

Dissertation

submitted to the

Combined Faculties for the Natural Sciences and for Mathematics

of the Ruperto-Carola University of Heidelberg, Germany

for the degree of

Doctor of Natural Sciences

presented by

Diplom-Physiker Daniel Aquino Maier

born in Cochabamba

Oral examination: February 1st, 2011

**Single Marker Switching Nanoscopy
with 4Pi Detection:
Superior Nanometric 3D Resolution**

Referees: Prof. Dr. Dr. h.c. Stefan W. Hell
Prof. Dr. Rainer H. A. Fink

Abstract – Zusammenfassung

The spatial resolution of light microscopy was limited by diffraction for a long time. Switching markers between a dark and a bright state was the key element to overcome this limitation. In single marker switching (SMS) microscopy, switching and subsequent localization of single markers enables the creation of two-dimensional superresolution images. The approaches to extend SMS microscopy to the third dimension were hitherto hampered by a substantially anisotropic resolution or limited to samples thinner than half the marker fluorescence emission wavelength. Still, a light microscope allowing three-dimensional subdiffraction imaging of thick samples with a homogeneous and isotropic resolution combined with the ability to differentiate between different types of markers is highly desirable.

This thesis presents a nanoscope which combines the SMS concept with the 4Pi-technique to address these important issues. The spherical wavefronts generated by a single fluorescence emitter are collected by two opposing objective lenses of high numerical aperture, brought to interfere and focused onto an area detector. By evaluating higher order moments of the detected spots, single markers can be simultaneously localized within samples of theoretically unlimited thickness with an unsurpassed accuracy. 3D localization accuracies of better than 10 nm within a layer of at least 1 μm thickness are shown. Importantly, this 1 μm sheet can be placed at any depth within the sample. Further, by splitting the fluorescence into orthogonal polarization states, the 4Pi-SMS setup facilitates the 3D nanoscopy of multiple marker species. The biological applicability of the presented method is proven for different biological samples and for distinct types of markers. Offering a unique combination of multicolor recording, nanoscale resolution, and extended axial depth, this work substantially advances the non-invasive 3D imaging of cells and other transparent materials.

Die Auflösung in der Lichtmikroskopie war lange Zeit durch die Beugung limitiert. Das Schalten zwischen hellen und dunklen Zuständen von Markern ist das Schlüsselement zur Überwindung dieser Beschränkung. Die Einzelmolekülschaltmikroskopie (englisch: single marker switching, SMS) ermöglicht durch das Schalten und die Lokalisierung einzelner Marker eine zweidimensionale Bildgebung mit einer Auflösung deutlich unterhalb der Beugungsgrenze. Bisherige Ansätze, die SMS Methode auf die dritte Dimension zu erweitern, führten entweder zu einer erheblich anisotropen Auflösung oder waren auf Proben beschränkt, welche dünner als die halbe Fluoreszenzwellenlänge des Emitters sind. Das ideale Lichtmikroskop sollte jedoch eine homogene und isotrope räumliche Auflösung unterhalb der Beugungsgrenze in dicken Proben besitzen und gleichzeitig in der Lage sein, zwischen verschiedenen Markertypen zu unterscheiden.

In dieser Arbeit wird ein Nanoskop vorgestellt, welches das SMS Konzept mit der 4Pi Technik vereint um die oben genannten Eigenschaften zu erreichen. Hierzu werden die sphärischen Wellenfronten eines einzelnen fluoreszierenden Emitters von zwei sich gegenüber stehenden Objektiven hoher numerischer Apertur gesammelt, zur Interferenz gebracht und auf eine Kamera fokussiert. Durch die Auswertung höherer Momente der detektierten Bildpunktfunktion wird die Lokalisierung einzelner Marker mit bisher unerreichter Genauigkeit innerhalb einer beliebigen dicken Probe erreicht. In der vorliegenden Arbeit werden Lokalisationsgenauigkeiten besser als 10 nm in allen drei Raumrichtungen innerhalb eines Detektionsvolumens von mindestens 1 μm Dicke präsentiert. Hierbei ist zu betonen, dass das Detektionsvolumen beliebig innerhalb der Probe positioniert werden kann. Biologische Anwendungen werden für unterschiedliche biologische Systeme und für verschiedene Markertypen exemplarisch vorgestellt. Durch die Aufteilung des

Detektionssignals in orthogonal polarisierte Zustände ist es zudem möglich, eine einfache Differenzierung zwischen unterschiedlichen Markertypen zu implementieren. Durch die bisher einzigartige Kombination von Mehrfarbenaufnahme, Auflösungen im Nanometerbereich und Bildgebung in ausgedehnten Proben stellt diese Arbeit einen wesentlichen Fortschritt in der nichtinvasiven dreidimensionalen Bildgebung dar.

Contents

List of Contents	viii
List of Figures	x
List of Tables	xii
1 Introduction	1
1.1 Thesis Outline	5
2 From Microscopy to Nanoscopy	7
2.1 Conventional fluorescence microscopy and its limits	7
2.1.1 Point Spread Function - Determination of the resolution properties of an optical system	7
2.1.2 Fluorescence - The Signal Generation	10
2.1.3 The Wide-Field Microscope	11
2.1.4 The Confocal Microscope	13
2.1.5 The 4Pi-Microscope	15
2.2 Nanoscopy - Resolution below the diffraction barrier	18
2.2.1 Ensemble/Targeted Mode - STED, RESOLFT,...	18
2.2.2 Single Molecule/Stochastic Mode : PALM, STORM,...	20
3 Single Marker Switching Microscopy	23
3.1 2D-SMS Approach	23
3.1.1 Acquiring the Image Data	23
3.1.2 Marker Localization	24
3.1.2.1 Algorithm	25
3.1.2.2 Localization Precision	27
3.1.2.3 Photon Statistics	28
3.1.3 Image Creation	29
3.1.4 SMS Toolbox	30
3.2 3D-SMS - Breaking the PSF Symmetry	31
3.2.1 Astigmatism	32
3.2.2 Defocus - Biplane	34
3.2.3 Double Helix	35
3.2.4 Theory of 4Pi-SMS	37
3.3 Information Content	37

4	4Pi-SMS - The Nanoscope	43
4.1	The Setup	43
4.2	The Cavity	45
4.2.1	Dipole Orientation	45
4.2.2	4 Channel Detection	47
4.3	Signal Generation	49
5	Theory - Optimizing the Information Content	51
5.1	Coherent Detection	51
5.2	Moment-based Estimator	52
5.2.1	Analytical Phase Plane Depiction	53
5.2.2	Bent Wavefronts	55
5.2.3	Reduced Moments	56
5.3	Extracting z	59
5.3.1	Implementation of the Estimator	59
5.3.2	Color Coding	60
6	Characterizing the Nanoscope	61
6.1	Fluorescent Beads	61
6.2	Resolution potential of 4Pi-SMS	61
6.2.1	Photon Number Dependence	63
7	Biological Applications	65
7.1	Imaging the fibrinogen receptor distribution on activated human platelets	65
7.1.1	Results	65
7.1.2	Samples for platelet imaging	68
7.2	Deep Section Imaging of Cultured Mammalian Cells	69
7.2.1	Cytoskeleton of Microtubules - Results	69
7.2.2	Samples for imaging of the tubulin cytoskeleton	71
8	Multicolor Expansion	73
8.1	Exploiting the 4th Channel	73
8.2	Biological Application	74
8.2.1	Two Color Imaging of Cell Network and Peroxisomes	74
8.2.2	Samples for Two Color Imaging	77
9	Conclusion	79
A	List of Acronyms	83
B	Statistics - Moments	85
C	The Stabilization Module	87
D	Tubulin rings	89
	Bibliography	91

List of Figures

2.1	Imaging Theory	7
2.2	Imaging with a lens	9
2.3	Fluorescence	11
2.4	The Wide-Field Microscope	12
2.5	The Confocal Microscope	14
2.6	The 4Pi-Microscope	17
2.7	The STED principle	19
3.1	SMS Acquisition	25
3.2	Localization Algorithm	26
3.3	Photon Statistics	29
3.4	Detection by Astigmatism	33
3.5	Biplane Detection	35
3.6	Double Helix PSF	36
3.7	4Pi-SMS PSF	38
3.8	Fisher Information Limits	40
4.1	The Nanoscope	44
4.2	$\lambda/4$ -plates	45
4.3	Babinet Solei Compensators	48
4.4	4Pi-SMS Signal	49
5.1	The Bent Phase Planes	55
5.2	Moment Modulation	56
5.3	Moment Mask	57
5.4	Phase Space	58
6.1	z -Resolution	62
6.2	xyz -Resolutions	63
7.1	Activated Human Platelets	66
7.2	SMS vs. Confocal	67
7.3	φ_0 vs. φ_0 - φ_3 -space	68
7.4	Cellular Cytoskeleton	70
8.1	Cellular Network & Peroxisomes	75
8.2	The s - p -space	76

8.3	Color recovery	77
C.1	The Automatic Module	87
D.1	Tubulin rings	90

List of Tables

2.1	PSF calculation parameters	13
3.1	PSF simulation parameters	32
3.2	Fisher Information parameters	39
3.3	3D-SMS techniques	41
6.1	Resolution parameters	64

Chapter 1

Introduction

Ever since its invention, the optical microscope has enabled scientists to make many important discoveries in the life sciences and beyond. Ranging from identifying the details of many different diseases and thus facilitating the development of remedies, over the discovery of the cell as a building block of life and developing a frame of a cell's substructure and its underlying functions, the optical microscope has emerged as a powerful and versatile instrument for the life sciences. Many remaining questions have not been solved for a long time yet and many novel problems need to be addressed. Despite all progress, the microscope was always hampered by its limited resolution, i.e. the inability to resolve structures smaller than a certain dimension. This resolution limit, also known as the diffraction barrier, was formulated mathematically by Émile Verdet (1), Ernst Abbe (2) and Lord Rayleigh (3) in the 19th century independently and states that,

$$\Delta r \gtrsim \frac{\lambda}{2n \sin \alpha} \quad (1.1)$$

$$\Delta z \gtrsim \frac{2\lambda}{n \sin^2 \alpha} \quad (1.2)$$

where λ denotes the vacuum wavelength of the employed light, n is the refractive index of the medium and α is the semi aperture angle of the objective lens. Δr defines the lateral resolution and Δz the axial resolution. The fact that both are not same results from the asymmetry of the underlying optical system and will be discussed in more detail later on. The parameters in above equations are not arbitrary eligible. Visible light has a wavelength in the range of 400-780 nm, shorter wavelengths are not desirable due to the augmented absorbance of light in the UV regime by standard optical components and the increasing harm provoked by higher energetic photons to living organisms. The product $n \sin \alpha$ in eq. (1.1) is also termed numerical aperture (NA) and the values for a high NA oil objective are limited to about 1.47, inferring a maximal feasible semi aperture angle α of about 78° . The refractive index is limited due to aberrations introduced by strongly mismatching refractive indices of immersion and embedding media (4). Summing up, the above equations imply that the resolution of an optical microscope in the visible range is limited to about 200 nm in the lateral and 500 nm in the axial directions.

Indeed, various techniques have emerged in the last decades which allow to resolve structures in the nanometer regime and below. Nevertheless, none of them broke the diffraction barrier given by above equations. Moreover, when focusing on live cell research, all of these techniques are hampered or even not applicable at all. As already indicated above, the most obvious way to improve the resolution is to reduce the wavelength. This principle is adopted in electron microscopy where λ corresponds to the *de Broglie* wavelength of the electron, which is far below 1 nm, and

thus allows resolutions down to 1\AA . Another method for high resolution imaging is the scanning tunneling microscopy (STM), where the tunneling current through a conducting tip is measured while the tip is scanned over the surface of a conducting sample (5). Although all of these methods have spurred scientific breakthroughs, imaging living objects is barely possible since these techniques require evacuated environments at cryogenic temperatures, conductive samples which have to be coated, or sliced samples. Each of these requirements is by itself live cell incompatible. The atomic force microscope (AFM) is also impressive. It scans a resonant oscillating tip across the surface of the sample and measures the impact of attractive or repulsive forces on the resonance frequency and the phase of the oscillation (6). Worth mentioning are also near field optics where nanosized mechanical tips use the near field of the light to reconstruct a high resolution image (7) and novel techniques with meta materials which use negative refractive indices to gather non propagated waves carrying further structural information (8, 9, 10). However, these techniques are all surface bound and therefore inhibit the imaging of the interior of living cells. In addition, the samples have to be placed quite close to the instrument, which is a hindrance for many applications, especially in the life sciences.

In contrast, far-field fluorescence microscopy has already proven to be an exceptional tool for the life science. Many different labeling techniques for various markers, like for example fluorophores, proteins or gold beads have been developed and ensure a specific tagging of the structures of interest. At the same time, these methods are minimal invasive which in combination with the low light intensities employed enable live cell research due to minimization of the perturbations. Further, the good signal-to-noise ratio (SNR) allows full 3D-reconstruction of structures, also inside cells, without requiring harmful sample preparation methods. In comparison to the other techniques, it is easy to use and quite stable.

Taking all these advantages into account, it is obvious that a resolution below the diffraction limit is desirable for far-field fluorescence microscopy. Thus, there have been many different attempts to break the diffraction barrier. Among others, the use of aperture filters was proposed (11) or an m -photon excitation (12) was suggested. However, none of these methods improved the resolution by more than a factor of two. Another way to push the limit was realized by 4Pi-microscopy, where the spherical wavefronts of two opposing objective lenses are coherently superimposed (13, 14, 15). The asymmetry in the detected part of the emitted wavefront of a single lens, which leads to a worse axial resolution in eq. (1.2), was thus diminished and an axial resolution enhancement by a factor of 3-7 was achieved. In the ideal case of collecting the whole wavefront, the system would be almost rotational invariant and thus the axial and lateral resolutions should also be the same. A similar concept was proposed by Gustaffsson et. al and termed I⁵M (16). Since these concepts essentially only expand the used solid aperture angle, they are still subject to the diffraction barrier.

In summary, all these techniques pushed the resolution to its limits, but they did not break the barrier. In the 1990s, stimulated emission depletion (STED) was proposed as the first concept to obtain resolutions below the diffraction limit, at least in fluorescence microscopy (17, 18). The basic idea behind this concept is to switch off all fluorophores which are outside the small region of interest and to read out the remaining ones. Combined with scanning, thus a diffraction unlimited image can be obtained. Its applicability and underlying functional resolution dependence was demonstrated in various studies (19, 20, 21).

Having opened up the field of 'diffraction-unlimited' resolution, STED was followed by many other techniques enabling sub-diffraction resolution. Basically, these methods can be divided into two subgroups depending on the way they address the fluorophores. To the *targeted mode*,

which addresses the fluorophores in ensembles and targets their coordinates by optical methods, belong STED, ground-state depletion (GSD) (22), reversible saturable optical fluorescence transitions (RESOLFT) (23, 24, 25, 26), saturated patterned excitation microscopy (SPEM) (27) or saturated structured illumination microscopy (SSIM) (28, 29). RESOLFT itself can be seen as a generalization of STED and GSD (23).

The other family addresses the markers stochastically in space and time, so that only one fluorophore is allowed to emit within the diffraction volume at an unknown position at a time. It is therefore termed *stochastic mode*. Since in the stochastic modality the position of the emitter is not known a priori, $N \gg 1$ photons have to be detected from the emitting marker to localize its position with a precision which in a first approximation scales as,

$$\Delta r \gtrsim \frac{\lambda}{2n \sin \alpha \sqrt{N}} \quad (1.3)$$

The coordinates of a single marker are determined by computational analysis of its point spread function (PSF). This principle is employed in photoactivated localization microscopy (PALM) (30), stochastic optical reconstruction microscopy (STORM) (31), fluorescence photoactivation localization microscopy (fPALM) (32), PALM with independently running acquisition (PALMIRA) (33), ground state depletion microscopy followed by individual molecule return (GSDIM) (34), points accumulation for imaging in nanoscale topography (PAINT) (35), direct STORM (dSTORM) (36) and time-lapse PALM (TL-PALM) (37). Since only the switching mechanism discerns these methods, they will be summarized as stochastic mode or single marker switching (SMS) microscopy in the course of this thesis. An intrinsic advantage of the single molecule approach is the availability of information about, for example the spectrum, lifetime and polarization of the single molecules. This for example facilitates the identification of different markers in multicolor labeling, even if the dyes fluorescence spectra overlap significantly (38, 39). Many biological applications like for example the colocalization of different proteins benefit from this simple way of differentiation between distinct markers.

The key to resolution below the diffraction barrier and the common principle employed by all these methods is the switching of the marker between a dark non-detectable state, also called *off*-state, and a bright detectable state, also termed *on*-state (24, 40, 41). Markers closer than the diffraction limit are discerned by consecutively switching them on and off and thereby identifying their position with sub-diffraction precision sequentially. While the diffraction barrier for the light itself remains, exploiting the inherent properties of the markers themselves, enabled sub-diffraction resolution and thus opened up the field of *nanoscopy*.

The underlying switching mechanism allows a further grouping of the different methods. For instance STED, SSIM and SPEM employ the S_0 - S_1 transition of a fluorescent marker as dark and bright states. GSD and GSDIM use the long lived triplet state of a molecule as the off-state and the $S_1 \rightarrow S_0$ transition as the on-state. RESOLFT, PALM and STORM include switching isomerization states (*cis-trans*) and other optically bistable transitions as bright and dark states. The transition between the different conformations may be triggered by a photon absorption. Indeed any molecular transition which is a reversible (saturable) optical transition can be employed for breaking the diffraction barrier (42).

Since the aim of nanoscopy is a full 3D reconstruction of structure with sub-diffraction resolution in far-field fluorescence microscopy, the question arises how the above methods perform in the axial direction. It turns out that all nanoscopy methods can provide improved axial resolution,

e. g. by shrinking the region of markers in the on-state in the axial direction (18), by optical sectioning by two-photon induced switching (43), or by breaking the symmetry of the PSF along the z-axis and thus creating a z-dependent signal (44, 45). However, as in the diffraction limited case, the resolution along the optical axis will always remain at least ~ 2.5 times worse than its focal plane counterpart, if only a single objective lens is used.

It was already demonstrated that the coherent use of two opposing lenses, as introduced by the 4Pi technique, facilitates the axial resolution improvement in switching-based nanoscopy methods like STED (46, 47). The most recent developments in targeting mode nanoscopy led to a method termed isoSTED which makes isotropic three-dimensional resolution at nanoscale feasible (48). Theoretical studies also predicted a considerable resolution gain in a combined 4Pi-SMS microscope (49). Therefore, a closer look on the 4Pi technique is advisable.

As already indicated above, the disparity between the xy- and the z- resolution, eq. (1.1) and eq. (1.2), stems from the fact that a lens is able to focus and detect just a segment of a complete spherical wavefront. By coherently adding the spherical wavefront segments of two opposing high angle lenses for illumination and/or fluorescence detection, the total aperture of the microscope can be extended along the z-axis, increasing the z-resolution by up to sevenfold (50, 16, 15, 51). Introduced to imaging by the concept of 4Pi microscopy (50, 15, 51), the self-interference of an emitted photon collected by two opposing lenses is also a key element in I⁵M (16). Importantly, unambiguous axial superresolution with opposing lenses requires spherical wavefronts of high focusing angles, as used in 4Pi and I⁵M systems. Using just interfering plane waves limits this strategy to objects thinner than $\lambda/2$ ($\sim 250\text{nm}$) due to periodic replication artifacts (51).

The coordinate-targeted as well as the stochastic superresolution modalities experience a remarkable boost in resolution when employing a second opposing lens, as done in 4Pi systems, by taking advantage of an enlarged solid focusing or detection angle (49, 52). IsoSTED microscopy (52, 48) has thus achieved a resolution of < 21 nm and 30 nm in the lateral and axial directions respectively, utilizing relatively moderate STED laser intensities. In the stochastic modality, 4Pi photon detection records twice the number of fluorescence photons and thus directly increases the localization precision by about $\sqrt{2}$ in all directions. A substantial resolution enhancement of a factor of about 4 is expected along the z-axis (49). The first realization of this scheme, called iPALM (53), has achieved an impressive resolving power with localization accuracies of about 9.8 nm and 22.8 nm (full-width-half-maximum, FWHM) reported for the axial and the lateral directions, respectively. However, the iPALM studies were reportedly challenged by the fact that they rendered ambiguous axial positions for layers thicker than $\lambda/2$ (225 nm), limiting the method to ultra-thin slices or to the TIRF-illuminated proximity of the cover glass. This limitation stems from the fact that the method analyzes the waves of fluorescence emission just as plane waves.

Much like 4Pi microscopy solved the ambiguity problem by resorting to spherical rather than plane waves, in this thesis it will be shown how to solve this problem in the stochastic superresolution modalities by taking advantage of the spherical shape of the fluorescence emission wavefronts. Thus, a 4Pi-SMS (i.e. 4Pi-PALM/STORM/GSDIM/dSTORM etc.) microscope will be defined with a demonstrated resolution potential of at least 5.4 - 8.2 nm in the axial direction and 11.3 nm in the lateral direction (full width at half maximum (FWHM)) within an about 2λ ($\sim 1\mu\text{m}$) thick xy-optical layer placed to any z-position in the sample. Importantly, the sample can be much thicker than $1\mu\text{m}$ since emitters lying outside the optical layer can be identified and easily excluded. Moreover, the 4Pi-SMS microscope arrangement presented here readily accommodates multiple label recordings, which easily makes for example colocalization experiments possible. The currently unique combination of resolving power, depth of field, and multicolor

detection is demonstrated by imaging the 3D distribution of selected proteins in mammalian cells.

1.1 Thesis Outline

First a brief introduction to optical microscopy and its image formation theory is given. The derived diffraction limit, is discussed for three important microscope systems. Subsequently the way to nanoscopy is sketched for the targeting methods as well as for the stochastic mode (chapter 2). One of the foci of this thesis is establishing 3D structure reconstruction below the resolution limit in SMS microscopy by employing two opposing lenses. Therefore an introduction to 2D-SMS is given and afterwards how SMS can be extended to the third dimension best is discussed (chapter 3). Subsequently, the 4Pi-SMS setup of this work is presented in chapter 4. The approach to maximize the axial information content employed by the 4Pi-SMS setup is discussed in detail in chapter 5. A nanoscope based on these concepts is characterized in chapter 6. Its biological applicability is demonstrated in chapter 7. The way to the biologically relevant ability of multi-color detection is shown in chapter 8. Finally, the results are discussed and an outlook for future developments is given (chapter 9).

Chapter 2

From Microscopy to Nanoscopy

In the following chapter some fundamental relations of image formation in microscopy will be introduced (54, 55, 56, 57). ‘Abbe’s law’, the diffraction barrier, will be shown to follow from the derived equations as a consequence of the wave nature of light. This limit is illustrated by three important and established microscopy techniques, namely the epifluorescent, confocal and 4Pi microscope, which will be examined in more detail. The way to nanoscopy, by making use of the switching properties of the labels, will be described for the targeted as well as the stochastic mode.

2.1 Conventional fluorescence microscopy and its limits

2.1.1 Point Spread Function - Determination of the resolution properties of an optical system

Since light is a part of the electromagnetic spectrum the underlying equations of optical microscopy are Maxwell’s equations. For simplicity, the scalar case of diffraction theory is studied. Nevertheless, similar considerations to those conducted here can be carried over to vectorial diffraction theory (54). As Maxwell’s equations are linear, an optical system with an electromagnetic input field $E_{in}(\mathbf{r}')$ in a plane defined by $\mathbf{r}' = (x', y')$ and an output field $E_{out}(\mathbf{r})$ in a plane

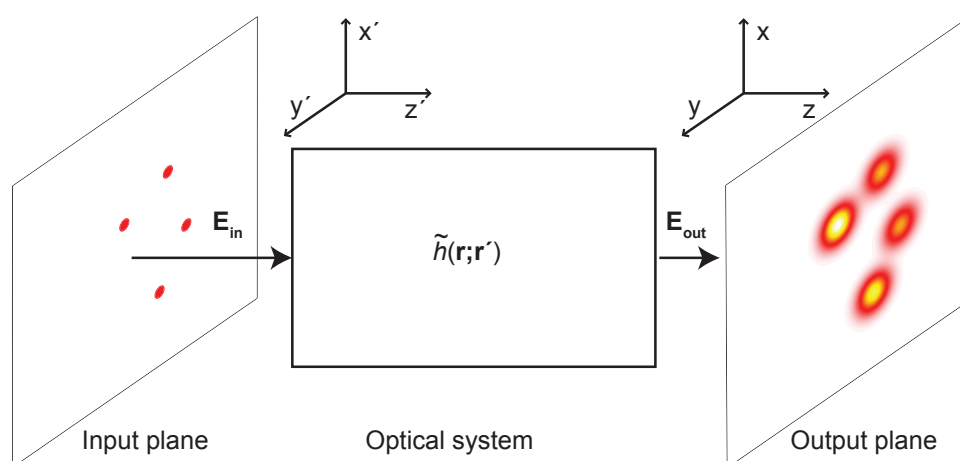


Figure 2.1 A general imaging system, with input plane, optical system and output plane.

$\mathbf{r} = (x, y)$ behind the optical system (Fig. 2.1), can be described by,

$$E_{\text{out}}(\mathbf{r}) = \int \tilde{h}(\mathbf{r}; \mathbf{r}') E_{\text{in}}(\mathbf{r}') d\mathbf{r}' \quad (2.1)$$

with $\tilde{h}(\mathbf{r}; \mathbf{r}')$ defining the impulse response function of the optical system. If the input light is incoherent, an equivalent equation follows for the intensities,

$$I_{\text{out}}(\mathbf{r}) = \int h(\mathbf{r}; \mathbf{r}') I_{\text{in}}(\mathbf{r}') d\mathbf{r}' \quad (2.2)$$

The assumption of incoherent light is reasonable for the fluorescence imaging discussed here, as the potential phase information of the excitation light is lost during the incoherent emission process. If a shift invariant system is assumed, $h(\mathbf{r}; \mathbf{r}')$ can only depend on $\mathbf{r} - \mathbf{r}'$ and thus becomes $h(\mathbf{r} - \mathbf{r}')$. If the input intensity distribution I_{in} is a point source, i. e. equivalent to the delta function $\delta(\mathbf{r}')$, I_{out} by definition becomes the impulse response $h(\mathbf{r})$. In imaging theory $h(\mathbf{r})$ is also known as the intensity point spread function (PSF) of the optical system. For an imaging system I_{in} corresponds to the intensity distribution of the explored object $O(\mathbf{r})$ in the object plane, while I_{out} is its image $I(\mathbf{r})$ in the image plane. Therefore the dependence of the imaging process on the PSF is described by the following equation,

$$I(\mathbf{r}) = \int h(\mathbf{r} - \mathbf{r}') O(\mathbf{r}') d\mathbf{r}' \quad (2.3)$$

The image is thus a convolution of the object distribution with the PSF of the system,

$$I(\mathbf{r}) = h(\mathbf{r}) \otimes O(\mathbf{r}) \quad (2.4)$$

This equation becomes even more simple after Fourier transformation,

$$\mathcal{F}[I(\mathbf{r})] = \mathcal{F}[h(\mathbf{r}) \otimes O(\mathbf{r})] \quad (2.5)$$

$$\mathcal{I}(\mathbf{k}) = \mathcal{H}(\mathbf{k}) \cdot \mathcal{O}(\mathbf{k}) \quad (2.6)$$

$\mathbf{k} = (k_x, k_y)$ defines the spatial frequencies in x -, y -direction and $\mathcal{I}(\mathbf{k})$, $\mathcal{O}(\mathbf{k})$ are the Fourier transforms of the image and the object respectively. $\mathcal{H}(\mathbf{k})$ is called the optical transfer function (OTF) and, as can easily be seen from eq. (2.6), describes how spatial frequencies of the object distribution are transferred by the optical system. For instance if the OTF becomes zero for frequencies higher than \mathbf{k}_{lim} , these spatial frequencies of $\mathcal{O}(\mathbf{k})$ are not available in $\mathcal{I}(\mathbf{k})$ anymore. In real space this translates into the inability of resolving structures smaller than the inverse of \mathbf{k}_{lim} .

The PSF is now going to be calculated for the simplest optical system, which is a single lens. In scalar field theory the output field of a point emitter imaged by a lens (Fig. 2.2a) is given by (54),

$$E(\mathbf{r}) = A \int_0^\alpha \sqrt{\cos(\theta)} \sin(\theta) J_0 \left(k \sqrt{x^2 + y^2} \sin(\theta) \right) \exp(ikz \cos(\theta)) d\theta \quad (2.7)$$

Here A is a constant depending on the excitation strength, α the semi aperture angle and θ the corresponding variable polar angle, J_0 is the Bessel function of first kind and zeroth-order, $\mathbf{r} = (x, y, z)$ describes the x , y -coordinates in the image plane z , finally k is given by $k = 2\pi n/\lambda$

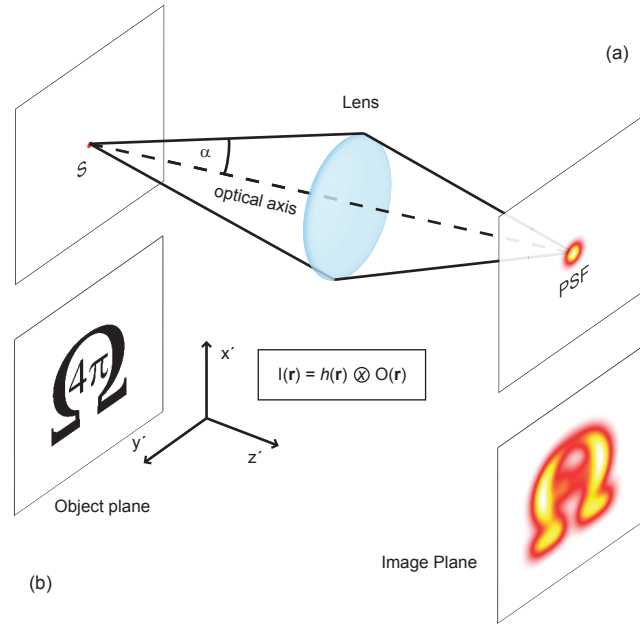


Figure 2.2 (a) Image of a point source S by means of a lens. The point source is blurred to the PSF of the system. (b) Image as convolution of the object with the PSF. Some details are lost due to the blurring.

with the vacuum wavelength of light λ and the refractive index n of the medium. The intensity distribution of the point emitters image is thus given as,

$$I_{\text{out}} = |\mathbf{E}(\mathbf{r})|^2 = h(\mathbf{r}) \quad (2.8)$$

the last implication follows from eq. (2.2) as I_{in} is the delta function $\delta(\mathbf{r})$. Evaluating the above equations shows that the image of a point source is an expanded light distribution characterized by the Bessel function of the first kind of order one (54). As the system shown in Fig. 2.2a is rotationally symmetric with respect to the z axis, cylindrical coordinates (r, ϕ, z) are more appropriate. The first minimum Δr of the function characterizing the intensity distribution is given by,

$$\Delta r \approx 0.61 \frac{\lambda}{n \sin \alpha} \quad (2.9)$$

in the focal plane, and the first minimum of $h(\mathbf{r})$ along the z axis is at,

$$\Delta z \approx 2 \frac{\lambda}{n \sin^2 \alpha} \quad (2.10)$$

The disk spanned by the radius defined in eq. (2.9) is also called *Airy disk*. According to the Rayleigh criterion, two point sources are regarded as just resolved when the principal diffraction maximum of one image coincides with the first minimum of the other. Therefore Δr and Δz correspond to the resolution in the lateral and axial direction respectively. The difference in factors between eq. (1.1) and eq. (1.2) are due to the fact that Abbe explored rectangular apertures instead

of circular ones. If the resolution is defined by the FWHM of the PSF the limits are,

$$\Delta r \approx 0.51 \frac{\lambda}{n \sin \alpha} \quad (2.11)$$

$$\Delta z \approx 1.77 \frac{\lambda}{n \sin^2 \alpha} \quad (2.12)$$

For many years these diffraction limits were thought to be insurmountable.

2.1.2 Fluorescence - The Signal Generation

The key to overcoming the diffraction barrier was to benefit from the inherent properties of fluorescent markers, namely their ability to switch between a dark off- and a bright on-state. In principle these states could also be of a different nature than fluorescence, but fluorescence has already proven to be a particular good signal source for microscopy. Not only the excellent SNR, but also the various labeling techniques for many available fluorophores and proteins convince. They enable a specific tagging of the desired structures, while simultaneously being minimal invasive and live cell compatible. In this section a short introduction to the fluorescence mechanism will be given (58).

The underlying theory of fluorescence is quantum electro dynamics. The Jablonski diagram is an appropriate way to sketch the eigenvalues and eigenstates of the underlying system. Basically it shows the energy values of the different electronic and vibrational states. The simplest case of a molecule with many electrons is a system with two electrons. The electron spins $s = 1/2$ couple to the total spin $\mathbf{S} = \sum_{i=1,2} \mathbf{s}_i$, resulting in the antisymmetric singlet state S with $S = 0$ ($M_S = 0$) and the symmetric triplet states T with $S = 1$ ($M_S = -1, 0, 1$). The multiplicity of the states is given by $M = 2S + 1$.

The Jablonski diagram in Fig. 2.3a exhibits the singlet ground state S_0 , the first excited singlet S_1 and triplet states T_1 . All electronic states are split into vibrational sub-states by phonon coupling, indicated by the gray lines. The lowest vibrational state is marked with a bold black line. At room temperature the lowest S_0 state has the highest probability of being populated. A photon absorption of the right energy heaves an electron from a S_0 state into a S_1 state. The vibrational states of S_1 decay via phonon interactions, indicated by the gray wavy lines, to the lowest state of S_1 . From there, either internal conversion (IC) (wavy vertical line) or a spontaneous photon emission (orange vertical line) to a vibrational state of S_0 takes place. Conventional fluorophores have fluorescence lifetimes τ_{fl} on the order of nanoseconds, depending on the molecule and the environment. The energy of the emitted photon is smaller than the energy of the absorbed photon due to the preceding phonon decays. This leads to a redshift between the absorption and emission spectra, known as Stokes-shift. The spectra are homogeneously and inhomogeneously broadened due to phonon- and environmental interactions. A typical fluorescence spectrum resulting from such states is shown in Fig. 2.3 b for the fluorophore Atto 532. The Stokes-shift is exploited to separate excitation from emission light (Fig. 2.4), which is necessary since the excitation intensity usually is many orders of magnitude larger than the fluorescence.

If the conservation of the total electronic spin were to be demanded, a transition between the singlet and triplet state would be prohibited. However rather than \mathbf{S} , $\mathbf{J} = \mathbf{L} + \mathbf{S}$ has to be conserved. Here \mathbf{L} defines the orbital angular momentum of the electronic wave function and \mathbf{S} the coupled spin of the electrons. Due to the coupling of \mathbf{S} and \mathbf{L} , a finite probability of inter system

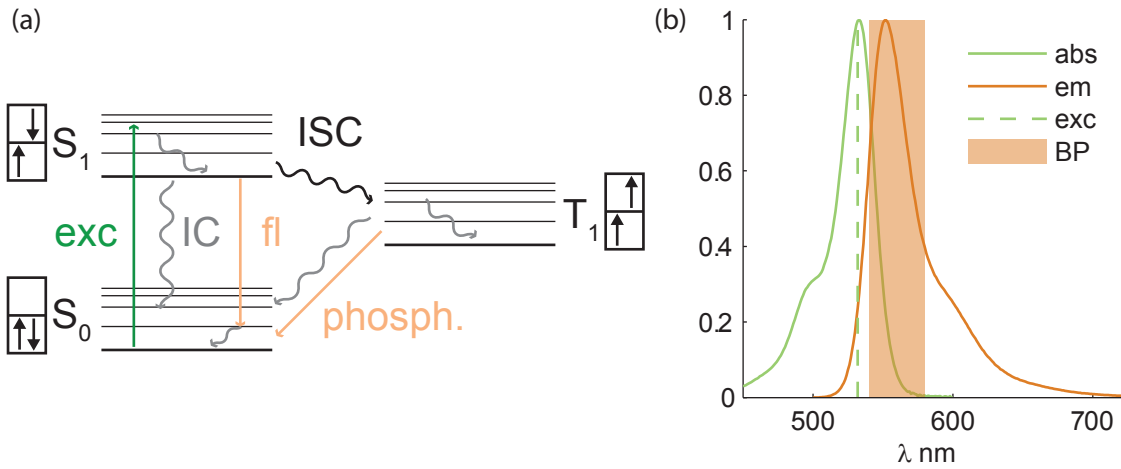


Figure 2.3 (a) Jablonski diagram of the electronic states S_0 , S_1 and T_1 . S_0 and S_1 are the electronic ground state and excited state, respectively. T_1 is the first excited triplet state. The gray lines represent vibrational sub-states. The green arrow indicates the excitation to S_1 (exc) from where the dye might decay to S_0 by emission of a photon (fl) or internal conversion (IC). The electron spins of the states are indicated by the arrows next to the corresponding labels. Inter system crossing (ISC) between S_1 and T_1 has a rather low but non vanishing probability. The same is valid for the transition T_1 to S_0 . A long lived triplet state T_1 is the result of this low transition probability. Photon emission from T_1 is called phosphorescence. (b) Normalized absorption (abs) and emission (em) spectra of the dye Atto 532. The green dashed line and the orange area indicate a typical excitation wavelength (exc) and the detection range of a microscope.

crossing (ISC), i. e. a transition between singlet and triplet state (and reverse), is given. Since this probability is low and the triplet state T_1 can only decay into the singlet state S_0 , T_1 exhibits a long life time. Typical lifetimes are $\tau = 1\mu s - 100ms$ depending on the environment (22). These long lifetimes of T_1 are exploited in ground-state depletion (GSD) and ground state depletion microscopy followed by individual molecule return (GSDIM) as the dark state for nanoscopy (59, 34). The radiative transition from T_1 to S_0 is referred to as *phosphorescence*, however more probable than a photon emission is the non-radiative relaxation of T_1 .

Finally, the issue of *photobleaching*, the irreversible loss of the fluorophore, which constraints resolution and image creation, shall be discussed. The long lived triplet state plays a crucial role in current theories about photobleaching (60). Its long lifetime increases the probability to undergo further excitation to higher energetic states, which may lead to conformational changes or even destroy the molecule. The triplet state can also interact with oxygen, which has a triplet state as ground state. This interaction leads to an excited singlet oxygen, which can then decay into a highly reactive radical, capable of destroying the adjacent fluorophore. To prevent from such harmful effects, in many studies glucose oxidase is used as an oxygen quencher.

2.1.3 The Wide-Field Microscope

Now that the image creation of an optical system and the signal sources have been established, three important microscope techniques will be discussed, starting with the *wide-field microscope*,

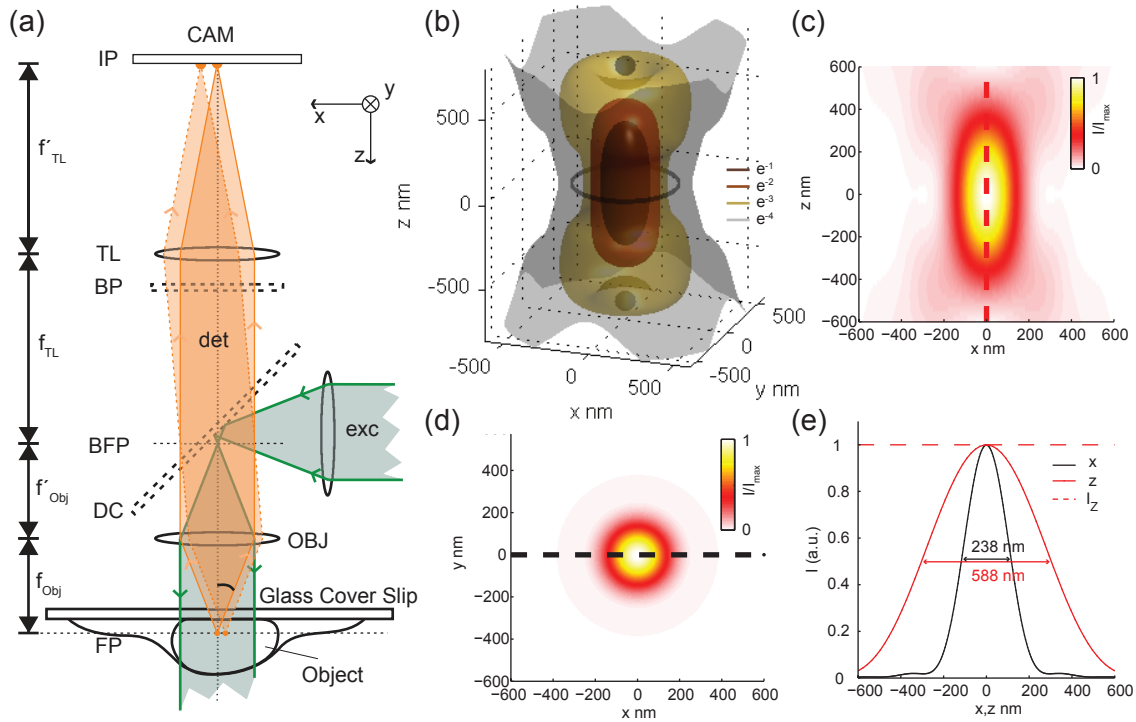


Figure 2.4 (a) Setup of a typical wide-field microscope. The excitation light (green) is focused to the back focal plane of the objective lens (OBJ) to obtain a wide-field illumination. The object is placed in the focal plane (FP) of the objective lens with the focal distance f_{obj} . The red-shifted fluorescence light (orange) is collected and imaged onto a camera (CAM) by the objective and tube lens (TL) with a focal length of f_{TL} . The fluorescence is separated from the excitation light by a long pass dichroic mirror (DC). An optional bandpass filter (BP) improves the SNR. (b) Calculated PSF of the wide-field microscope. The different colors depict isosurfaces with at $e^{-1}, e^{-2}, e^{-3}, e^{-4}$ of the maximal intensity. (c) xz -cross-section of the PSF at $y = 0$. (d) xy -cross-section of the PSF's focal plane. (e) z -, x -profile of the dashed lines in (c,d) and the z -response of the PSF (dashed line). Note that the PSF has a larger extension along the z -axis than along the x -axis. The z -response $I_Z(z)$ of a wide-field microscope is constant, revealing the inability to discern different z -planes.

also referred to as an *epifluorescence microscope* (61). Fig. 2.4a shows a standard wide-field microscope setup. It basically consists of three lenses, an excitation source, a camera for detection and a dichroic mirror to separate excitation and fluorescence. The excitation light is coupled in by the long-pass dichroic mirror and focused into the back focal plane of the objective to yield a homogeneous illumination (wide-field) of the sample, which is mounted on a glass cover slip. The fluorescence in the focal plane is collected and collimated by the objective lens. Since the emission light experiences a Stokes-shift, it passes through the dichroic mirror, while excitation light, backscattered from the sample, is reflected. The collimated light is focused onto a camera by a second lens, the so called *tube lens*, which is usually optimized for the objective lens. Thus, each point of the object is imaged to the image plane at the camera, resulting in the final image. In

Table 2.1 PSF calculation parameters

semi-aperture angle	α	64.5°
excitation wavelength	λ_{exc}	532 nm
emission wavelength	λ_{det}	570 nm
2-Photon excitation wavelength	λ_{2P-exc}	850 nm
depletion wavelength	λ_{STED}	650 nm
refractive index	n	1.515
pinhole diameter	ρ_0	$0.6 \cdot d_{\text{Airy}}$

the so called 4f imaging geometry, the back focal point of the objective lens and the focal point of the tube lens coincide. In this geometry the magnification M of the system is given by the ratio of the focal lengths $M = f_{\text{tube lens}}/f_{\text{objective lens}}$. For SMS microscopy, the magnification is chosen in a way that the camera pixel approximately sample the PSF according to the Nyquist criterion (62). Typically a bandpass (BP) filter is introduced after the dichroic to reduce the background signal, for instance from auto fluorescence, and thus improve the SNR. The PSF of a wide-field microscope is given by eq. (2.8),

$$h_{epi}(\mathbf{r}) = h(\mathbf{r}) \quad (2.13)$$

A big disadvantage of the wide-field microscope is that it can not discriminate between structures from different planes along the z -axis in the sample, i. e. structures in the focal plane and structures out of the focal plane are both imaged onto the camera with equal strength. As these planes are defocused, they contribute to the background rather than to the image. A quantity used to assess the capability of a microscope to discern different z -planes is the z -response, which is defined as the overall signal detected from an infinitesimally thin xy -layer in dependence of z ,

$$I_Z(z) = \int h(\mathbf{r}) dx dy \quad (2.14)$$

A microscope capable of discriminating between different z -planes, also referred to as *optical sectioning*, has a fast decreasing z -response for an increasing distance from the focal plane.

The wide-field PSF is shown in Fig. 2.4b-e. The common parameters for this and subsequent calculations are summarized in table 2.1. An xz -cross-section of the focal plane as well as an xy -cross-section along the optical axis and its central profiles are illustrated in Fig. 2.4c-d, respectively. Note the rotational symmetry about the z -axis and the stronger extension of the PSF in the z -direction. The z -response of the the wide-field microscope is shown in Fig. 2.4e and reveals its non existent optical sectioning capability.

2.1.4 The Confocal Microscope

The confocal microscope, first proposed by Minsky in 1961 (63), enables optical sectioning. A typical confocal setup is sketched in Fig. 2.5a. It basically consists of a point source which is imaged into the sample, resulting in a diffraction limited intensity distribution $h_{exc}(\mathbf{r})$, and a pinhole located at the image plane in front of the detector. The generated fluorescence is collected by the same objective lens and focused by the tube lens. Again the back scattered excitation light is separated from the fluorescence light by a dichroic mirror. In the back projected image plane a pinhole (PH) is inserted, ensuring that only light from the focal plane reaches the detector

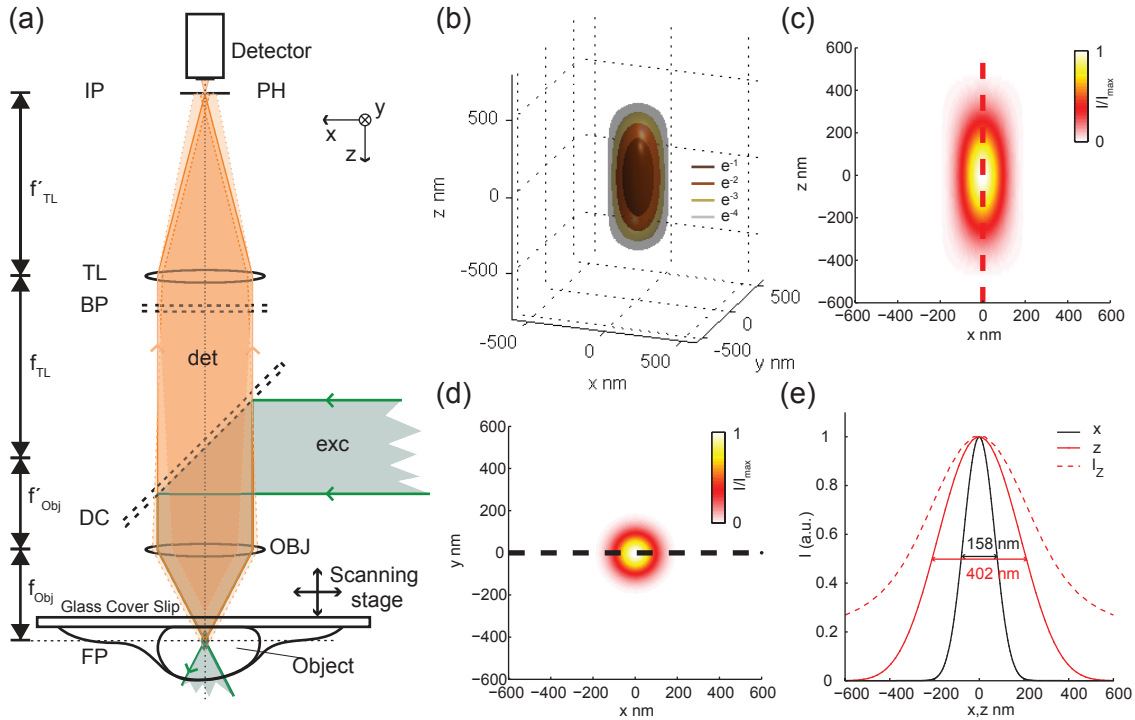


Figure 2.5 (a) Confocal microscope. The collimated excitation light (green) is focused to a diffraction limited spot in the sample by the objective lens (OBJ). The object is placed in the focal plane (FP) of the objective lens with a focal distance f_{Obj} . The red-shifted fluorescence light (orange) is collected and imaged on a pinhole (PH) by a 4f-imaging system formed by the objective and tube lens (TL). The fluorescence is separated from the excitation light by a long pass dichroic mirror (DC). An optional bandpass filter (BP) improves the SNR. A detector collects the signal behind the pinhole. (b) Calculated PSF of a confocal microscope. The different colors depict isosurfaces at $e^{-1}, e^{-2}, e^{-3}, e^{-4}$ of the maximal intensity. Note that the confocal PSF is much less extended than the epifluorescent PSF (cf. Fig. 2.4). (c) xz -cross-section of the PSF at $y = 0$. (d) xy -cross-section of the PSFs focal plane. (e) z -, x -profile of the dashed lines in (c),(d) (solid lines) and the z -response of the PSF (dashed line). Again the PSF has a larger extension along the z - than the x -axis. The z -response is z dependent, enabling the confocal microscope to discern different z -planes.

behind, which is typically a photo multiplier tube (PMT) or, due to their high quantum efficiency an avalanche photo diode (APD). Light coming from below or above the focal plane as indicated by the dashed and dotted lines in Fig. 2.5a is rejected by the PH from reaching the detector. Due to the reversibility of the light path this can also be interpreted as imaging the pinhole into the sample. Its image corresponds to the detection PSF $h_{\text{det}}(\mathbf{r})$ and gives the detection probability of a photon emitted at \mathbf{r} . The final PSF of a confocal microscope emerges as the product of the probabilities of a fluorophore to be excited and detected,

$$h_{\text{con}}(\mathbf{r}) = h_{\text{exc}}(\mathbf{r}) \cdot h_{\text{det}}(\mathbf{r}) \quad (2.15)$$

For a point like pinhole, $h_{det}(\mathbf{r})$ is given by eq. (2.8). However, in practice a pinhole always has a finite size,

$$p(x, y) = \begin{cases} 1 & , \text{if } \sqrt{x^2 + y^2} \leq \rho_0 \\ 0 & , \text{else} \end{cases} \quad (2.16)$$

with ρ_0 being the radius of the pinhole. In this case the true detection PSF $\tilde{h}_{det}(\mathbf{r})$ is given by,

$$\tilde{h}_{det}(\mathbf{r}) = h_{det}(\mathbf{r}) \otimes_{x,y} p(x, y) \quad (2.17)$$

A confocal PSF is shown in Fig. 2.5b-e. In contrast to the wide-field PSF its extension along z is constrained to a smaller volume.

Scanning this PSF over the sample, by either deflecting the beam or moving the sample, and collecting the light for each scanning step creates the final image.

Note that the excitation and detection PSF have different underlying wavelengths due to the Stokes-shift between absorption and emission spectra of the dye. However, since the ratio is typically on the order of 0.95, the confocal PSF for an ideal pinhole can be approximated by,

$$h_{con}(\mathbf{r}) \approx h_{exc}^2(\mathbf{r}) \quad (2.18)$$

The quadratic dependence leads to an $\sqrt{2}$ improvement in FWHM and is responsible for the ability of optical sectioning of the confocal microscope, as seen by the z -response in Fig. 2.5e.

2.1.5 The 4Pi-Microscope

In this work the idea of 4Pi microscopy (13) is employed to obtain resolutions below 10 nm in all spatial directions in SMS microscopy. Therefore, the basic concepts of the 4Pi techniques implemented so far will be introduced. The motivation behind 4Pi microscopy was to obtain better resolutions by maximizing the aperture size. Coming back to the diffraction barrier given by eq. (1.1) and eq. (1.2), it is obvious that at a given wavelength λ , the $NA = n \sin \alpha$ constrains the resolution. The two parameters which can be adapted are the refractive index n and the semi aperture angle α . The refractive index of the immersion medium may not differ too strongly from the refractive index of the embedding medium, which in live cell applications usually is water ($n_{H_2O} = 1.33$), as otherwise strong spherical aberrations are introduced, which worsen the resolution (4, 64). Increasing α is technically demanding and for angles larger than $> 70^\circ$ almost impossible. However, exactly the asymmetry created by collecting only a small sector of the entire wavefront, which propagates into the whole solid angle of 4π , is responsible for the asymmetry of eq. (1.1) and eq. (1.2) and causes the bad resolution along the z axis. 4Pi microscopy improves this drawback by the coherent use of two opposing lenses with high numerical aperture. Depending on the implementation, it coherently sums up either the counter propagating spherical wavefronts of the focused excitation light fields at the common focal point (4Pi-Type A), the spherical wavefronts of the emitted fluorescence light field at the detector (4Pi-Type B), or combines both (4Pi-Type C) (14, 65, 51). Thus a resolution improvement in the axial direction by a factor of 3-7 can be achieved. A drawback is that side lobes are created by the interfering waves (see Fig. 2.6), which lead to ‘ghost images’ in the recorded data. The intensity of these side lobes is decreased by confocal detection and 2 photon excitation (cf. Fig. 2.6). Deconvolution of the raw data can reduce the ‘ghost images’ and is either mandatory or optional, depending on the method applied. 4Pi also belongs to the scanning microscopy methods.

A similar principle was realized by Gustafsson and named I⁵M (66, 16, 67). It also employs two opposing lenses but brings the counter propagating excitation light fields to form a flat standing wave rather than being focused, and detects the interfering fluorescence on a camera instead of confocal detection. The advantage of a parallelized image acquisition comes along with the disadvantage of increased side lobes due to the wide-field detection, which makes mathematical deconvolution of the raw data mandatory. Furthermore, high NA objectives are required, since image quality drops fast with decreasing aperture angles. Thus water objectives are barely possible, making live cell experiments difficult.

The best results for a 4Pi-Type C-setup are achieved if two photon (2P) excitation and confocal detection are employed (68). A typical 4Pi setup of Type C with 2P-excitation is illustrated in Fig. 2.6a. It basically consists of a 4Pi cavity for excitation and one for detection (right, left triangles, respectively). The 2P-excitation laser is split by a beamsplitter into the two legs of the 4Pi cavity. The objectives (OBJ) focus the collimated beams to diffraction limited spots which interfere coherently in the focal plane. The fluorescence light is collected by the second 4Pi cavity built up by two long pass dichroics (DC), which reflect the emitted light, and a beamsplitter (BS), at which the gathered photons interfere. The focal plane is imaged on a pinhole (PH) for confocal detection by e. g. an APD. The 2P excitation PSF, i. e. the probability of exciting a molecule by a two photon process is just given by the squared probability of inducing a one photon excitation,

$$h_{exc,2P}(\mathbf{r}) = h_{ext}^2(\mathbf{r}) \quad (2.19)$$

Taking into account the vectorial character of light and the coherent superposition of the electrical fields, $\mathbf{E}_{\gamma,a}$, $\mathbf{E}_{\gamma,b}$ ($\gamma = exc, det$), of both objectives a and b, the PSF of a 4Pi-Type C setup with a 2P-excitation reads as follows,

$$h_{4Pi,C}(\mathbf{r}) = h_{ext}^2(\mathbf{r}) \cdot (h_{det}(\mathbf{r}) \otimes_{x,y} p(\mathbf{r})) \quad (2.20)$$

$$= (|\mathbf{E}_{ext,a} + \mathbf{E}_{ext,b}|^4) \cdot (|\mathbf{E}_{det,a} + \mathbf{E}_{det,b}|^2 \otimes_{x,y} p(\mathbf{r})) \quad (2.21)$$

with the confocal pinhole $p(\mathbf{r})$ given by eq. (2.16). The fields of both objectives, $\mathbf{E}_{\gamma,a}$ and $\mathbf{E}_{\gamma,b}$ are connected by,

$$\mathbf{E}_{\gamma,b}(\mathbf{r}) = e^{i\Delta\varphi_\gamma} \cdot \hat{T} \cdot \mathbf{E}_{\gamma,a}(\hat{T} \cdot \mathbf{r}) \quad (2.22)$$

with the geometry dependent transformation matrix,

$$\hat{T} = \begin{pmatrix} 1 & 0 & 0 \\ 0 & 1 & 0 \\ 0 & 0 & -1 \end{pmatrix} \quad (2.23)$$

and the phase difference $\Delta\varphi_\gamma$, considering distinct path length or refractive indices in the arms of the 4Pi cavity. The calculated PSFs are shown in Fig. 2.6b-f. Two photon excitation has two advantages. Firstly, the quadratic dependence of $h_{exc,2P}$ lowers the ratio of side lobe intensity to main peak intensity compared to the one photon case. Secondly, as can be seen in Fig. 2.6c-d the side lobes of the detection PSF approximately peak at the first minima of the excitation PSF. This is explained by the almost doubled wavelength of the excitation light compared to the fluorescence light. Since the final PSF is the product of both PSFs the side lobes are further decreased (Fig. 2.6e).

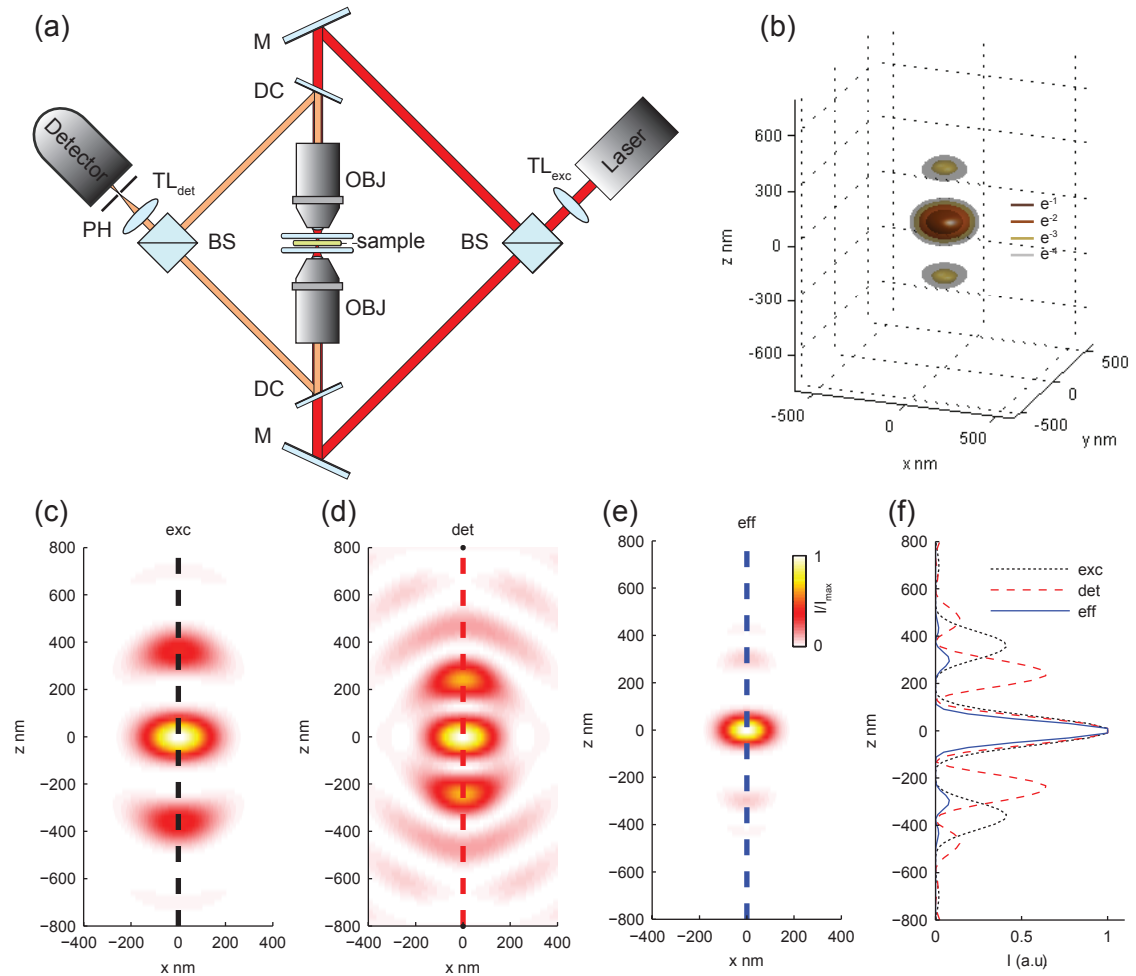


Figure 2.6 (a) 4Pi-Type C microscope with two photon excitation. The collimated excitation light (red) is split by a beamsplitter (BS). The beams are focused by the objectives (OBJ) and are coherently added up. The fluorescence (green) is collected by both objectives and reflected by the dichroic mirrors (DC). The beams interfere at the second beamsplitter and are detected in confocal mode. (b) Simulated PSF of a 4Pi microscope. The different colors depict isosurfaces at $e^{-1}, e^{-2}, e^{-3}, e^{-4}$ of the maximal intensity. Note the interference patterns in contrast to the confocal PSF (cf. Fig. 2.5). (c,d,e) xz -cross-sections at $y = 0$ of the excitation, detection and effective PSF respectively. The side lobes of the 2P-excitation and detection have different z positions due to the distinct wavelengths. (f) z -profiles $I_z(z)$ of the dashed lines in (c-e). Note that the side lobes of the detection are near to the minima of the excitation, leading to smaller side lobes of the effective PSF. The FWHM of the central peak is about 7 times smaller than the FWHM of the confocal microscope.

2.2 Nanoscopy - Resolution below the diffraction barrier

Now that the diffraction barrier has been formulated and its limits have been explored for different established microscopy techniques, the way beyond the diffraction limit will be elucidated.

Switching between a dark off-state and a bright on-state of a marker generating the signal for detection, is common to all methods with sub-diffraction resolution. Most techniques use fluorescence as the signal source of the bright on-state. Although a simple fluorophore with its ground state S_0 and excited state S_1 already fulfills this requirements and enables sub-diffraction resolution, like e. g. in STED, many other switching modalities employ conformational changes of molecules, as e. g. cis-trans isomerization, to switch between a dark and a bright state. Indeed, nanoscopy is not restricted to fluorescence, every signal source capable of switching between a signal generating on- and a dark off-state, may be exploited for sub-diffraction imaging. Depending on the way the markers are targeted, the nanoscopy techniques can roughly be divided into two groups, which are going to be introduced next.

2.2.1 Ensemble/Targeted Mode - STED, RESOLFT,...

The ensemble mode is characterized by targeting, mostly an ensemble, of markers simultaneously at certain predefined coordinates. At this position a spatial light distribution is applied, which constrains markers in a sub-diffraction volume to a certain state, e. g. the on-state, while all other markers in the targeted region are in the off-state. This principle is going to be explained using the example of stimulated emission depletion (STED) microscopy, which was historically the first concept breaking the diffraction barrier (17, 18). STED uses the fluorescent state S_1 of a molecule as the on-state, while the non fluorescent S_0 state describes the off-state. First all molecules within a diffraction limited area are excited to S_1 (Fig. 2.7a). Subsequently, in a time much shorter than the nanosecond fluorescence lifetime, a second red shifted doughnut-shaped beam follows (Fig. 2.7b). This beam prevents the dyes from fluorescing. As the probability to not fluoresce increases with the intensity of the doughnut-shaped beam, which ideally has zero intensity in its center, molecules in the outer regions are hindered from fluorescing while those in the most central region, with a diameter $d \ll \lambda/(2n \sin \alpha)$ are still capable of fluoresce. Thus, fluorescence is only collected from a sub-diffraction region (Fig. 2.7c). Iterating this process by either scanning the beam or the sample leads to the final image with a resolution below the diffraction barrier. This process can be parallelized, e. g. by creating an array of ‘zero’ lines or points with a distance $> \lambda/(2n \sin \alpha)$ and recording the fluorescence on a camera. Scanning the pattern over the sample again results in the sub-diffraction image. It can be shown that Abbe’s law (1.1) can be expanded by a square root term to define the enhanced resolution (21, 41),

$$\Delta r \gtrsim \frac{\lambda}{2n \sin \alpha \sqrt{1 + a I_{max}/I_s}} \quad (2.24)$$

here I_{max} depicts the peak intensity of the beam constraining the light field and $a > 0$ is a parameter depending on the exact form of the depletion PSF. The *saturation intensity* I_s is a characteristic of the underlying switching mechanism and scales inversely with the lifetime of the on-state. The probability that a marker remains in the on-state depends on the switching beam intensity $I(\mathbf{r})$ and scales with $\exp(-I(\mathbf{r})/I_s)$. As already mentioned, the light field $I(\mathbf{r})$ is adjusted in a way that this probability vanishes except in a small region around $\mathbf{r} = 0$. At a given saturation intensity the resolution is theoretically unlimited if the intensity I_{max} can be

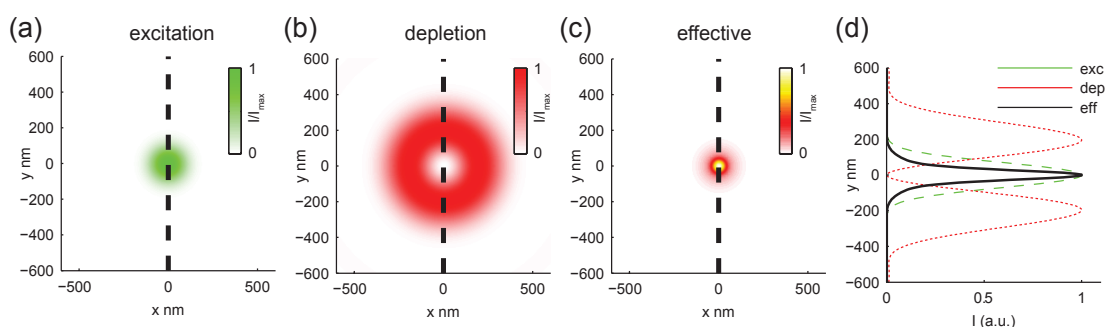


Figure 2.7 The STED principle. Calculated (a) confocal excitation, (b) depletion PSF created by a 2π ‘phase ramp’ phase mask and (c) effective PSF. (e) y -profiles of the dashed lines in (a-c). The effective PSF has a smaller FWHM than the confocal PSF. Increasing the depletion power theoretically enables infinite resolution.

brought to infinity. However, when the resolution reaches about the size of the marker molecules, the classical resolution definition becomes inappropriate and the signal has to be analyzed more carefully. To achieve high resolutions at low intensities, the saturation intensity I_s should be small, which requires long lived states. STED requires relatively high intensities I_{max} on the order of several 100 MW/cm^2 since the S_1 - S_0 transition typically has lifetimes on the order of nanoseconds. An implementation of a targeted mode which uses longer lived states than the S_0 - S_1 pair is ground-state depletion (GSD) (22, 59). Here the metastable triplet state T_1 , with lifetimes up to 0.1 ms, is employed as the dark state, while the bright state is defined by the fluorescence emitted by a S_1 - S_0 transition. Typical switch off intensities used are on the order of several kW/cm^2 . A further advantage of this system is that the switching and probing pulses can have the same wavelength. Thus, only one laser system is required. The basic idea is the same as behind STED. First, for e. g. a doughnut shaped high intensity pulse pushes all molecules around a sub-diffraction region into the dark state T_1 via excitation to S_1 and subsequent spontaneous inter system crossing (ISC) (s. Fig. 2.3). Subsequently, a regularly shaped probe pulse reads out the remaining fluorescence of the central region.

Generalizing the concept behind STED and GSD to switching reversibly activatable proteins and organic fluorophores leads to reversible saturable optical fluorescence transitions (RESOLFT) (23, 24, 26). Here conformational changes of the marker, i. e. cis-trans isomerization, are employed to switch between the dark and bright states.

Further ensemble methods are saturated patterned excitation microscopy (SPEM) (27) and saturated structured illumination microscopy (SSIM) (28). The basic principle of these techniques is to illuminate the sample with a standing wave interference pattern and saturate the fluorescent state, which is recorded by a camera. With the a priori knowledge of the spatial frequency of the illumination pattern, a mathematical analysis of the image in Fourier space is conducted. Due to the saturation, higher spatial frequencies are shifted into the frequency range covered by the OTF of the optical system and mathematically back shifted to their ‘real’ position in frequency space. Thus the computed OTF recovers frequencies which would not pass the optical system with standard illumination. The back transformation of the image to real space reveals structures below the diffraction limit. To obtain sub-diffraction resolution over the whole image the pattern has to be scanned along the sample, which is usually done by phase-shifting the maxima of the

interference pattern. The resolution improvement is only available perpendicular to the minima of the standing wave pattern. To achieve a resolution improvement in all directions the pattern is rotated several times. Due to its wide-field recording mode, this method is highly parallelized.

2.2.2 Single Molecule/Stochastic Mode : PALM, STORM,...

Besides the targeted methods, another group of techniques achieving resolutions below the diffraction limit came up. The two key elements common to this group of techniques are localization and stochastic switching of single markers. In this section a short introduction and overview about already implemented methods will be given. A more detailed description will follow in the next chapter.

Localization of a marker, e. g. a fluorophore, emitting $N \gg 1$ photons can be done with an accuracy which scales with $1/\sqrt{N}$. Although known for a long time (69), localization of single molecules (70) alone is not able to provide images with resolutions below the diffraction limit. The reason is that the localization process, namely determining the center of the single molecule PSF, cannot be conducted if more than two molecules are active within the diffraction limited spot of size $\lambda/(2n \sin \alpha)$, since in this case their PSFs cannot be discerned. First employing the second key component, namely switching, enables the time sequential localization of many molecules within a diffraction limited volume. For that purpose, just one arbitrary fluorophore within this volume is stochastically switched on and localized, while all other markers are kept in the off-state. Iterating this process in time, i. e. recording many frames with single molecule detections, assures that all markers are localized at least once.

This concept of stochastic temporal unmixing by molecular switching was contemporarily realized by different groups and termed photoactivated localization microscopy (PALM) (30), stochastic optical reconstruction microscopy (STORM) (31) and fluorescence photoactivation localization microscopy (fPALM) (32). While photoactivated localization microscopy (PALM) uses photoactivable fluorescent proteins as the switch, STORM employs photochromic cyanine dyes with one of them used as an activation switch facilitator. However, the acquisition time in these experiment took up to ten hours, which requires extremely stable microscopes. PALM with independently running acquisition (PALMIRA) solved this problem by using asynchronous switching (33). In contrast to PALM, which switches the markers to their on-state at the beginning of each frame acquisition, in PALMIRA the molecules are switched to their bright state continuously at a rate that ensures no overlap of the single molecule PSFs. This lead to typical acquisition durations in the order of a few minutes.

As GSD, its single molecule counterpart, termed ground state depletion microscopy followed by individual molecule return (GSDIM), employs the triplet state T_1 as dark state (34). In above described methods the initial state of the markers is the off-state, which is switched on for detection. In contrast, the initial state in GSDIM is the on-state and the markers are switched off at the beginning of the data acquisition, by pushing most of them into the triplet state, or other dark states, so that only a very sparse amount can fluoresce and thus be localized. Stochastic return of molecules from the triplet state assures that all regions are sampled. GSDIM has the advantage that no further switching laser source is needed and a simple preselection of the sample can be done by using its fluorescence signal.

Further implementations of single molecule methods are dSTORM, a simplified version of STORM that is not restricted to special dyes for activation anymore (36) and PAINT, where the

on-state is induced by the binding of something to the structure to be imaged, while otherwise the marker is in its off-state (35).

The localization accuracy of the molecule's coordinates in all described methods can be approximated by,

$$\Delta r = \frac{\lambda}{2n \sin \alpha \sqrt{N}} \quad (2.25)$$

where N denotes the number of detected photons (69, 71, 72).

Since the key to all these nanoscopy concepts is switching, they will be referred to as single marker switching (SMS) microscopy from now on.

Chapter 3

Single Marker Switching Microscopy

In the following an introduction to single marker switching (SMS) microscopy will be given. First the basic two-dimensional concept and its implementation are going to be discussed. However, as information is encoded in the third dimension which is lost in a two-dimensional projection, there have been approaches to extend SMS methods to the third dimension (44, 45, 73, 49, 53). The principal problem thereby is the symmetry of the PSF along the z -axis, which makes it impossible to distinguish signals from above and below the focal plane with the same distance to it. How this symmetry can be broken will be discussed in section 3.2.

In contrast to the targeted modes, which achieve their resolution enhancement by constraining the signal to sub-diffraction regions generated by light fields, a typical 2D SMS setup just employs a standard wide-field detection PSF. In SMS microscopy the time-sequential localization of single detected markers allows to create the superresolved image. The excitation and switching light in SMS methods is rather used to create the signal and to constrain it to certain areas in order to reduce background or enable optical sectioning. Thus the excitation PSF is less crucial in SMS methods than in the targeted modes. When referring to the PSF in this chapter, the detection PSF is meant for the most part.

In this work excitation is performed in wide-field mode, i. e. an approximately homogeneous illumination is applied implying a homogeneous fluorescence probability over the whole sample. Other approaches often also use total internal reflection fluorescence (TIRF) illumination to reduce the background signal. As most SMS methods so far employed fluorescent markers with a bright and a dark state as the switching system, such markers will also be assumed in the following considerations. However, again it should be emphasized that nanoscopy is not restricted to fluorescent markers. A typical SMS setup is based on the wide-field microscope introduced in section 2.1.3 and shown in Fig. 2.4, expanded by a fast camera with almost 100% duty cycle and high quantum yield.

3.1 2D-SMS Approach

Creating a 2D-SMS image can be subdivided into three steps, acquiring the image data, localizing the markers and finally rendering the superresolved image.

3.1.1 Acquiring the Image Data

As seen in section 2.1.1 the image generated by a microscope is given by the convolution of the object, i. e. the marker distribution, with the PSF. Therefore, structures of sub-diffraction

size are blurred and cannot be resolved. SMS microscopy addresses this issue by employing switchable markers to isolate markers in their on-state and by localizing them individually in time (30, 31, 32). A switchable marker exhibits a bright on-state A and a dark off-state B. In this work the switching is induced by light of a certain wavelength, e. g. UV light. The bright state is typically a fluorescent state which is excited by light of a different wavelength, e. g. green light (see Fig. 3.1a). The whole process defined by the data acquisition and the marker localization is sketched in Fig. 3.1. The marker distribution is defined by the black 4Pi logo. Assuming that all fluorophores initially are either in their dark state B or can be driven to it, the switching light (swi) brings a sparse stochastic subset of markers to the bright state A (Fig. 3.1a). The light intensity is chosen in a way that the probability of two markers in state A being closer than the diffraction limit is negligible. Excited by a second laser (exc), the markers emit a bunch of photons which are recorded by a fast camera with high photon yield, e. g. an electron multiplying charge coupled device (EMCCD). The image of a single marker is blurred to a diffraction-limited spot by the imaging system, but it can be identified unambiguously (Fig. 3.1b). Such a bunch of photons will be referred to as an *event* or a *photon burst* from now on. Each event can be localized, i. e. its center can be determined, with sub-diffraction precision (Fig. 3.1c). After emitting the photons the markers fall back to their dark state, another (metastable) dark state (e. g. the triplet state T_1), or are bleached (cf. section 3.1.2.3). In any case, they stop to fluoresce. In the next frame the activation laser stochastically switches on another subset of markers and the whole process is iterated (Fig. 3.1 central column). The real marker distribution, a corresponding wide-field and SMS image of the markers are shown in Fig. 3.1d-f, respectively. It is clearly visible that blurred details in the wide-field image are resolved in the SMS image.

Therefore, the registration of the markers is spatio-temporally unmixed. As a single marker is already the smallest possible emitter, no further optical confinement is required. For a given PSF the localization precision, among other factors, depends on the photon number and the pixel size of the camera. In many cases an appropriate choice of the pixel size is given by the standard deviation σ_{det} of the detection PSF, a coarser choice leads to a loss of information, while a finer one worsens the signal-to-noise ratio (SNR). A more detailed description can be found in (74).

The first SMS implementations were hampered by the long acquisition times required (30, 31, 32). In this work the acquisition scheme introduced by PALMIRA is employed, which leads to recording times on the order of minutes (33). It basically involves an independently running acquisition, i. e. , the fluorophores are also switched on and off stochastically in time and not synchronized to the camera. The frame rate and the excitation intensity are optimized to achieve a fast recording and, simultaneously, a good SNR. The best SNR is obtained if a bunch of photons is detected within a single frame. If the frame time t_{fr} is too short, additional readout noise is collected since the photons of one event are distributed over many frames, while a too large t_{fr} increases the background.

3.1.2 Marker Localization

The localization analysis used in this work is based on a *Gaussian mask fitting* algorithm (33, 74), which has proven to be stable and accurate enough for the applications presented here. New methods based on maximum likelihood estimators (MLEs) have been established and show that the information content of the system, i. e. the real position of the marker, is recovered even more accurately. (75, 76, 77). The reason is that the MLEs model the intrinsic Poisson distribution of the data, while all methods based on Gaussian fits erroneously assume normal distributed data.

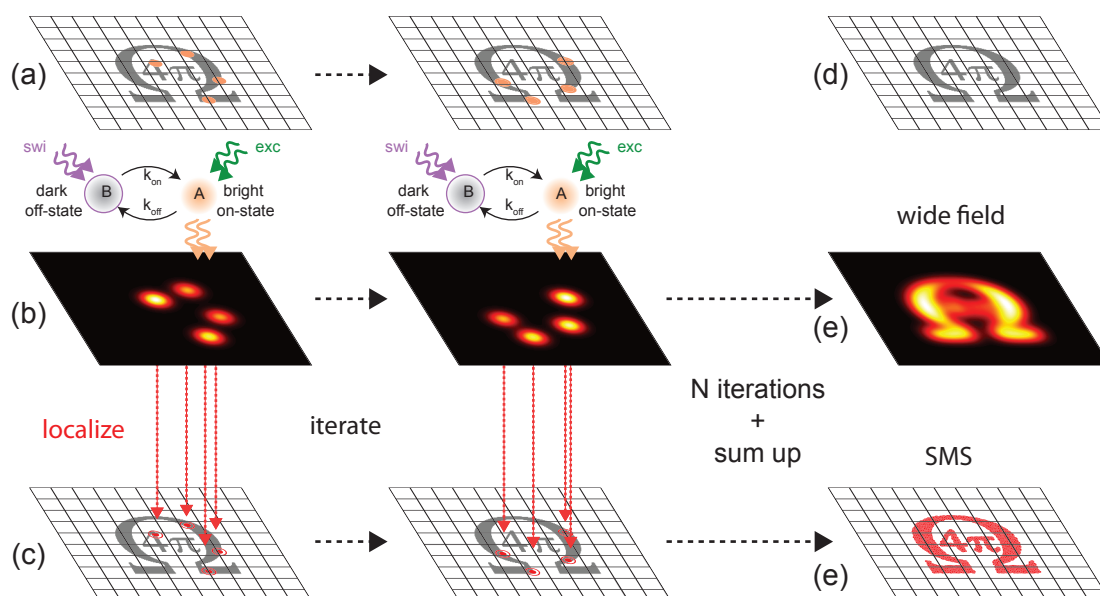


Figure 3.1 (a) A marker distribution given by the black 4Pi logo. All markers are initially in their dark state B. A laser (swi) switches sparse random subsets of markers to the bright state A (orange points). These markers are excited (exc) and emit photons (orange wavy lines). (b) The blurred photon distributions in the image plane are recorded by a camera. Note that each marker can be identified. (c) Localization of the center of the photon distribution. The grid sketches the camera pixels, each marker can be identified with a subpixel precision. After emitting the photons, the markers fall back to their dark state (or any other dark state) and another iteration takes place (central column). (d) Real marker distribution. (e) wide-field image of the markers, details are blurred. (f) SMS image of the markers with sub-diffraction resolution.

However, the difference in precision is not tremendous and the MLEs yet have to prove their robustness on experimental data sets. If they prove to be reliable, already acquired data can easily be reanalyzed. In the future, parallel computing and computation on graphics processing units (GPUs) will enable ‘online’ image reconstruction (76, 78) rather than post acquisition analysis.

3.1.2.1 Algorithm

Mathematically, the SMS localization process is equivalent to a wavelet analysis (79). Thereby, the underlying marker distribution is decomposed into wavelets of stochastic widths and positions. The basic wavelet is the detection PSF $h_{det}(\mathbf{r})$ of the system, i. e. it is proportional to the diffraction pattern of a single molecule. The PSF of a standard SMS system is rotationally symmetric about the z -axis. In the current section imaging of a two-dimensional object located in the focal plane is studied, implying $z = 0$. With these assumptions, a good approximation for $h_{det}(x, y, z = 0)$ is

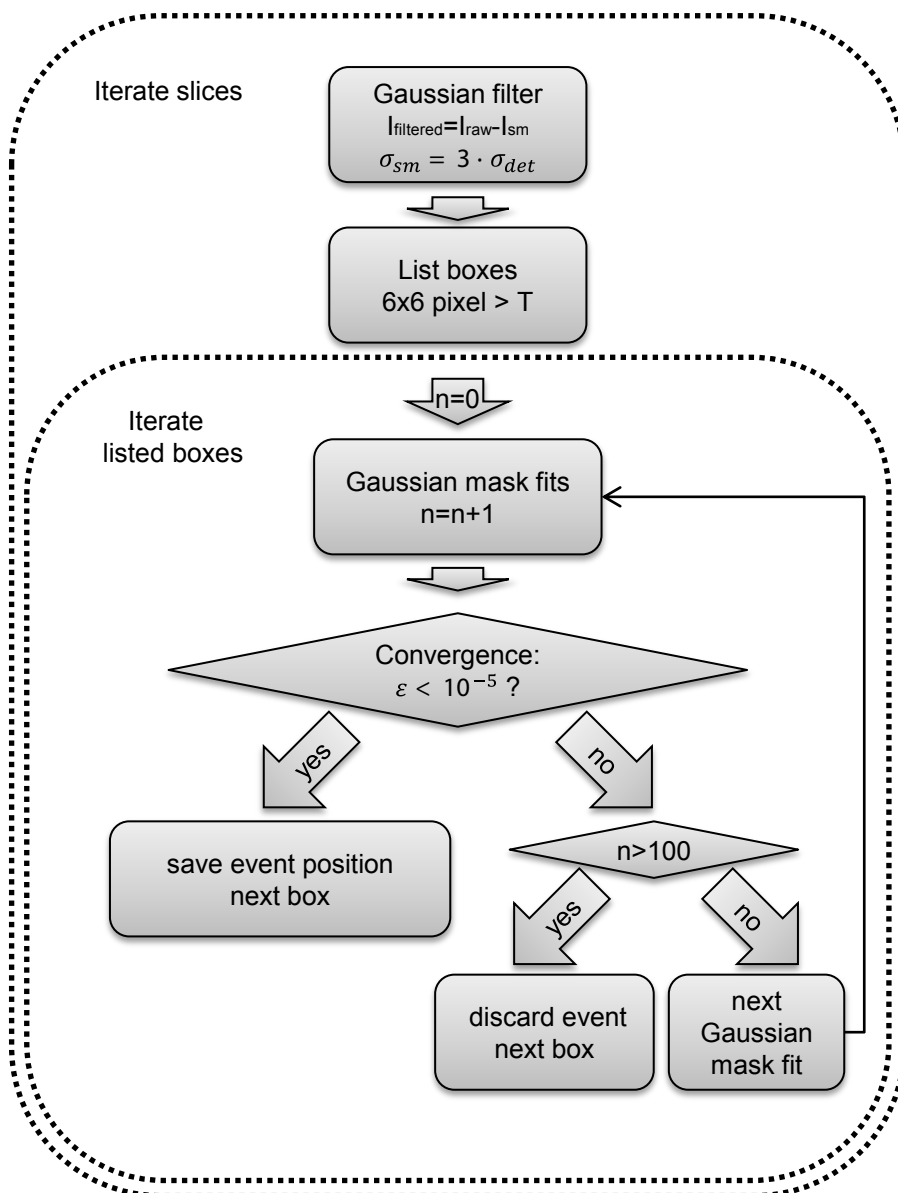


Figure 3.2 Flow chart of the localization algorithm

given by a two-dimensional Gaussian. A marker at $\mathbf{r}_c = (x_c, y_c)$ is thus defined by

$$h_{det}(\mathbf{r}, \mathbf{r}_c) = A \exp\left(-\frac{(x - x_c)^2 + (y - y_c)^2}{2\sigma_{det}^2}\right) \quad (3.1)$$

This approximation of the PSF is used within the algorithm sketched in Fig. 3.2. The algorithm is called *Gaussian mask fit* and equivalent to the scheme described in (74). For each image recorded, the following steps are conducted. First a Gaussian filter with $\sigma_{sm} = 3 \cdot \sigma_{det}$ is applied to remove

the inhomogeneous background and prevent false noise localizations. The raw data (I_{raw}) is thus smoothed with a Gaussian of standard deviation σ_{sm} and the smoothed image (I_{sm}) is subtracted from the raw data, yielding the filtered image I_{filtered} . Squared boxes with at least 6x6 pixel above the photon threshold T are listed for the Gaussian mask fits. Each Gaussian mask fit multiplies the box with a Gaussian of standard deviation σ_{det} and centered at the position obtained from the previous iteration. The position is determined as the center of mass of the computed box values. Convergence is given, if the position of two subsequent iterations changes by less than 10^{-5} times the pixel size. If the algorithm converges within 100 iterations the position and photon number of the event are saved. The Gaussian mask fitting algorithm is intermediate in complexity between a full non-linear least-squares fit and a centroid-based algorithm.

3.1.2.2 Localization Precision

As the PSF is rotationally symmetric about the z axis, the same inferences follow for x and y and therefore the lateral coordinates will be represented by r in the subsequent discussion. The resolution of a SMS microscope is given by the precision of the localization process and approximated by eq. (2.25). Due to the thresholding in the localization algorithm described above, only events with a photon number exceeding a certain threshold T are accepted. The photon number of the accepted events feature a geometric distribution (section 3.1.2.3). A more sophisticated description of the resolution includes the effect of thresholding and reads (80)

$$\Delta r_{FWHM} \gtrsim \frac{\lambda}{2n \sin \alpha} \sqrt{\frac{\phi(\frac{N}{N+1}, 1, T)}{N+1}} \quad (3.2)$$

where N denotes the mean photon number of the molecules and the function ϕ is Lerch's- ϕ -transcendent, describing the stochastic spread which corresponds to the accepted photon values. The function ϕ is the analogon to the Airy function in classical microscopy or the depletion doughnut in STED microscopy (80).

However, for most practical purposes an estimate of the resolution is enough. According to common statistics, the mean of a normal distribution with standard deviation σ_{det} can be determined with a precision given by

$$\Delta r = \frac{\sigma_{det}}{\sqrt{N}} \quad (3.3)$$

where the distribution is sampled by N measurements (photons). Thus the localization process, i. e. the position determination of a marker, has a precision of Δr . This explains the functional dependence of eq. (2.25) and will be used as resolution approximation of a SMS microscope from now on. Note that the full width at half maximum (FWHM) of the distribution can be used to assess the resolution instead. Both definitions just differ by a factor

$$\Delta r_{FWHM} = 2\sqrt{2 \ln 2} \Delta r \approx 2.35 \Delta r \quad (3.4)$$

With an infinite number of photons N an infinitely high resolution should be achievable. However, this definition of resolution again becomes meaningless when the size of the marker system is reached.

The above equation neglects noise sources other than shot noise, e. g. background noise, pixelation noise, dark counts or readout noise. A more sophisticated description considering these noise sources can be found in (74). Nevertheless, if the background is reduced by appropriate

optical filters and a EMCCD camera acquires the images at low temperatures and high electron multiplying gains, eq. (3.3) is an appropriate approximation. The electron multiplying process of the EMCCD camera changes the probability distribution of the signal, leading to a reduction of the SNR by a factor of $\sqrt{2}$ for large gain factors. This *excess noise factor* introduces an additional localization uncertainty (81). A more detailed analysis reveals that the effect can be considered by halving the number of detected photons

$$\Delta r_{\text{EMCCD}} = \frac{\sigma_{\text{det}}}{\sqrt{N/2}} \quad (3.5)$$

3.1.2.3 Photon Statistics

As the number of detected photons defines the resolution of a SMS microscope, this section will briefly sketch the underlying statistics from which an expectation value for the mean photon number can be derived.

Photon emission starts after the marker is switched from its dark off-state B to its bright on-state A (Fig. 3.3a). The transition from B to A is spontaneous and assumed to be negligible in comparison to the other rates considered here. The switching rate $k_{on}(I_{on})$ and the excitation rate $k_{exc}(I_{exc})$ depend on the intensity of the activation and excitation laser, respectively. I_{on} is chosen in a way that the on-markers are sparse enough to allow detection of individual molecules. On the one hand I_{exc} has to be as high as possible for a fast re-excitation of the fluorophore after a photon emission, on the other hand a too high intensity leads to an increased bleaching and thus reduces the number of emitted photons. An optimum has to be found for each dye and environment. After being excited to S_1 a fluorophore either fluoresces with a rate $k_{fl} = 1/\tau_{fl}$, with the fluorescence lifetime τ_{fl} , or it goes to a non-fluorescent state like e. g. T_1 , or it is bleached. In the latter two cases the fluorophore is not fluorescing during the actual frame anymore. All rates leading to a non-fluorescent state add up to the rate k_{nfl} . The probability of a photon emission for each excitation decay cycle is given by the fluorescent rate divided by all other available rates,

$$p_{fl} = \frac{k_{fl}}{k_{nfl} + k_{fl}} = 1 - p_{nfl} \quad (3.6)$$

with p_{nfl} the probability not to fluoresce. The probability of N consecutive photon emissions with a followed transition to a non-fluorescent state afterwards is given by

$$P(N) = (1 - p_{fl}) \cdot p_{fl}^N = p_{nfl} \cdot (1 - p_{nfl})^N \quad (3.7)$$

This is a geometric distribution for the number N of photons emitted by a single fluorophore. Fig. 3.3b exhibits the time trace of a typical measurement integrated over a camera area of 4x4 pixels. The photon bursts of many different single molecule detections are clearly visible. The photon numbers of the single bursts are randomly drawn from a geometric distribution. Fig. 3.3c reveals the photon number distribution of all detected events in the whole image. Note that the geometric distribution is truncated at the lower end due to the photon threshold applied in the localization process. The distribution is fitted by an exponential decay function, $a \cdot \exp(-N/\mu)$, where μ denotes the mean photon number of the underlying geometric distribution. Fig. 3.3d reveals the mean photon numbers obtained from subsequently analyzing 400k events of an image in groups of 20k events. The decay indicates that at the beginning of the measurement most probably events of higher order (i. e. double, triple, ... events) were detected. Higher order events

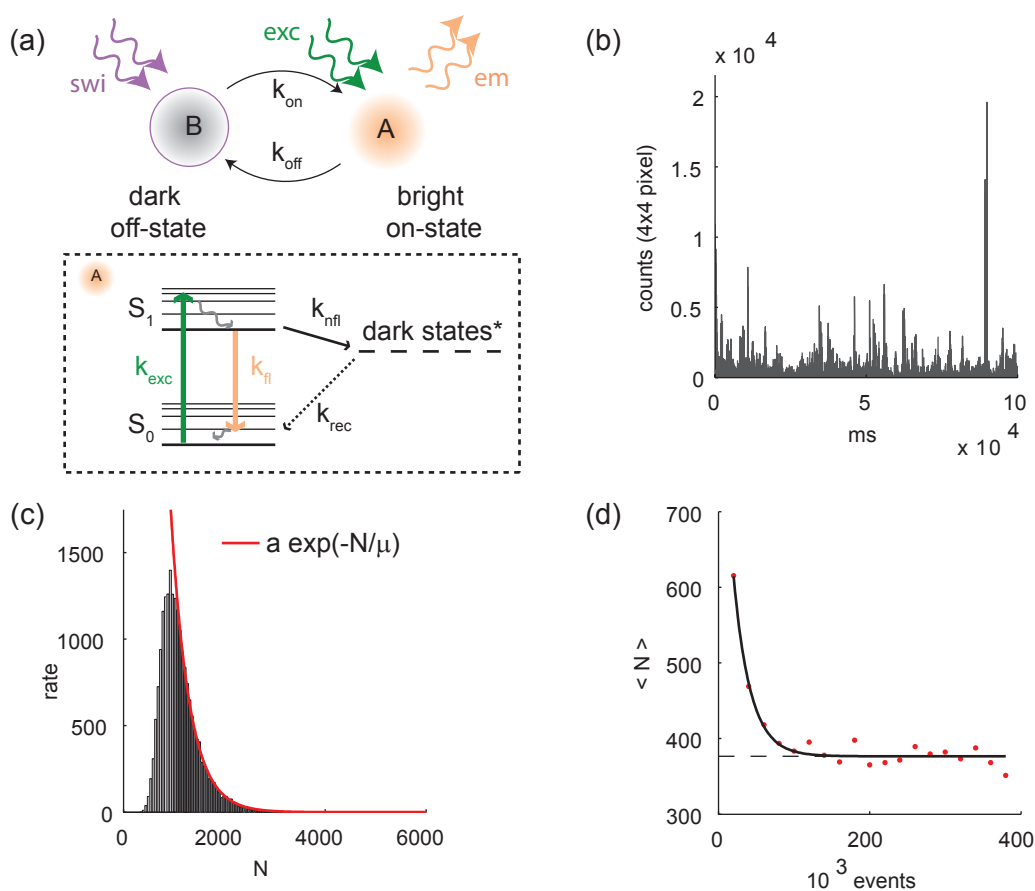


Figure 3.3 (a) Switchable fluorescent marker. The marker is switched on (swi) and excited (exc) by light of specific wavelengths, e. g. UV (swi) and visible (exc). It emits photons with a rate k_{fl} or goes into a non-fluorescent dark state with a rate k_{nfl} (subfigure). (b) Time trace of collected counts on a 4x4 pixel array of a camera with an integration time of 10ms. Photon bursts of many different single molecule detections are visible. (c) A cut geometric distribution of 20k events and an exponential fit to the dark gray bins. The expected mean photon number μ of the whole distribution is 365. (d) The mean photon number as a function of detected events during image acquisition. The mean photon number was calculated for subsequent groups of 20k events each. The decay indicates events of higher order (i. e. double, triple, ... events) at the beginning of the measurement.

are events where two or more markers were within the diffraction limit, on average they exhibit a higher photon number. The correct expectation value of about 380 photons (Fig. 3.3d dashed line) is reached after enough molecules have been bleached to ensure an appropriately sparse sample.

3.1.3 Image Creation

After localization, two parameters are available for each event, its position and the photon number which defines the localization precision (eq. (3.3)). In the last section it was shown that the photon number of each event is drawn from a geometric distribution. Therefore the localizations have dif-

ferent precisions. Three different approaches to create an image of the acquired list of determined positions and detected photons are currently used.

The first one, which will be referred to as *histogram view*, creates a xy-histogram of the data with a bin size half as large as the expected average resolution. The counts in each bin reveal the number of localizations in the corresponding xy region. If each marker is localized many times, the effective PSF is sampled quite well by this approach. The disadvantage is that the available information content is not fully exploited, since events with high photon counts are treated the same as ones with a low photon count.

The second method will be called *Gaussian view*. Each event is represented by a normalized Gaussian localized at its position and with a standard deviation depending on the detected number of photons given by eq. (3.3). The effective PSF in the Gaussian view is broader than in the histogram view. (80). A disadvantage of this method is that it falsely suggests a larger dynamic range of the image to the eye, since it decreases the impact of noise.

The third approach, called *brightness view* (45), is similar to the histogram view with the difference that the bin counts are not event counts, but rather the sum of all photons in that bin is displayed. Indeed it can show the brightness information, but at the cost of losing the information about the number of total events in a bin. Like the histogram view, the brightness view is not capable to fully recover the information of precision.

Note that each of these approaches does not depict the available information completely, a more detailed discussion can be found in (82). In this work the histogram view is employed to create the final image, unless stated otherwise.

Another crucial parameter in SMS image creation is the photon threshold T applied within the localization algorithm. A high threshold entails that only the brightest events are accepted resulting in a better resolution of the final image. This happens at the cost that many events are discarded and the image thus becomes more spotty. Moreover, systematic effects like e.g. the potential dependence of the environment on the photon number have to be considered when evaluating an SMS image. However, the advantage of SMS methods in comparison to the targeted modes is that the resolution can be adapted to the requirements after data acquisition (within certain limits).

The resolution can be compromised if events of higher orders are detected, i. e. , if two or more molecules emit within one Airy disk. This problem can be partially solved by geometric considerations, by employing the photon distribution or by analyzing the detection span of an event. In the first case events are discarded if the diffraction pattern is too elliptical since it most probably features a superposition of more than one molecule. In the second case events with photon counts higher than a certain threshold are removed, since very high photon counts have a higher probability to stem from higher order events. In the last case, events exceeding e.g. twice the mean on-time of all markers are removed. This is justified by the fact that extreme long on-times most probably are caused by two markers overlapping in time. A more detailed discussion can be found in (30, 57).

3.1.4 SMS Toolbox

The crucial components for creating a superresolved 2D-SMS image shall be summarized here.

- **A switchable marker** is required, i. e. a marker with at least two states and a controllable transition. Although here fluorescence is used as the signal and light as the switch, SMS is not restricted to these. Thermally or chemically induced transitions for example can be imagined.

- **A high photon yield in a short time** is desirable, since the resolution enhancement scales with $1/\sqrt{N}$ and the acquisition time is proportional to the average duration of an event.
- **A high signal contrast** between the distinguishable states is required. Already a small signal from the off-state B can exceed a high signal from the on-state A, as most markers are in state B and single markers in state A have to be detected.
- **A high ratio between the off- and on-state** is desirable, since otherwise the labeling density has to be reduced to ensure that only one marker is on within the diffraction limit.
- **A fast and sensitive camera** is advantageous to reduce the acquisition time and improve the SNR.

Briefly, the most important advantages and disadvantages of SMS microscopy compared to RESOLFT shall be summarized. A more detailed description is given in (40, 41, 57).

- **Acquisition time and field of view** are two points which discern both methods. While SMS microscopy is a highly parallelized process where the recording area can be scaled up without compromising recording time, until now most RESOLFT techniques were based on single PSF scanning, implying a quadratic dependence of the acquisition time on the length of a squared field of view. However, RESOLFT has high parallelization potential which will improve the situation in the future (42). When focusing on speed, RESOLFT has a clear advantage. With fast beam scanning in small fields of view video rates in living cells have been demonstrated (83). SMS is limited by the camera speed, which is on the order of ms per frame for appropriate cameras. Future developments in camera technology will improve the situation, e. g. camera-like arrays of APDs have potential of much lower recording times. However, it has to be considered that indeed the emission time of a photon burst can be shortened by increasing the excitation intensity, but only up to a certain limit. Too high intensities augment the bleaching probability, which diminishes the number of emitted photons and thus worsens the resolution.
- **Switching fatigue** is an issue in targeted methods since many switching cycles are required to obtain a superresolved image while in SMS methods one switching cycle per marker is enough.
- **The photon yield**, in contrast, is a limiting factor for SMS microscopy, which requires high photon counts to achieve high resolutions while the resolution of RESOLFT does not directly depend on the photon yield. Already one photon is enough for detection.

3.2 3D-SMS - Breaking the PSF Symmetry

Since one of the foci of this thesis is establishing 3D structure reconstruction below the resolution limit in SMS microscopy by employing two opposing lenses, this section will show how 3D structure can be resolved by SMS systems. Single lens based methods will be introduced and compared with 4Pi-SMS, and its significance will be assessed.

Three-dimensional objects have markers below and above the focal plane, i. e. out of focus, which leads to a broader detection PSF. Indeed thin 3D-structures can also be imaged by a 2D-SMS microscope, although the lateral localization precision for events out of focus is worse. However, the methods introduced in the last section can not recover the information encoded in the z

Table 3.1 PSF simulation parameters

semi-aperture angle	α	64.5°
emission wavelength	λ_{det}	570 nm
refractive index	n	1.515
astigmatism parameter	S	2
biplane defocus	$d_{defocus}$	$\pm 300\text{nm}$
4Pi-SMS phase difference	$\Delta\varphi_b$	$\pi/2$

direction, they just project all events to the same xy-plane. As most cellular structures have a three-dimensional extension and their orientation angles in space are stochastically distributed, a lot of information is lost by the projection process. Thus a meaningful investigation of most cellular structures requires the ability to determine the markers z position.

To determine the z position a z dependent signal which can be analyzed is required. Considering this requirement the standard SMS methods could use the z dependent degree of blurring of the detected marker as signal (cf. Fig. 2.4). However this approach is hampered by two problems:

- **The z dependent PSF broadening is weak** for a range of a few hundred nanometers around the focal plane, i. e. the PSF changes its form very slowly and does therefore not allow a precise z determination for events near the focal plane.
- **The PSF is symmetric about the focal plane**, thus signals from above and below this plane are indistinguishable, which makes a meaningful z determination impossible.

Therefore, three-dimensional marker localization requires modified SMS systems which fulfill the following requirement:

- **The PSF symmetry has to be broken** with respect to the focal plane.
- **A strong z-dependent signal** has to be created.

In the following, schemes addressing these issues will be presented. Afterwards, their potential performance will be discussed. As will become apparent, a 4Pi-based scheme as proposed by Middendorff et. al. (49) is most promising to solve these issues. The subsequently shown PSF simulations are conducted with parameters summarized in table 3.1.

3.2.1 Astigmatism

Z-dependent aberrations can be employed for z determination. Many types of wavefront distortions are possible, but astigmatism is most promising as it clearly breaks the symmetry about the focal plane and therefore allows to differentiate between positions above and below the focal plane. It can be easily implemented in a standard SMS setup by just adding a cylindrical lens in the detection path as shown in Fig. 3.4a (84). The excitation path is similar to that shown in Fig. 2.4a and not illustrated again since it is not necessary for the following discussion. The same also applies to the setups introduced subsequently. The *aberration function* describing the phase factor distribution in the back aperture of the objective, which leads to the distortion of the wavefront, reads as follows (54):

$$\varphi(r, \phi) = \exp[iSr^2 \cos(2\phi)] \quad (3.8)$$

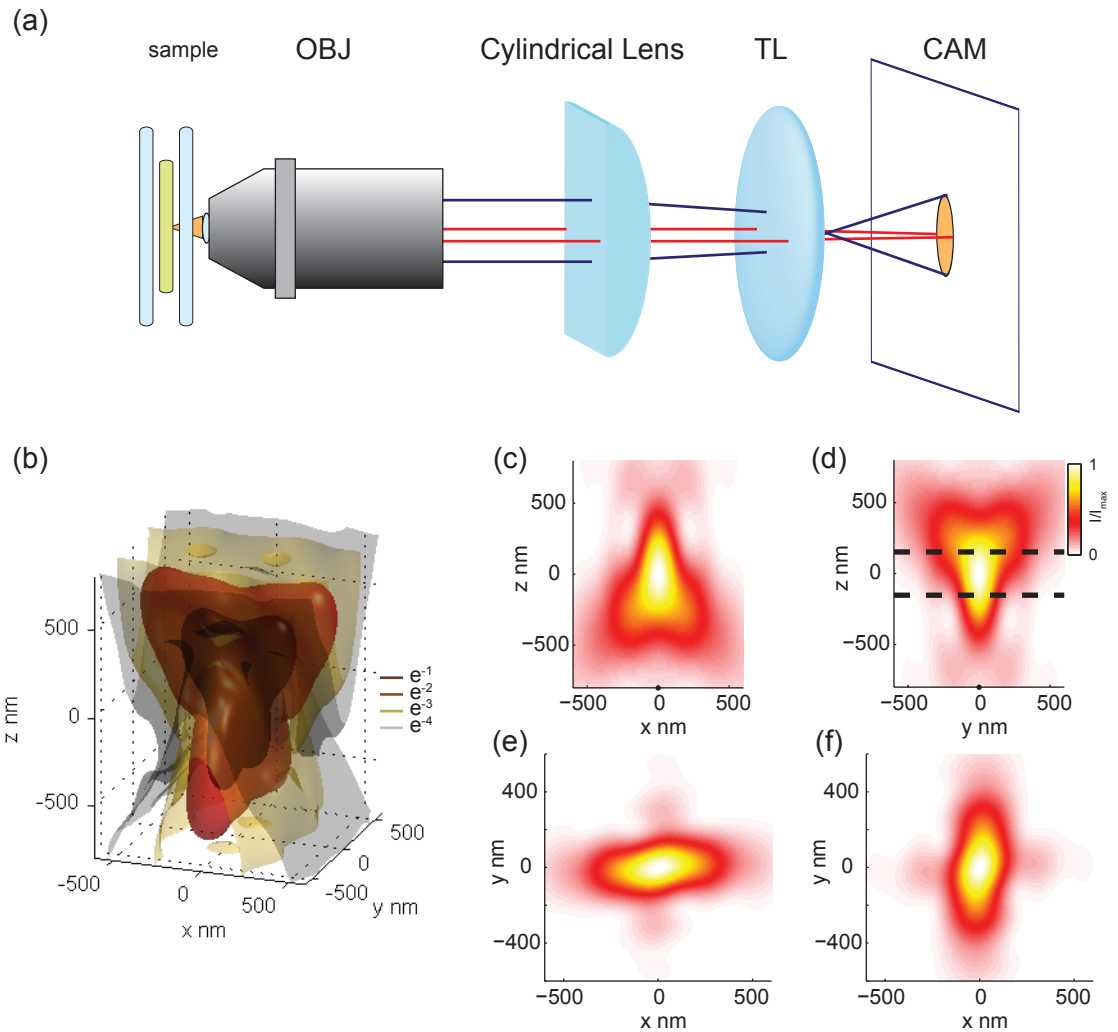


Figure 3.4 (a) Setup of a 3D-SMS microscope based on astigmatism. It basically is similar to a 2D-SMS setup, i. e. a wide-field microscope, with an additional cylindrical lens in the back aperture of the objective, which introduces astigmatism. (b) Simulated PSF of an astigmatism system. The different colors depict isosurfaces at e^{-1} , e^{-2} , e^{-3} , e^{-4} of the maximal intensity. Note that the symmetry about the focal plane is clearly broken. (c) xz -cross-section of the PSF at $y = 0$. (d) yz -cross-section of the PSF at $x = 0$. (e-f) xy -cross-section of the planes indicated by the dashed lines in (d). The ellipse-like xy -cross-section changes its orientation when crossing the focal plane.

Here (r, ϕ) describe the polar coordinates in the back aperture of the objective lens (r is normalized to the aperture size) and S is a parameter characterizing the degree of astigmatism. A simulated PSF is illustrated in Fig. 3.4b-f. The projections obviously reveal that the symmetry about the focal plane is broken removing the ambiguity in z -assignment. Depending on the ellipticity and the orientation of the PSF, a marker can be assigned to an unambiguous z position. The z determination works best around the focal plane, as the aberration leads to a strong z dependence of the signal

in that region. Indeed an axial position determination is possible in this way, but compromising the lateral resolution as can best be seen in Fig. 3.4e-f. The figures reveal xy -cross-sections of the z -planes defined by the dashed lines in Fig. 3.4d. The PSF is clearly elongated either in the x - or y -direction, leading to a worse resolution in the corresponding dimension. The x - and y -resolution are thus inhomogeneous and anisotropic over the whole z range. The first experimental realization of such a setup was implemented by Huang et. al. (44) and uses an astigmatism comparable to $S = 2$. A localization precision of $\sigma_z = 22\text{nm}$ axially and $\sigma_{x,y} = 9/11\text{nm}$ laterally in the focal plane has been reported for immobilized streptavidin molecules doubly labeled with Cy3 and Alexa 647 on a glass surface, yielding 6000 photons on average. Three-dimensional images of microtubules and clathrin-coated pits were demonstrated.

3.2.2 Defocus - Biplane

Another approach images the object at least twice, where the different imaging channels have focal planes which are offset with respect to each other (85). A biplane, i. e. two focal planes, SMS setup is shown in Fig. 3.5a. The difference to a standard SMS setup is that the detection signal is split by a 50:50 beamsplitter (BS) into two arms. The longer path of the reflected arm leads to a different focal plane than the one of the transmitted arm. Simulated detection PSFs of both channels are shown in Fig. 3.5b-c. Fig. 3.5d-e exhibit xz -cross-sections at $y = 0$ of both detection PSFs. The symmetry of each channels about $z = 0$ is obviously broken, since the foci are offset. If the object is centered with respect to the focal planes, each channel displays the same information. If it is closer to one of the focal planes, the PSF becomes more focused in that channel, while it is more blurred in the other one. This behaviour is revealed by the xy -cross-section of the PSFs at a non-centered plane indicated by the dashed lines in Fig. 3.5d-e and shown in Fig. 3.5f-g. The integrated signal over a fixed xy -area of the PSF is used for z determination, since it depends on the blurring of the PSF. For instance, if the image of the marker is highly blurred the signal is small while a focused marker leads to a high signal. Thus a z dependent signal is available and the symmetry about the former focal plane, now the center of both focal planes, is broken. These are the requirements for z determination.

Compared to the former method, the disadvantageous lateral anisotropy, resulting from aberrated detection, is avoided by this approach. The lateral precision remains isotropic. However, since both PSFs are defocused in the central plane, the lateral resolution is worse than in the focused case. Again a tradeoff between axial and lateral precision is intrinsic to the system. Furthermore the z resolution is not homogeneous along the z axis (49). Indeed a more homogeneous z resolution could be achieved by employing additional focal planes, but this compromises the lateral resolution and is also experimentally more sophisticated. It also worsens the SNR in case of non-negligible readout noise of the CCD sensor. Increasing the distance of the two focal planes in a biplane setup worsens the lateral precision and improves the axial one.

This concept for z determination in SMS microscopy was first reported by Juetten et. al. (45) and named biplane fluorescence photoactivation localization microscopy (BP FPALM). They report a lateral and axial FWHM-resolution of 30 nm and 75 nm respectively for caged fluorescein-labeled antibodies on a cover slip. A z range of several μm is demonstrated with a fluorescein labeled bead of 4 μm diameter.

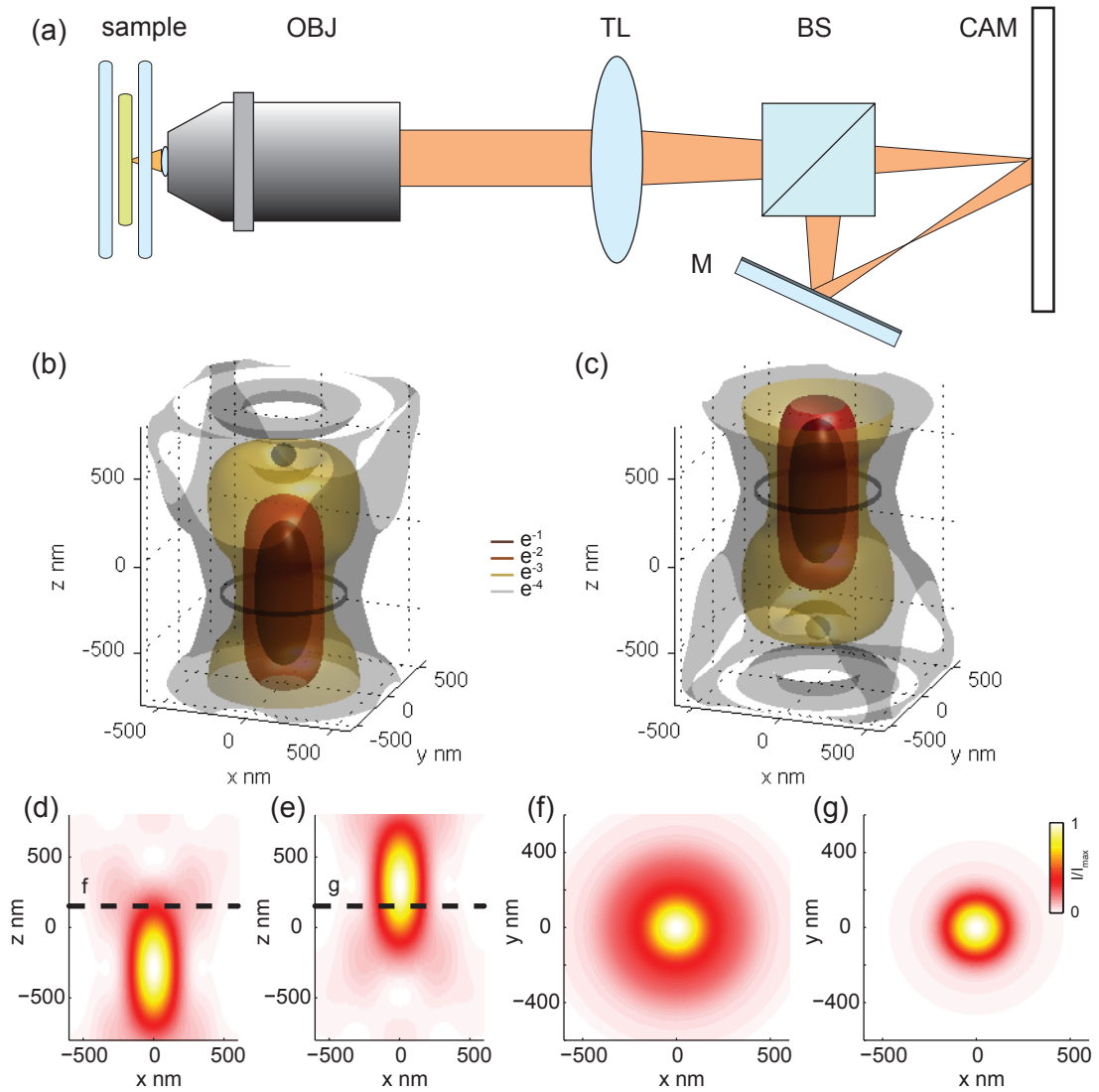


Figure 3.5 (a) Setup of a 3D-SMS system based on two focal planes. The signal of a standard SMS setup is split into two detection channels by a beamsplitter (BS) after the tube lens (TL). The arms create two images with offset focal planes due to the different arm lengths. (b-c) Simulation of the PSFs of both channels. Note the offset of the focal planes, which breaks the symmetry with respect to $z = 0$. (d-e) xz -cross-sections of both channels. (f-g) xy -cross-sections of the dashed lines in (d-e). The signals have a different shape and are rotationally symmetric about the z -axis.

3.2.3 Double Helix

A further concept was implemented by Pavani et. al. and called double helix point spread function (DH-PSF) (86). It basically uses a phase mask in the Fourier plane of the object to create a PSF whose z dependence features a double helix. The setup is illustrated in Fig. 3.6a. The spatial light modulator (SLM) placed in a Fourier plane creates the required phase mask, whose functional

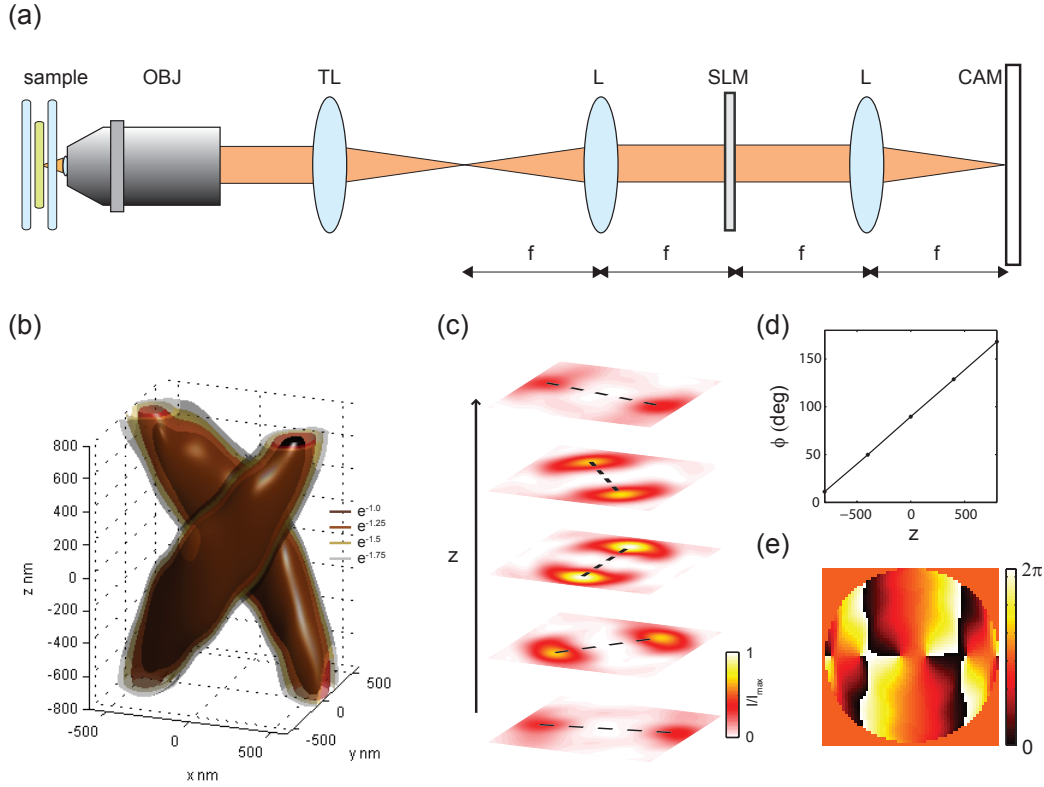


Figure 3.6 (a) DH-PSF setup. A $4f$ lens system images the image of a standard SMS setup on a camera. An SLM is placed in the Fourier plane of the $4f$ system to create the double helix PSF. (b) Simulation of the double helix PSF. (c) xy -cross-sections of the PSF for different z planes. (d) Polar angle (ϕ) defined by the connection between the two helix lobes (dashed lines in c) in dependence of z . (e) Phase mask created by the SLM.

form is obtained by an optimization algorithm considering certain constraints (87) and normally is a super position of different Gauss-Laguerre modes. The simulated PSF of such a system is sketched in Fig. 3.6b. Again it reveals a non-symmetric intensity distribution about the focal plane. This becomes even more apparent in Fig. 3.6c, which exhibits different cross-sections of the double helix along the z -axis. The polar angle ϕ between both lobes is shown in Fig. 3.6d as a function of z . Symmetry breaking and creation of a z dependent signal is again established and the z position of a marker can be determined. An axial resolution of $\sigma_z = 20\text{nm}$ for 9300 detected photons from single molecules embedded in a poly methyl methacrylate (PMMA) film in the focal plane has been reported at a frame rate of 500ms. Furthermore an axial field of view (fov) of about $2\mu\text{m}$ can be achieved.

The z position in a DH-PSF setup can be assigned unambiguously over an axial range corresponding to a polar angle between 0 and π . If a larger z range is desired, the phase pattern has to be adapted to axially extend the DH-PSF. The polar angle thus characterizes a larger axial range, however as a fixed angle difference $\Delta\phi$ now covers a larger z range, the precision of z determination worsens. Therefore a compromise between axial field of view (fov) and resolution has to

be found. A further drawback is that the double helix pattern, rather than the airy disk, limits the area in which only one marker can be in its on-state. Since the double helix PSF has an extension approximately 3-4 as large as the Airy disk, a single marker covers a 9-16 times larger area. This directly translates into a 9-16 times higher acquisition time. Furthermore a sophisticated pattern recognition algorithm is required to identify both lobes corresponding to the same marker. Another issue is the low quantum efficiency of the system due to the SLM. The transfer functions of optimized double helix PSF systems achieve efficiencies of less than 60% (87). The SLM leads to further losses. The total detection efficiency is typically less than 25% (86). Probably all these drawbacks prevented DH-PSF from recording superresolved images of biological samples and limited its applications to quantum dot particle tracking so far (88).

3.2.4 Theory of 4Pi-SMS

In section 2.1.5 it was shown that 4Pi improves the z resolution in conventional microscopy by a factor of 3-7 by employing a second lens. The 4Pi concept was already applied to the targeted methods and lead to STED with an isotropic resolution of 40nm (isoSTED) (48). Middendorff et. al. studied the potential information content within a system combining the 4Pi and SMS techniques (49). The underlying setup is sketched in Fig. 3.7a. It basically consists of a 4Pi cavity (cf. section 2.1.5) which coherently adds the electric fields \mathbf{E}_a and \mathbf{E}_b emitted by a fluorophore and collected by the objectives a and b. For the subsequent discussion, the absolute phase difference $\Delta\varphi_a$ of both arms is set to $-\pi/2$ without loss of generality. The 4Pi cavity is followed by an additional cavity which introduces a further phase difference $\Delta\varphi_b$ between the output fields \mathbf{E}_1 and \mathbf{E}_2 of the first cavity, generating two further electric fields \mathbf{E}_3 and \mathbf{E}_4 . Finally, these electric fields are imaged onto an EMCCD generating four distinct signal channels. Fig. 3.7b-c reveal xz -cross-sections of simulated PSFs for each channel. $\Delta\varphi_b$ was set to $\pi/2$ in the simulations. Clearly a strong z -dependence in each channel is visible. While the channels 1 and 2 are symmetric about the focal plane, the symmetry is broken for the channels 3 and 4. Thus again the requirements for a z determination are fulfilled for such a setup. Note that the z modulation in this system is much stronger than in systems presented before, promising an improved z resolution compared to former techniques. Fig. 3.7d-e reveal xy -cross-sections of the focal plane of each PSF and the corresponding central profiles. The presented cross-section exhibit rotational symmetry, which is valid for the whole z range. Thus an isotropic lateral resolution along the z axis can be expected. The second objective lens doubles the number of detected photons, which directly translates into a lateral resolution enhancement of $\sqrt{2}$. The second cavity is required for two reasons. Firstly, symmetry breaking in the case of $\Delta\varphi_a = -\pi/2$, is only possible by an additional channel (Fig. 3.7c). Secondly, the z -modulation around the maxima and minima is very weak, leading to a worse or even diverging z resolution. The phase $\Delta\varphi_b$ is chosen in a way that the modulation in the additional channels is maximal at these locations (Fig. 3.7b,c).

3.3 Information Content

Having presented different concepts to realize z determination in SMS microscopy, they shall be compared more quantitatively in this section to identify the most promising technique. An established method to assess the performance of an imaging system is employing *Fisher information* and the *Cramer-Rao-uncertainty* to explore the information content of the system. These statisti-

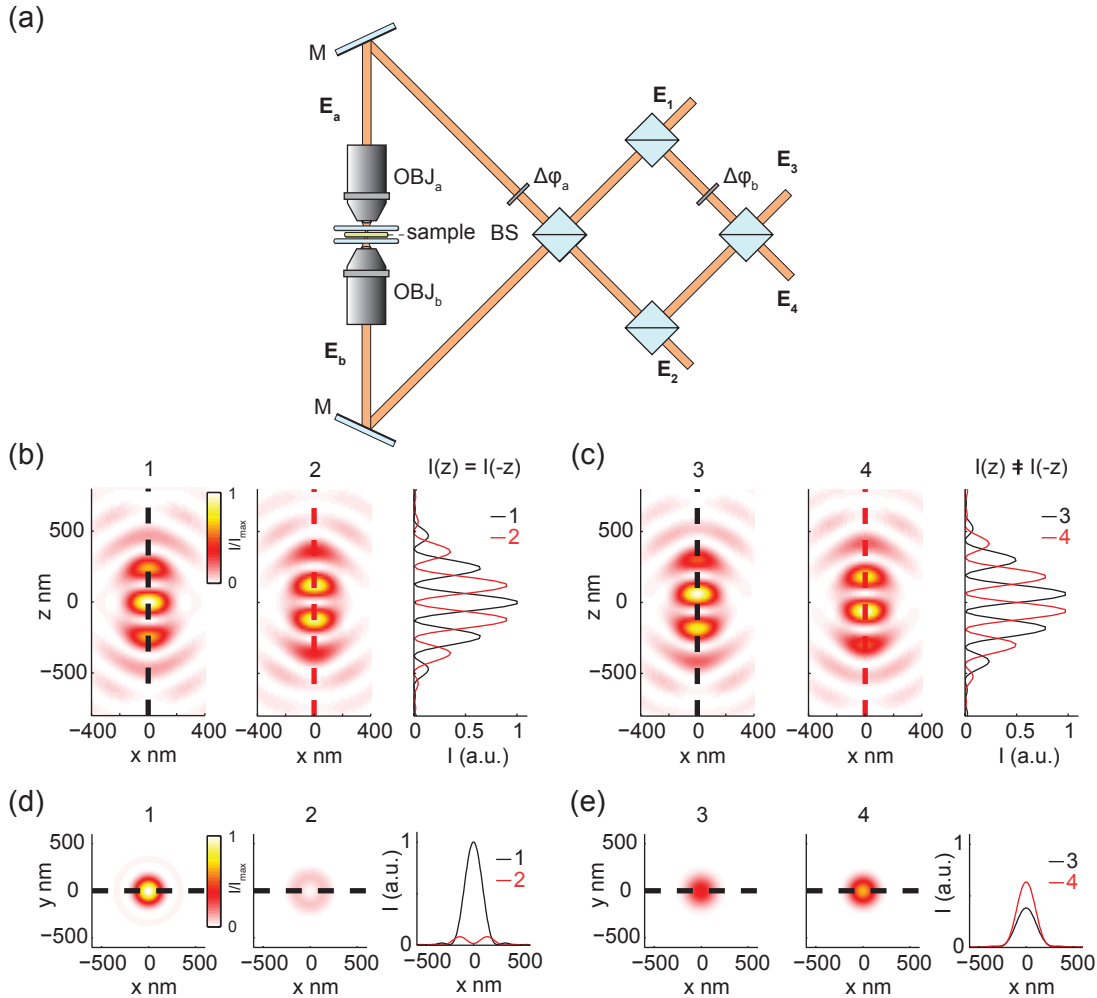


Figure 3.7 (a) A potential realization of a 4Pi-SMS setup. It comprises a 4Pi cavity and an additional cavity followed by a wide-field detection (not shown). The electric fields \mathbf{E}_a and \mathbf{E}_b emitted by a fluorophore are collected by the objectives a and b. The fields interfere at the first BS with the absolute phase difference $\Delta\varphi_a$ and create the electric fields \mathbf{E}_1 and \mathbf{E}_2 . Another interference with the phase difference $\Delta\varphi_b$ between the fields \mathbf{E}_1 and \mathbf{E}_2 in the subsequent cavity generates the electric fields \mathbf{E}_3 and \mathbf{E}_4 . Each electric field corresponds to one detection channel. (b-e) Simulated PSFs of the four detection channels ($\Delta\varphi_a = -\pi/2$, $\Delta\varphi_b = \pi/2$). (b) PSFs of channel 1 and 2 and the profiles defined by the dashed lines. Both channels are symmetric about the focal plane. (c) PSFs of channel 3 and 4 and profiles defined by the dashed lines. The PSFs are asymmetric about the focal plane and thus break the symmetry for a 4Pi-SMS system. (d-e) *xy*-cross-sections of the focal plane for each channel and the corresponding central profiles. Note the different intensities and the rotational symmetry about the *z* axis in each channel.

cal methods have been applied to SMS systems in different studies, which will be summarized in the following (49, 89).

Table 3.2 Fisher Information parameters

semi-aperture angle	α	64.5°
emission wavelength	λ_{det}	575 nm
average detected photons	N_{ph}	250
background per pixel	b	1/250
astigmatism parameter	S	3
distance of focal planes	d_{BP}	600 nm
average detected photons for 4Pi	$N_{ph,4Pi}$	500
background per pixel 4Pi	b_{4Pi}	1/500

The differential information content of each channel k of a system is given by

$$\mathbf{i}_{ij,k}(\mathbf{r}) = \frac{[\partial_i h_k(\mathbf{r})][\partial_j h_k(\mathbf{r})]}{h_k(\mathbf{r}) + b} \quad (3.9)$$

with h_k the PSF of channel k and b the average background in photons per pixel normalized by the total signal (49). The PSFs are normalized as follows,

$$\sum_k \int h_k(\mathbf{r}) dx dy = 1 \quad (3.10)$$

The differential information content is thus proportional to the derivative of the PSF, i. e. it depends on its modulation strength. It can be shown that for symmetric PSFs about the xz and yz planes, the off-diagonal elements vanish, leading to a diagonal Fisher information matrix \mathbf{I} ,

$$\mathbf{I}_{ii}(\mathbf{r}) = N \int \sum_k \mathbf{i}_{ii,k} dx dy =: NI_i(z) \quad (3.11)$$

N denotes the expectation value for the total number of photons detected in all channels and $I_i(z)$ is defined as the photon-number-normalized information content. The Cramer-Rao-uncertainty is given by

$$\sigma_i(z) \geq \frac{1}{\sqrt{NI_i(z)}} \quad (3.12)$$

For a given average number of detected photons and a given background level this equation gives a lower bound for the variance of any unbiased position estimation procedure. The last equation presents two important points. Firstly, as expected, the lower bound of localization precision scales with $1/\sqrt{N}$. Secondly, it is inversely proportional to the square root of the normalized information content, i. e. a weak modulation of the PSF raises the lower bound for the precision of the position determination while a strong modulation lowers the bound. This already suggests that 4Pi-SMS should perform best, as the modulation strengths of its PSFs are much stronger compared to the other techniques.

Middendorff et. al. theoretically studied the Cramer-Rao-bounds for the following SMS systems: an ordinary wide-field detection, a biplane detection, an astigmatism-based technique and a 4Pi-SMS system (49). The parameters of the simulations are listed in table 3.2. The most important results of these studies are summarized in Fig. 3.8. First, the lateral resolution shall be

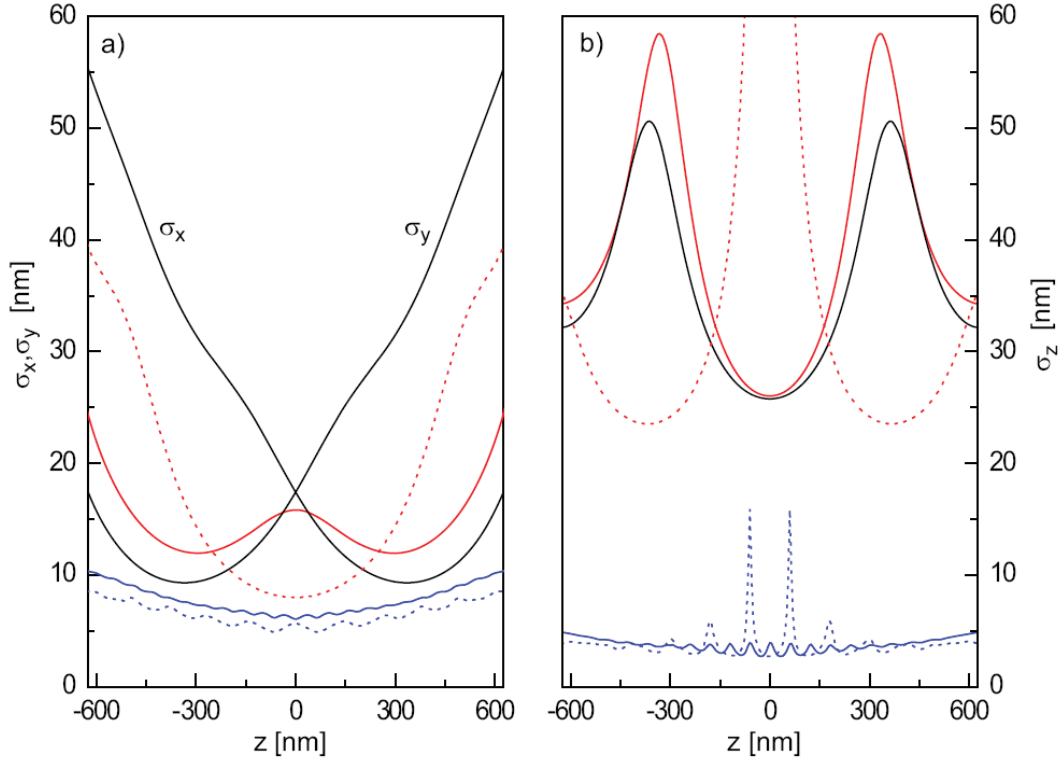


Figure 3.8 (a) Lateral Cramer-Rao bounds σ_x , σ_y and (b) axial Cramer-Rao bounds σ_z for the interferometric detection scheme (blue) in comparison to the biplane setup (red) and an astigmatism system (black). The parameters of the systems are summarized in table 3.2. The Cramer-Rao bounds for interferometric detection using just one beamsplitter and two channels is also shown (blue, dotted). The bounds for a wide-field detection in a single channel are indicated by red dotted lines. Introducing more channels can lower the radial precision due to a smaller signal-to-noise level. (Figure courtesy of Middendorff et. al. (49))

discussed which is shown in Fig. 3.8a. The standard 2D-SMS-setup (red, dotted line) achieves its best resolution in the focal plane $z = 0$. Out of focus the lateral resolution worsens, as the PSF gets more blurred. The astigmatism scheme (black lines) has different dependencies for the x and y direction. While σ_y has a minimum below the focal plane, the minimum of σ_x lies above it. At the optimum of one axis, the other axis has a rather bad resolution. This behavior is explained by the ellipticity of the PSF whose orientation is rotated by 90° when passing the focal plane (cf. Fig. 3.4). The biplane detection system (red line) has its best lateral resolution at both focal planes, while at $z = 0$, i. e. between the focal planes, the resolution decreases, due to blurring. Solely the 4Pi-SMS setup (blue line) shows an almost homogeneous lateral resolution along the z axis, which is also better due to the doubled number of detected photons. The blue dotted line corresponds to a 4Pi scheme with only two channels. The lateral resolution is a bit better compared to the four channel system, as distributing the signal to four channels instead of two worsens the SNR.

The axial resolution is shown in Fig. 3.8b. The resolution of the 2D-SMS-setup diverges at the

Table 3.3 3D-SMS techniques. Properties and resolutions for $N = 250$ photons.

	isotropic	homogeneous	xy -isotropic	$\sigma_{x,y}$ (nm)	σ_z (nm)
astigmatism	no	no	no	10/35	25
biplane	no	no	yes	12	25
DH-PSF	no	yes	almost	10/15 ¹	30 ¹
4Pi-SMS	(no) ²	yes	yes	7	3

focal plane, since the modulation of the PSF vanishes at $z = 0$. Note that although a resolution is given for other z locations, a 2D-SMS-system is not capable of unambiguously determining the correct z position, since the symmetry is not broken. The Fisher information matrix only studies the potential local precision available in the PSF rather than global properties like symmetry. Furthermore it does not provide a scheme how to extract the information from the system. The axial resolutions of the astigmatism and the biplane scheme are comparable and are best at the focal plane with $\sigma_z \approx 25\text{nm}$. Out of focus, the resolution strongly deteriorates leading to an inhomogeneous precision along the z axis. In contrast, the 4Pi-SMS concept has an almost homogeneous resolution along the axial direction and has a precision of $\sigma_z < 5\text{nm}$, i. e. more than a factor of 5 better than the other techniques. The blue dotted line again represents the two-channel 4Pi-system. The peaks in the axial resolution occur when the modulation almost vanishes, i. e. at the maxima and minima of the PSF (cf. Fig. 3.7b). Therefore, at least three channels are required to flatten these peaks.

Another study employing Cramer-Rao-bounds compares the double helix concept with an astigmatism and biplane system (89). Since the underlying parameters are not the same as in previous investigations, a comparison to former results has to be done carefully. However, the performance of the three single-lens-based systems can be compared to each other. If the Cramer-Rao-bounds of both studies should be compared, the results from the latter study has to be multiplied by a factor of $\sqrt{N_B/N_M}$ to correct for the distinct number of detected photons, where N_B and N_M are the number of photons employed by Badieirostami et. al. and Middendorff et. al. respectively. The main conclusions of latter investigation are, that DH-PSF has homogeneous axial and lateral resolutions along the z axis over a range of about $2\mu\text{m}$ in contrast to the inhomogeneous resolutions of astigmatism and biplane systems. Comparing the best lateral resolutions the DH-PSF is a bit worse than the other methods, however as it is almost homogeneous it provides this precision over the whole $2\mu\text{m}$ in contrast to the other techniques. The best axial resolutions are also comparable, but again astigmatism and biplane are unable to maintain the precision over the whole range. Note that this theoretical study assumed the same number of detected photons in each single-lens-based method, but experimentally the DH-PSF system is hampered by a strong attenuation of the light due to the employed SLM. Furthermore the 9-16 times larger extension of the DH-PSF demands a 9-16 times longer recording time (cf. section 3.2.3).

Finally, the conclusions of this section shall be summarized (see also table 3.3). The only method which has the potential to provide homogeneous and isotropic lateral resolution is 4Pi-SMS. DH-PSF has an almost homogeneous lateral resolution along the z axis but it is not perfectly isotropic. The other two single-lens-based methods do neither exhibit isotropic nor homogeneous lateral resolution along the z -axis. A 4Pi-SMS system has a $\sqrt{2}$ better xy -determination as the number of collected photons is doubled by the second objective.

All single-lens-based techniques presented here have in common that the axial precision is ap-

proximately three times worse than its lateral counterpart. As already discussed in section 2.1.5 less than half of the detection aperture is used by a single lens, which leads to an elongation of the PSF along the z axis. Therefore, its axial features are not as steep as the lateral ones. Employing the second lens addresses this drawback. The theoretical axial resolution of a 4Pi-SMS clearly outperforms all other single-lens-based techniques by an approximately 6-fold improvement. At the same time there is no tradeoff between lateral and axial precision as in the other aberration based techniques. Furthermore the fov range and precision along the z axis are independent in 4Pi-SMS, in contrast to the single-lens-based methods, where fov range and precision are correlated. Besides, 4Pi-SMS theoretically provides almost uniform precision of axial localization over the whole range. For 250 photons per event it should offer localization precisions below 10 nm in all three dimensions.

¹photon number corrected value taken from Badieirostami et. al. (89)

²In 4Pi-SMS the anisotropy is due to the superior z resolution, rather than an inferior z resolution.

Chapter 4

4Pi-SMS - The Nanoscope

Considering the theoretical resolution enhancement which can be achieved by a 4Pi-SMS microscope, the focus of this work is to experimentally implement such a setup and to investigate how the potential information content of such a system can be exploited. Moreover, the setup design readily allows a multicolor expansion, which is of high interest for many biological applications. In the following chapter the developed 4Pi-SMS system underlying this thesis is going to be introduced.

As described in detail below, in the present setup, four detection channels are created in which the fields through the objective lenses a and b interfere with different relative phases. This is achieved by different phase delays of the p (parallel to plane of incidence, E_x) and s -polarized light in the interferometer arms. Moreover, the multi-color measurements use a dichroic mirror to make the intensity ratio between the p and the s -polarized channels dye specific and use this to identify the dye species during the measurement.

4.1 The Setup

The experimental setup is sketched in Fig. 4.1a. It basically consists of a triangular 4Pi cavity (15) with an additional achromatic quarter-wave plate and a modified Babinet-Soleil compensator in each leg of the triangle. The optical axes of the quarter-wave plates and the setup plane draw an angle of 45° , ensuring that the fluorescence light ends up with nearly equal probability in the s - and p -polarized channels irrespective of the fluorophore's dipole orientation. The Babinet-Soleil compensators retard the phase of the p -component of the fluorescence light with respect to its s -polarized component within both leg a and leg b by $\Delta\varphi_a$ and $\Delta\varphi_b$ respectively, thus creating time-separated fluorescence wave packages with mutually orthogonal polarization (Fig. 4.3).

After interference at the neutral beamsplitter, the ensuing optical elements spatially separate the wave packages into four detection channels $s,1;s,2;p,1;p,2$, and project them onto a single EMCCD camera (IXON-Plus DU-897, Andor Technology) in a 2×2 grid pattern. In this scheme, each fluorescence photon can pass through both lenses (63X PL APO N.A. 1.20 water immersion, Leica microsystems) simultaneously, self-interferes at the beamsplitter, and thus can be detected with certain probabilities in any of the four channels. Note that the physically relevant phenomena take place up to the beamsplitter (BS), the components following the beamsplitter merely facilitate the convenient use of a single camera. Therefore, the superimposed intermediate image pairs $p,1/s,1$ and $p,2/s,2$, generated by the tube lenses (L1), are clipped by the variable rectangular apertures (Ap) to fill one quadrant each of the EMCCD chip in parallel. The polarizing beamsplitter (PBS) interchanges the partners of the image pairs which are then imaged via lenses L2, L3, the metalized prism (MP), a notch filter rejecting the excitation light, and a bandpass filter (N/BP) onto the

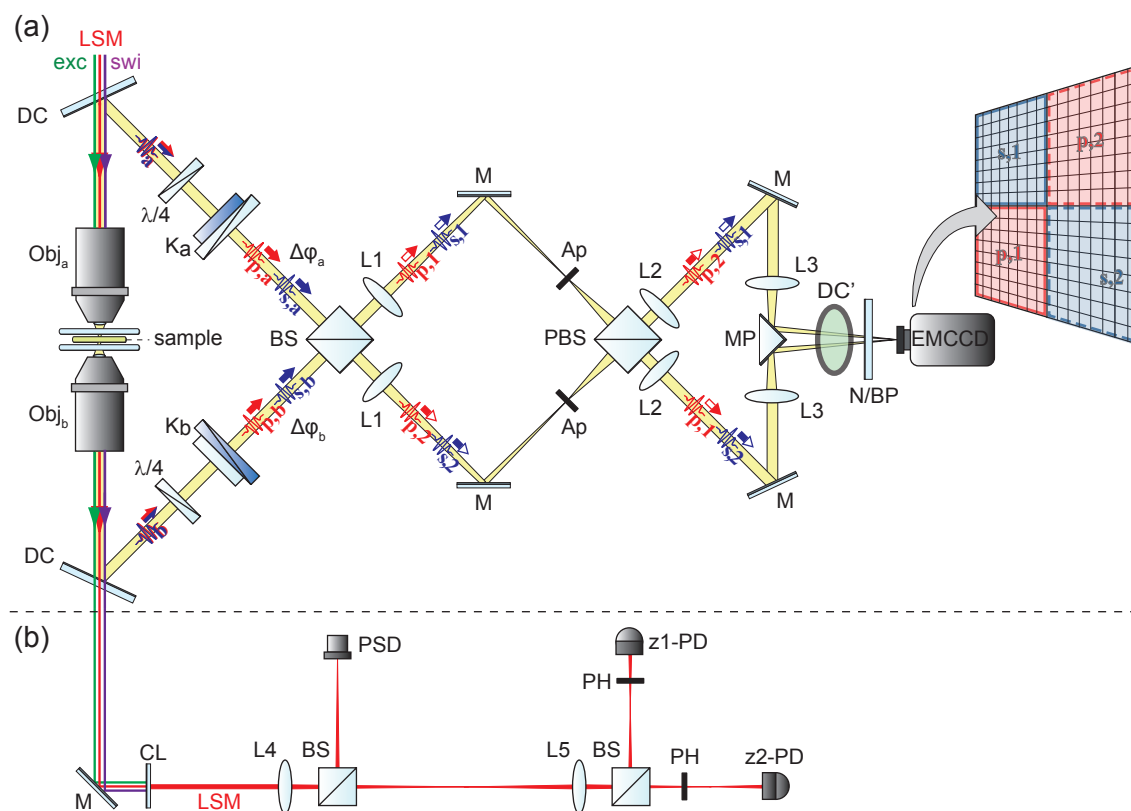


Figure 4.1 (a) 4Pi SMS microscope. The sample is sandwiched between two cover slips. Illumination for excitation (exc) and on-off-switching (swi) occurs through the upper of the two water immersion objective lenses. The 4Pi cavity consists of two dichroic mirrors (DC), two quarter wave plates ($\lambda/4$), two modified Babinet-Soleil compensators (K_a & K_b) and a neutral beamsplitter (BS). The superimposed intermediate image pairs $p_{1/s,1}$ and $p_{2/s,2}$, generated by the tube lenses (L1), are clipped by the variable rectangular apertures (Ap) to fill one quadrant each of the EMCCD chip in parallel. The polarizing beamsplitter (PBS) interchanges the partners of the image pairs which are then imaged via lenses L2, L3, the metalized prism (MP), a notch and a bandpass filter (N/BP) onto the camera. The mirrors (M) are tilted to spatially separate the four detection channels. For the multicolor measurements, an additional dichroic (DC') is inserted in front of the camera. (b) The stabilization module. An optical system creating a signal characterizing the relative position of the objectives a and b and thus allowing to focus them onto the same point. An additional collimated laser beam (LSM) is focused by objective Obj_a . Objective Obj_b and lens (L4) image the generated focal spot on a position sensitive diode (PSD) to track relative xy -deviations of both objectives. The relative z -motion is detected by an additional lens (L5), a beamsplitter and two pinholes (PH) and photo diodes (PD).

camera. The mirrors (M) are slightly tilted to spatially separate the four detection channels. For the multicolor measurements an additional dichroic (DC') is inserted in front of the camera.

Fig. 4.1b presents the stabilization module, an optical system to measure the relative position of the objectives a and b and thus allowing to minimize the relative displacement between them to stabilize the cavity. An additional collimated laser beam (LSM) is focused by objective a

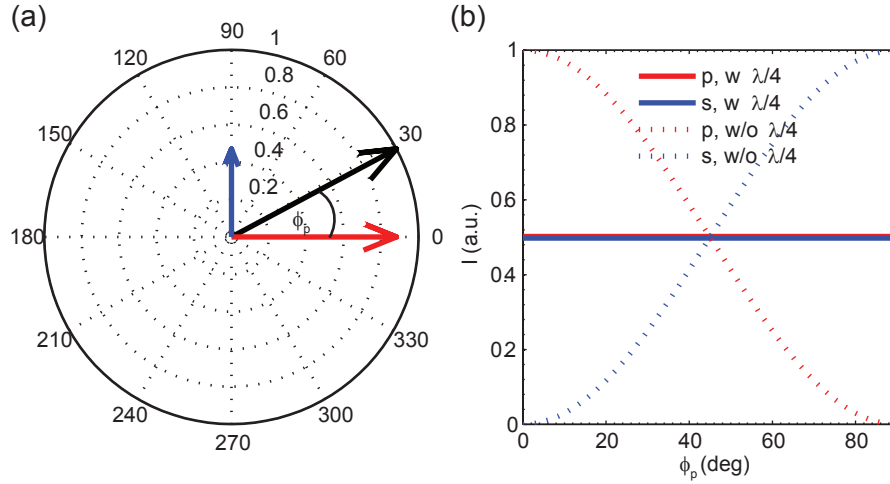


Figure 4.2 (a) Linearly polarized light (black vector) with an angle ϕ_p to the x -axis and the corresponding s - and p -component (blue, red). (b) Intensity dependence of the s - and p -component on the angle ϕ_p . The dependence without a $\lambda/4$ -plate (dotted lines) vanishes when introducing a $\lambda/4$ -plate at an angle of $\chi = 45^\circ$ to the x -axis (bold lines).

(Obj_a). The objective b (Obj_b) and lens (L4) image the generated focal spot on a position sensitive diode (PSD) to track the relative xy -deviations of both objectives. A beamsplitter before the PSD creates a second beam which allows the detecting of relative z motions of both objectives. An additional lens (L5), a beamsplitter, two pinholes (PH) and photo diodes (PD) provide the necessary signals. The axially shifted positions of the pinholes in front of the detecting PDs lead to a z dependent signal. A PID-controller implemented in LABVIEW evaluates the signals and adjusts the position of objective b which is mounted on an xyz -piezo stage. A more detailed description of the stabilization module is given in appendix C.

4.2 The Cavity

4.2.1 Dipole Orientation

Unless the emitters rotate fast compared to the timescale of the fluorescence emission during a single *off-on-off* cycle, which is in the order of milliseconds, both the intensity and polarization of the detected fields will depend on the azimuthal and polar orientations of the fluorescence emitting dipole. For example, an x -oriented dipole would be detected almost exclusively in the p -polarized channels, a y -oriented one in the s -polarized channel and a dipole oriented along the z -axis would create equal intensities in both channels. To avoid the concomitant orientation-dependent bias, $\lambda/4$ plates with the crystal optical axis oriented at 45° against the x -axis were introduced in the exit pupil of the lens. The Jones matrix $T(\chi)$ of the $\lambda/4$ -plate with an angle χ between the fast axis and x -axis can be written as.

$$\mathbf{T}(\chi) = \mathbf{R}^{-1}(\chi)\mathbf{T}'\mathbf{R}(\chi) \quad (4.1)$$

with the matrix \mathbf{R} describing the rotation of the coordinate system by an angle χ ,

$$\mathbf{R}(\chi) = \begin{pmatrix} \cos\chi & \sin\chi \\ -\sin\chi & \cos\chi \end{pmatrix} \quad (4.2)$$

and the Jones matrix of a $\lambda/4$ -plate with the fast axis along the x-axis,

$$\mathbf{T}' = \begin{pmatrix} 1 & 0 \\ 0 & -i \end{pmatrix} \quad (4.3)$$

As mentioned above, χ is set to 45° and \mathbf{T} thus reads,

$$\mathbf{T} = \frac{e^{-i\pi/4}}{\sqrt{2}} \begin{pmatrix} 1 & i \\ i & 1 \end{pmatrix} \quad (4.4)$$

Fig. 4.2a shows a black vector representing linearly polarized light with an angle ϕ_p with respect to the x -axis, the corresponding s - and p - components are indicated by the blue and red vectors. Fig. 4.2b reveals the dependence of the components on ϕ_p without the $\lambda/4$ -plate, dotted lines and with the $\lambda/4$ -plate. The dependence on ϕ_p obviously vanishes in the last case. Linearly polarized light thus exhibits equal p -polarized and s -polarized parts before the beamsplitter.

Let $\mathbf{a}(r, \phi, \theta_p, \phi_p, z)$ be the field created by a dipole located on the optic axis at $(0, 0, z)$ and oriented along $\mathbf{p} = (\sin\theta_p \cos\phi_p, \sin\theta_p \sin\phi_p, \cos\theta_p)$ at position $\mathbf{r} = (r \cos\phi, r \sin\phi)$ in the exit pupil of the lens. Here, $0 \leq r \leq \sin\alpha$ and α is the semi-aperture angle of the lens. Due to the cylindrical symmetry of the lens one obtains,

$$\mathbf{a}(\phi, \phi_p) = \mathbf{R}^{-1}(\phi_p)\mathbf{a}(\phi - \phi_p, 0), \quad (4.5)$$

where the dependence on θ_p , r and z is implicit. The field in the exit pupil after passing the $\lambda/4$ plate is then given by

$$\mathbf{A} = \frac{e^{i\pi/4}}{\sqrt{2}} \begin{pmatrix} 1 & i \\ i & 1 \end{pmatrix} \mathbf{a} \quad (4.6)$$

Considering eq. (4.5) this yields

$$\mathbf{A}(\phi_p + \phi, \phi_p) = \begin{pmatrix} e^{i\phi_p} & ie^{i\phi_p} \\ ie^{-i\phi_p} & e^{-i\phi_p} \end{pmatrix} \mathbf{a}(\phi, 0) \quad (4.7)$$

Now, again due to the symmetry of the lens, \mathbf{a} is mirror symmetric about the dipole's projection into the xy -plane and therefore

$$\mathbf{a}(-\phi, 0) = \begin{pmatrix} 1 & 0 \\ 0 & -1 \end{pmatrix} \mathbf{a}(\phi, 0). \quad (4.8)$$

Inserting this in eq. (4.7) gives,

$$\mathbf{A}(\phi_p - \phi, \phi_p) = \begin{pmatrix} e^{i\phi_p} & -ie^{i\phi_p} \\ ie^{-i\phi_p} & -e^{-i\phi_p} \end{pmatrix} \mathbf{a}(\phi, 0) \quad (4.9)$$

Comparing eq. (4.9) and eq. (4.7) shows that the x - and y - components of \mathbf{A} are related by,

$$A_y(\phi_p + \phi, \phi_p) = i e^{-2i\phi_p} A_x(\phi_p - \phi, \phi_p). \quad (4.10)$$

Thus, the s -polarized field equals the p -polarized field mirrored about the polar dipole orientation and multiplied by a constant phase that depends on the dipole orientation. Therefore, the intensity ratio of the s and p channels as well as the ratio and z -dependence of the (cylindrically symmetric) weighted moments introduced below are independent of the polar orientation of the dipole.

Note that the polar orientation (θ_p) changes the shape of \mathbf{a} but not its phase (90). Nevertheless, it generates images with the center of mass shifted away from the geometric focus for moderate tilts and ring-like images for z -oriented dipoles. For completely static dipoles, a minor influence on the analysis described below can therefore not be excluded and a careful quantification of this effect will be the subject of further studies. Note that the effect is not limited to the axial position estimation, and should be assessed for 2-dimensional SMS experiments as well.

4.2.2 4 Channel Detection

Both arms a and b of the cavity are shown in Fig. 4.3a-b, respectively. The $\lambda/4$ -plates are orientated at an angle of $\chi = \pm 45^\circ$ in the arms b and a respectively. The different sign in both arms is to compensate the helicity change caused by the additional reflection in one arm when combining both paths at the beamsplitter. Compensator K_a consists of a parallel BK7 plate and two quartz wedges, while compensator K_b consists of a parallel quartz plate and two BK7 wedges. The birefringent quartz crystal has distinct refractive indices for the p - and s -components, with $n_p > n_s$ inferring a delay of the p -polarized components. The crystal thickness is chosen such that the s - and p - wave packets are clearly separated in time, i. e. by more than the wave packet's coherence length of about 20-30 μm . Thus the s - and p -wave packets cannot interfere anymore. By varying the thickness of the plate made up by the two quartz wedges, the relative phase delay behind the objective a ,

$$\Delta\varphi_a(d) = \varphi_{pa} - \varphi_{sa} \quad (4.11)$$

can be precisely tuned. The phase delay between both polarizations in arm b ($\Delta\varphi_b = \varphi_{pb} - \varphi_{sb}$) is defined by the thickness of the quartz crystal and is fixed. By varying the thickness of the variable BK7 plate made up of the two BK7 wedges behind objective b , the overall dispersion within the 4Pi triangle can be corrected. To determine the z -position with high precision, the 4Pi cavity is adjusted such that:

- The electric field from an emitter located in the common focal plane of both objective lenses ($z = 0$) features the same phase difference between both s - and p -polarization wavefronts at the beamsplitter, independent of the emission wavelength and the position of the marker in the focal plane,
- The phase delays between p - and s -polarizations in both arms obey the following equation: $\Delta\varphi_a - \Delta\varphi_b = \pi/2$.

The last equation ensures that the information content is maximized by generating an equidistant phase delay between the four channels ($0, \pi/2, \pi, 3/2\pi$), since it implies,

$$\Delta\varphi_s - \Delta\varphi_p = \pi/2 \quad (4.12)$$

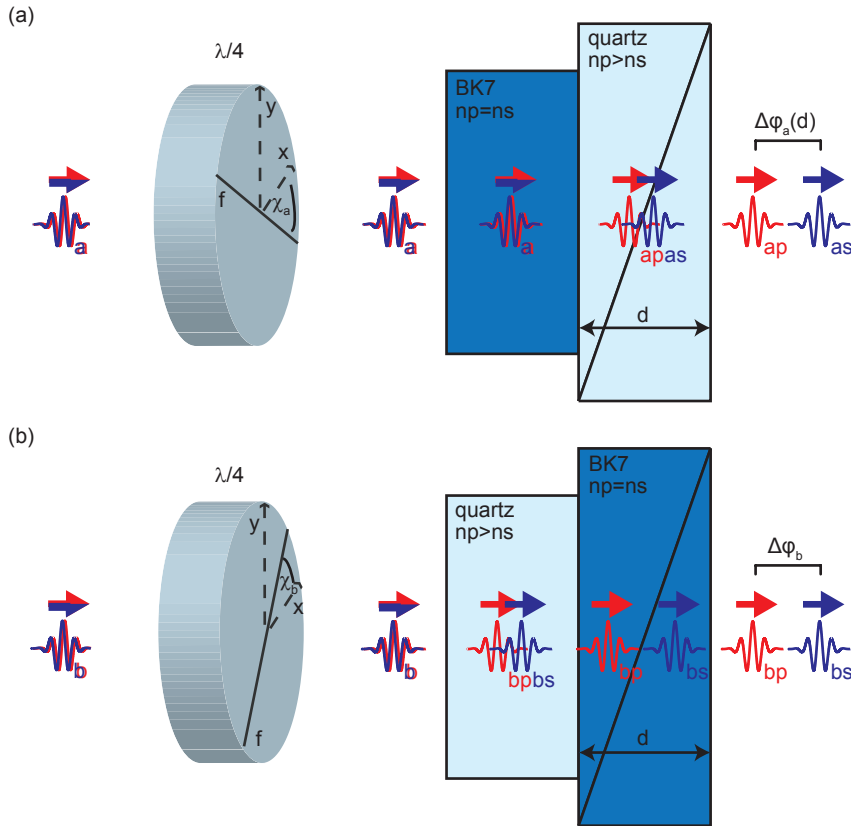


Figure 4.3 Two $\lambda/4$ -plates and a pair of modified Babinet-Soleil compensators as used behind the two objective lenses Obj_a and Obj_b . (a,b) Cavity arm a and b, respectively. The $\lambda/4$ -plates create s -, p - components of equal strength independent of the emitter's emission dipole orientation. Compensator K_a consists of a parallel BK7 plate and two quartz wedges, while compensator K_b consists of a parallel quartz plate and two BK7 wedges. The s - and p -component are separated in space by the birefringent quartz crystals. By varying the thickness of the plate made up by the two quartz wedges, the phase delay behind the lens Obj_a can be precisely tuned to achieve $\Delta\varphi_s - \Delta\varphi_p = \pi/2$. By varying the thickness of the variable BK7 plate made up of the two BK7 wedges behind lens Obj_b , the overall dispersion within the 4Pi triangle can be corrected.

with the phase differences $\Delta\varphi_\kappa$ for each polarization ($\kappa = s, p$) defined as,

$$\Delta\varphi_\kappa = \varphi_{\kappa b} - \varphi_{\kappa a} \quad (4.13)$$

The xy position independence of the phase is achieved by adjusting the cavity dichroics to align the phase planes collected by both objectives parallel to each other.

Finally, by employing the polarization, a single cavity with two outputs generates four channels. In contrast to a two cavity system (49), the present one facilitates alignment and enhances the stability, besides only standard optical components are required.

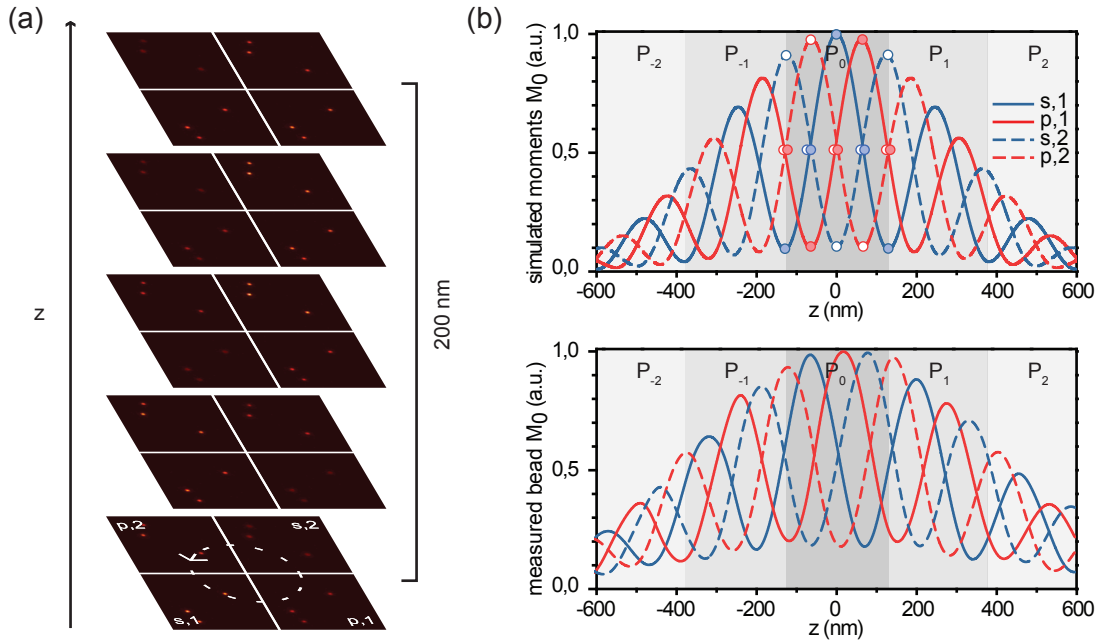


Figure 4.4 (a) Camera images for different axial planes of fluorescent beads scanned along z . The four channels are indicated by the quadrants. Each channel displays the same bead distribution, albeit mirrored. Note the modulation along z . The oscillation of the intensity between the channels with increasing z is indicated by the dashed white arrow. (b) Gaussian-weighted signal of the detection channels as a function of the axial marker position. Upper panel depicts simulated data, while the lower panel shows measured data. The relative intensities are used to calculate the global phase φ_0 which is unique within a range of $\lambda/2$ only. The periodicity of φ_0 is indicated by the gray bars which denote the different periods.

4.3 Signal Generation

Fluorescent beads were scanned over a z -range of about $1.2 \mu\text{m}$ around the focal plane in 40 nm steps. Fig. 4.4a shows camera images of different z -planes. The four channels are indicated by the different quadrants. Each channel reveals the same bead distribution albeit mirrored. Note the intensity modulation in the channels when scanning the beads along z , caused by the photon self-interference in the 4Pi cavity.

The lateral position of a bead image within each channel can be determined by using one of the established localization algorithms (cf. section 3.1.2). Subsequently the Gaussian weighted intensities in each channels, also called zeroth order moments $M_{0\kappa,1/2}$ ($\kappa = s, p$ -polarization), can be computed for each localization. Thus one event (bead image) is represented by four corresponding positions and intensities. To unify the information available in the four channels, three affine transformation which register channel 2-4 with channel 1 are identified. The final lateral position is then calculated as the intensity weighted average of the positions determined in each channel. The intensities, which depend on the phase and thus on the z -position, are saved separately. The exact implementation will be discussed in more detail in section 5.3.

The upper panel in Fig. 4.4b shows the calculated Gaussian-weighted fluorescence intensity

as a function of the z -position of a simulated point source for each of the four detection channels. The four signals oscillate as the point source is moved along the z -direction; note that the relative phases of the oscillations in each individual channel are evenly spaced within the 0 to 2π interval. As described later on in more detail, the relative intensities of the four channels can be used to calculate a global phase φ_0 , which specifies the average phase difference of the electric field of the emitted fluorescence, collected by both objectives and superimposed at the beamsplitter. φ_0 ranges from $-\pi$ to π and can be used to accurately determine the axial position of a fluorophore within an axial interval $\Delta z_0 \approx \lambda/2$, e. g. 255 nm. However, the fluorophores located outside this $\lambda/2$ sheet around the focal plane will be incorrectly projected into this sheet, leaving imaging artifacts. The lower panel in Fig. 4.4b reveals the Gaussian-weighted fluorescence intensity for a measured bead (hundredfold interpolated by a cubic spline). The overall behavior is quite similar to the simulated data. The disparities of the envelope are due to aberrations in the experimental system. The lower modulation depth of the measured data is most probably caused by a slight remaining dispersion in the cavity. In the next chapter a detailed description will be given on how to extract the z position of a marker from these data.

Chapter 5

Theory - Optimizing the Information Content

This chapter will show how the theoretical resolution limits of a 4Pi-SMS setup can be approached by exploiting the high numerical aperture of the objective lenses. First the equations describing the signal in the four channels will be derived. Afterwards it will be shown how to lift the periodicity in the acquired signal, which restricts the z determination to a range of $\Delta z_0 \approx \lambda/2$, e. g. 255 nm. Exploiting this additional information, a z -estimator allowing a high precision estimation of z over a theoretically unlimited z range will be developed. Finally the practical implementation of this estimator will be presented.

5.1 Coherent Detection

The field $\mathbf{A}(r, \phi, \theta_p, \phi_p, z)$ created by a dipole located on the optic axis at $(0, 0, z)$ and oriented along $\mathbf{p} = (\sin \theta_p \cos \phi_p, \sin \theta_p \sin \phi_p, \cos \theta_p)$ at position $\mathbf{r} = (r \cos \phi, r \sin \phi)$ in the exit pupil of the lens after passing the compensators was introduced in the last chapter. Here, $0 \leq r \leq \sin \alpha$ and α is the semi-aperture angle of the lens. As mentioned in section 4.2.1, the fields of the s - and p -polarization before the beamsplitter are related by

$$A_s(\phi_p + \phi, \phi_p) = i e^{-2i\phi_p} A_p(\phi_p - \phi, \phi_p). \quad (5.1)$$

If the two arms denoted by a and b are identical and if a constant phase for the p -polarization is ignored, the components of \mathbf{A} are given by

$$A_{\kappa a/b}(r, \phi, \theta_p, \phi_p, z) = A(r, \phi, \theta_p, \phi_p) \exp\left(\pm i k z \sqrt{1 - r^2}\right) \quad (5.2)$$

where $\kappa = s, p$ denotes the polarization component. The additional square root factor in the exponential function describing the wave nature of light, approximates the curvature of the wavefront in the back aperture of the objective for emitters out of focus ($z \neq 0$).

In the absence of aberrations, A is a real function of the dipole angles and the position in the back-aperture. For large focal lengths of the last lens in the imaging system, the z -component of the electric field in the image plane can be neglected and the fields generated through the lenses a and b , $E_{\kappa a/b}$, are linearly polarized along κ and given by the Fourier transform of $A_{\kappa a/b}$. Taking into account the phase delay of $\varphi_{\kappa a/b}$ in the two arms and the reflection at the beamsplitter, the

electric fields in the images of beam-paths 1 and 2 are given by

$$\begin{aligned} E_{\kappa 1} &= [E_{\kappa a} \exp(i\pi/2) \exp(i\varphi_{\kappa a}) + E_{\kappa b} \exp(i\varphi_{\kappa b})] / \sqrt{2} \\ E_{\kappa 2} &= [E_{\kappa a} \exp(i\varphi_{\kappa a}) + E_{\kappa b} \exp(i\varphi_{\kappa b}) \exp(i\pi/2)] / \sqrt{2}. \end{aligned} \quad (5.3)$$

The dipole orientation has no influence on the phase differences defined later on and employed to determine z . The influence of shape of the PSF on the orientation of the dipole is averaged out since the here explored markers rotate much faster than the acquisition time of the camera, which is around 10 ms. Therefore, in the following, the dependence of the fields on the dipole orientation is neglected. However, for completely static dipoles, a minor influence on the analysis described below can not be excluded and a careful quantification of this effect should be the subject of further studies. As already mentioned, the effect is not limited to the axial position estimation, it also has to be assessed for 2-dimensional SMS experiments.

Because the imaging system is aplanatic, the lateral dependence of above fields only depends on the axial position of the emitter and its lateral position (x, y) relative to the point of detection. As mentioned in section 4.2.2, the phase differences $\Delta\varphi_{\kappa}$ between both arms for each polarization can be adjusted independent of beam-path and polarization using the mirrors of the cavity or the beamsplitter and the compensator in arm a . The setup is adjusted such that the phase of $E_{\kappa a/b}(x, y, 0)$ is equal for all (x, y) and over the whole emission spectrum. Note that due to equation (5.2), the fields ideally obey $E_{\kappa a}(x, y, z) = E_{\kappa b}(x, y, -z)$. However, this symmetry may be broken in the presence of aberrations induced for example by the sample, uncompensated variations in the cover glass thickness when imaging with water immersion lenses or simply by a refractive index mismatch between the immersion medium and the sample. For the success of the z -estimation this symmetry is not mandatory because a gauge procedure is used to compensate for deviations. Extracting the $\Delta\varphi_{\kappa}$ -dependence, the intensities in the four channels can be reduced to the following formula

$$I_{\kappa 1/2} = |E_{\kappa a}|^2/2 + |E_{\kappa b}|^2/2 \pm 2|E_{\kappa a}^* E_{\kappa b}| \cos[\varphi_{\kappa}(z) - \Delta\varphi_{\kappa}] \quad (5.4)$$

where the z -dependent phase is given by

$$\begin{aligned} \cos[\varphi_{\kappa}] &= -\Im[E_{\kappa a}^* E_{\kappa b}] / (|E_{\kappa a}| |E_{\kappa b}|) \\ \sin[\varphi_{\kappa}] &= -\Re[E_{\kappa a}^* E_{\kappa b}] / (|E_{\kappa a}| |E_{\kappa b}|) \end{aligned} \quad (5.5)$$

The fields and the phases depend on (x, y, z) and their z -dependence is used to estimate the axial position of the emitter. However, the phases φ_{κ} are only unambiguous on an range of about $\lambda/2 \approx 255$ nm. Therefore, further information is required to enable z determination on larger z -ranges.

5.2 Moment-based Estimator

From a statistical point of view, the integrated intensity of a PSF in the imaging corresponds to the zeroth order moment of the photon distribution. A general probability distribution $p(x)$ of a

random variable X is given by all its moments \tilde{M}_l providing they exist (appendix B),

$$p(x) = \int \frac{dk}{2\pi} e^{ikx} \sum_l \frac{(-ik)^l}{l!} \tilde{M}_l \quad (5.6)$$

Motivated by this, a moment based estimator will be introduced next. Note that all subsequent moments are additionally weighted by a Gaussian to reduce the influence of the background and are thus not completely identical with the moments from above.

5.2.1 Analytical Phase Plane Depiction

The setup resembles of course that of a simple interferometric position monitor. Indeed, if lenses of very low numerical aperture are used, the square root in equation (5.2) can be set to unity and the equation is reduced to,

$$[E_{\kappa a}^* E_{\kappa b}](x, y, z) = [E_{\kappa a}^* E_{\kappa b}](x, y, 0) \exp(-i2kz) \quad (5.7)$$

and thus only the phase is z -dependent in equations (5.5) with

$$\varphi_{\kappa}(x, y, z) = 2kz \quad (5.8)$$

It is immediately obvious that this will only allow an unambiguous estimation in a layer of thickness $\lambda/2$ due to the periodic nature of the intensity variations. All approaches which do not take the high numerical aperture into account are at best similarly limited and deliver false estimates in the worst case.

In order to extract unambiguous z -estimates, the fact that the objective lenses have high focusing angles has to be exploited. In this case the z -dependent oscillation of the intensity in the back-aperture will depend on the distance from the optic axis and the same will be true in the Fourier transform, i.e. in the image of the emitter on the camera. While the exact dependence is not readily derived in closed form, it can be inferred from equation (5.2) that the central part of A and thus the outer rings of E oscillate faster. In order to use this fact the weighted moment operator \mathbf{M}_l acting on an intensity distribution $I(\mathbf{r})$ is defined by,

$$\mathbf{M}_l[I](z) = \int dx dy w_l(R) I(x, y, z). \quad (5.9)$$

with $R = \sqrt{x^2 + y^2}$ and the weighting functions of the moments,

$$w_l(R) = \exp[-R^2/2\sigma^2] R^l. \quad (5.10)$$

The moments,

$$M_{l\kappa,1/2} = \mathbf{M}_l[I_{\kappa,1/2}] \quad (5.11)$$

of an emitter's intensity distribution are going to be used as parameters for the determination of its z -position. Note that the particular choice of weighted moments here has proven to be successful but may not be the optimum choice for all applications. Certainly alternative weighting functions can be used in equation (5.9) to derive valid estimators. Most likely cylindrical symmetry of new functions should be maintained as it ensures a certain robustness against tilt and rotation of the

emitters. For instance, one could imagine ring-like weights with different diameters exploiting the very same features of the detection PSFs as the approach presented here. A more detailed analysis would be a worthwhile subject for further studies.

Applying the moment operator \mathbf{M}_l on the intensities defined in equation (5.4), the moments can be written as follows,

$$M_{l\kappa 1/2}(z) = \mathbf{M}_l[|E_{\kappa a}|^2 + |E_{\kappa b}|^2]/2 \pm |\mathbf{M}_l[E_{\kappa a}^* E_{\kappa b}]| \cos[\varphi_{l\kappa} - \Delta\varphi_\kappa]. \quad (5.12)$$

where $\varphi_{l\kappa}$ is determined analogous to φ_κ . While all quantities now vary with z , the envelope and the modulation strength vary due to the aberrations introduced by the square-root factor in equation (5.2) and thus change quite slowly while the phase function exhibits a much stronger dependence on z with a period of approximately half a wavelength. Importantly, the period of the phase functions depends on l which allows to resolve the ambiguity occurring in layers thicker than $\lambda/2$. This is in agreement with former theoretical studies (49) which show that the PSF contains enough information to uniquely identify positions within a much thicker layer.

z -estimation will be based on a gauge measurement and the amplitudes in eq. (5.12) may slightly vary between gauge measurement and sample due to spectral changes effecting a change in relative transmission in the s and p polarized channels and due to aberrations and the averaging over a larger or smaller emission spectrum affecting the modulation depth. The robustness can thus be increased by using relative values

$$m_{l\kappa}(z) = [M_{l\kappa 1}(z) - M_{l\kappa 2}(z)]/M_{l\kappa}(z) = b_{l\kappa}(z) \cos[\varphi_{l\kappa}(z) - \Delta\varphi_\kappa] \quad (5.13)$$

where the total moment for each polarization direction is defined as

$$M_{l\kappa}(z) = M_{l\kappa 1}(z) + M_{l\kappa 2}(z) \quad (5.14)$$

and the relative modulation strength, $b_{l\kappa}(z)$, is implicitly defined. Note that the $m_{l\kappa}$ remain unchanged if the detection efficiency of s versus p -polarized light varies. In experiments, $\Delta\varphi_s - \Delta\varphi_p$ is tuned to $\pi/2$ to maximize the information content (49), while the absolute phase $\Delta\varphi = \Delta\varphi_s$ is often unknown and may drift between experiments. The z -information is predominantly contained in the phase $\varphi_{l\kappa}$ which is independent of the polarization and varies fast with z . It is therefore advantageous to further decrease the amount of parameters by defining

$$\begin{aligned} c_l(z) &= m_{ls}(z)/\rho_l(z) = \cos[\varphi_l(z) - \Delta\varphi] \\ s_l(z) &= m_{lp}(z)/\rho_l(z) = \sin[\varphi_l(z) - \Delta\varphi] \end{aligned} \quad (5.15)$$

where

$$\rho_l(z) = [m_{ls}(z)^2 + m_{lp}(z)^2]^{1/2}. \quad (5.16)$$

The quantities $c_l(z)$ and $s_l(z)$ will be used for z -estimation (see below) and are called *reduced moments* in the rest of this thesis. Note that the dependence of $\varphi_l(z)$ on z deviates slightly from a linear relationship even in an ideal setup. Importantly, as long as these deviations are the same for both gauge and real measurement, they will merely lead to a slightly changing localization accuracy over the z -range.

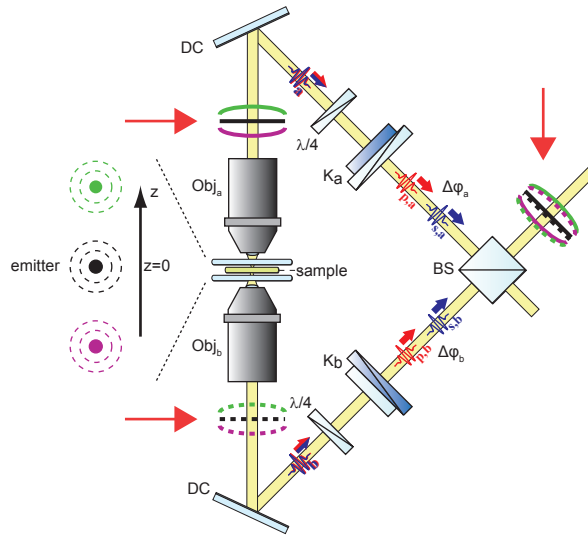


Figure 5.1 Bent phase planes. Three emitters at different z planes: emitter in the focal plane ($z = 0$, black), above the focal plane ($z > 0$, green) and below the focal plane ($z < 0$, purple). Depending on the z position of the marker, the spherical emitted wavefronts (see red arrows) are bent with different strength and curvature in the back aperture of the objectives. The wavefronts in both arms are superimposed at the beamsplitter (BS).

5.2.2 Bent Wavefronts

The impact of the high numerical aperture objectives shall be discussed also qualitatively by means of Fig. 5.1. The figure shows the cavity of the 4Pi-SMS setup. Three different marker positions are indicated by the emitters and their emitted spherical waves on the left hand side. The black colored emitter is in the focal plane $z = 0$ of both the objectives, while the green and purple labeled markers are above and below the focal plane respectively. The spherical waves emitted by a marker in the focal plane are collimated by both objectives and thus result in plane waves in the back aperture. The spherical waves of an emitter above the focal plane ($z > 0$) result in negative and positive bent wavefronts behind the objectives a and b respectively. This is explained by the different distances to the foci of the objectives. The wavefronts of an emitter below the focal plane ($z < 0$) are also bent in the back aperture of the objectives but with inverted curvatures. At the beamsplitter the wavefronts of both objectives are united. Without loss of generality, the phase difference $\Delta\varphi$ between both arms is assumed to be zero. The following implications hold for both polarizations. In the case of an emitter in the focal plane (black) both wavefronts are parallel and arrive at the same time. If the emitter is above the focal plane (green), the negatively bent phase plane of objective a, arrives before the positively bent phase plane of objective b. In the case of an emitter below the focal plane the arrival times and curvatures are interchanged. Note that the bending of wavefronts causes distinct phase differences in its central and outer area. This difference is employed to break the periodicity present for an estimator which is only based on the zeroth moment.

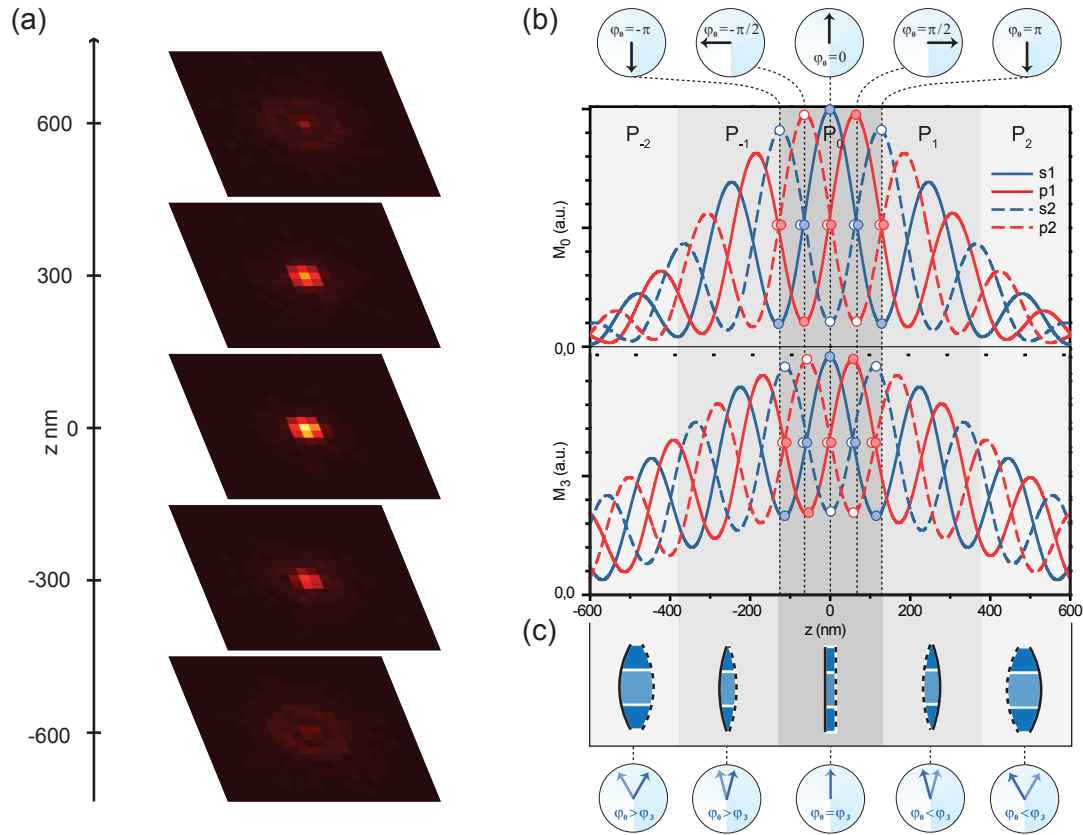


Figure 5.2 Evaluating moments. (a) Image in channel $s1$ of a fluorescent bead at different z -planes ranging over about $1.2 \mu\text{m}$. Note that the shape of the bead changes for different z positions. (b) Gaussian-weighted signals $M_{0\kappa,1/2}$ and Gaussian-weighted third central moments $M_{3\kappa,1/2}$ of the detection channels as a function of the axial marker position. Note that the periodicity of both moments is distinct. The relative intensities are used to calculate the global phases φ_0 and φ_3 . While each of them is unique within a range of $\lambda/2$ only, the phase pair $[\varphi_0, \varphi_3]$ uniquely encodes the axial position over a much larger range. (c) The propagation of fluorescence light from out of focal plane emitters is described by a segment of a spherical wavefront, implying that the phase as a function of the z -position varies more slowly for the outer wavefront parts.

5.2.3 Reduced Moments

The problem of the periodicity in the signal is solved by exploiting the fact that the phase difference between the counter propagating wavefronts after the objective lenses varies more slowly at the outer parts when the emitter moves out of focus. To this end, the global phase not only for the Gaussian-weighted intensity of the fluorescence spot on the camera is calculated, but also for its Gaussian-weighted 3^{rd} central moment, which has a larger contribution from the inner parts of the wavefront. The resulting phase pair $[\varphi_0, \varphi_3]$ uniquely encodes the axial position of the marker over a range much larger range than $\lambda/2$. Fig. 5.2a shows the image in the first channel of a fluorescent bead for different z planes. The shape of the image depends on the z position. Fig. 5.2b reveals the

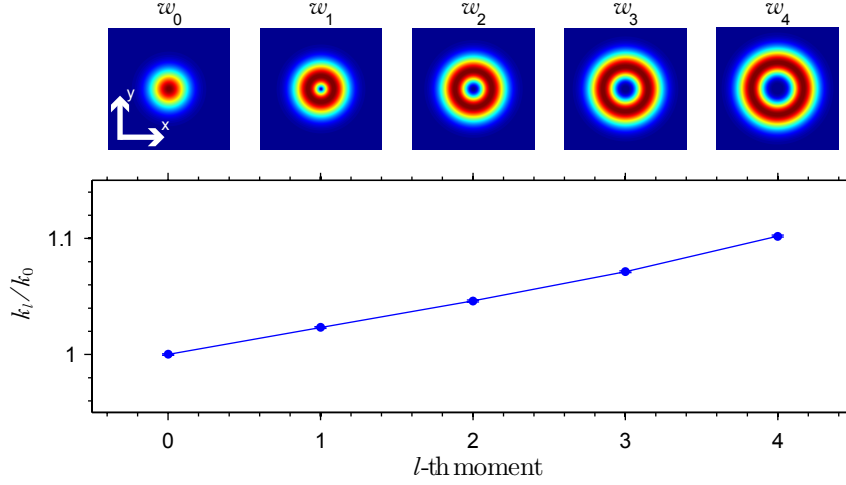


Figure 5.3 The modulation speed of the moments M_l increases with their order. (a) Illustration of the weighting functions w_l used for the calculation of the moments M_l . (b) Spatial modulation frequency k_l along the optic axis of the different moments $M_l(z)$ extracted from measuring a bead scanned along z . k_l was determined by fitting the reduced moments defined in equation (5.15) with $b \cos(k_l z - \varphi_0)$. The modulation is faster for higher moment orders l which emphasize the outer parts of the emitter's image. From a single phase $k_l z$, the z -position can not be unambiguously inferred as a shift by $2\pi/k_l$ reproduces the same value. However, by measuring at least two phases, this ambiguity is lifted allowing localization over a much larger range of z -values.

calculated zeroth and third moments for such a z -scan. Note that the modulation frequency of the third moment is slightly larger than the modulation frequency of the zeroth moment. The upper ‘phase watch’ panel indicates the phase of channel s1 for different z positions within the period P_0 , which corresponds to a z -range $\Delta z_0 \sim \lambda/2$. This phase course is same in all other periods P_i , indicated by the different gray bars, and therefore φ_0 alone is not capable of differentiating between the distinct periods. Fig. 5.2c sketches the wavefronts of both objectives at the beamsplitter. Note how the shape depends on the z position of the emitter. The phase differences of the central area are larger than the phase differences of the outer area, implying a faster modulation of the central part of the wavefront. Since the outer areas contribute more to the center of the PSF when the wavefront is focused, they contribute more to the zeroth moment which renders the central part of the PSF. In contrast, inner areas of the wavefront contribute more to the outer regions of the PSF and thus to the higher order moments. This is in agreement with a faster modulation of the 3rd order moment. The ‘phase watch’ panel in Fig. 5.2c sketches the phases φ_0 and φ_3 for different periods. Note the distinct phase combinations for each period which breaks the periodicity, and how φ_3 runs faster than φ_0 with variable z . In a properly aligned microscope, the focal plane ($z = 0$) is identified by $\varphi_0 = \varphi_3$.

The increasing modulation speed of the higher order moments can be seen in Fig. 5.3. The upper panels reveal the moment masks, i. e. the weighting functions $w_l(R)$ of the moments defined in eq. (5.10). Lower order moments accentuate the center of the PSF while higher order moments render the outer parts. The lower panel shows the modulation frequency k_l of the moments as function of their order l . A monotonic increase of the frequency with the order of the moment is

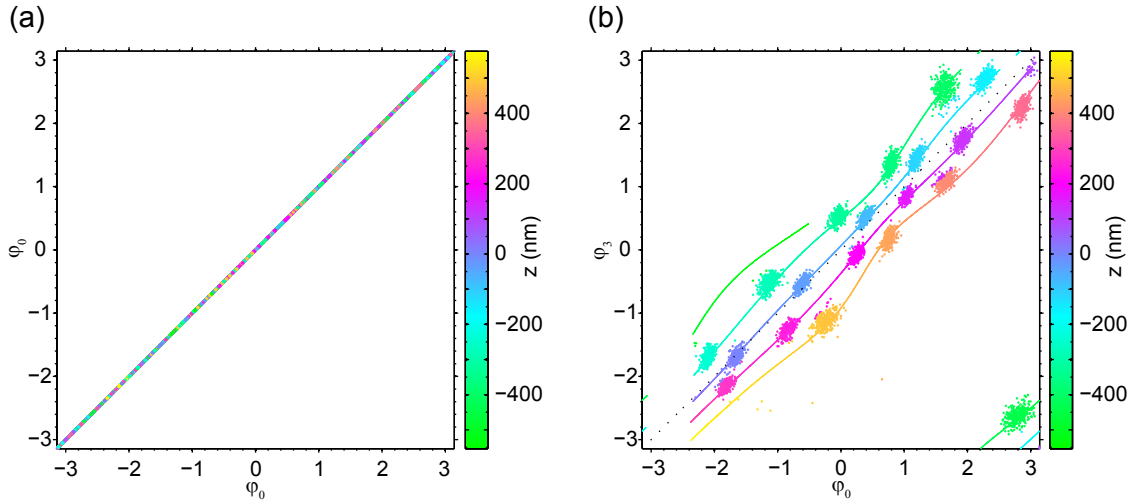


Figure 5.4 Phase pairs $[\varphi_0, \varphi_0]$ (a) and $[\varphi_0, \varphi_3]$ (b) for z-scans of a bead. A scan with high photon yield (line) and a scan with low photon yield and 300 independent measurements at each axial location (dots) are shown. The first scan corresponds to a gauge measurement, while the second one yields a statistical sample. In (a) events with a distance Δz_0 have the same φ_0 , implying that colors corresponding to different z planes have the same position in $[\varphi_0, \varphi_0]$ -space (a random subset is shown). Therefore, no bijective function connecting φ_0 and z can be found for z intervals larger than Δz_0 . The problem is solved by employing the phase of an additional moment, e. g. φ_3 . In $[\varphi_0, \varphi_3]$ -space (b) each shown z position is unambiguously defined. The axial marker position is estimated by determining the point on the gauge curve that minimizes the distance $D(z)$ defined in section 5.3. Note that in a properly aligned setup, the focal plane ($z = 0$) is unambiguously defined by $\varphi_0 = \varphi_3$.

clearly visible. Note that although e. g. k_4 is larger than k_3 in this work the third order moment was employed, since the noise of the signal also increases with the order of the moments. The third order moment turned out to be a good compromise between high spatial frequency difference and low noise.

To demonstrate the ability to discern different periods, a fluorescent bead was scanned over a range of $2 \mu\text{m}$ around the focal plane in 40 nm steps and recorded at a camera-exposure time of 100 ms , yielding a gauge measurement. Afterwards the bead was again scanned over the central $1 \mu\text{m}$ in 40 nm steps and 300 images per z -step were recorded at an exposure time of about 10 ms yielding a statistical sample with less photon counts. A more detailed description of the applied parameters will be given in the next chapter, where the setup is going to be characterized. Fig. 5.4a shows the recorded data in a two-dimensional space spanned by $[\varphi_0, \varphi_0]$. The color encodes the z position of the bead. Since a differentiation of the distinct periods is not possible, the same phase values encode different z planes. The situation completely changes when involving φ_3 . Fig. 5.4b shows the same measurement in a $[\varphi_0, \varphi_3]$ space. The different z positions of the hundredfold interpolated gauge measurement (line) as well as the statistical sample (dots) can be identified unambiguously. Each z position has a unique combination of $[\varphi_0, \varphi_3]$ and can thus be uniquely identified over the whole z -range of at least $1 \mu\text{m}$. The spread of the statistical sample around the gauge measurement is due to the lower photon yield which introduces more uncertainty in the

calculated parameters.

Thus a z determination of a marker's position can be performed by identifying the closest point of a z gauge measurement in $[\varphi_0, \varphi_3]$ space and assigning the corresponding z value.

5.3 Extracting z

5.3.1 Implementation of the Estimator

The estimation of the axial position is implemented in a collection of MATLAB routines as follows: The acquired frames are corrected for background by a Gaussian filter and the positions of events are estimated independently in each channel as described in former studies (33). In short: relevant image segments are identified by applying a count threshold to the frame. The quadratic segment is then multiplied with an initially centered normalized Gaussian of equal FWHM as the PSF. In each iteration the center of mass of the product of the Gaussian with the background-corrected image is calculated and used as the center for the Gaussian in the next iteration. An event is listed if this iteration converges, i.e. if in less than 100 iterations the displacement of two consecutive iterations becomes less than 10^{-5} of the pixel size, otherwise the event is discarded. Prior to the actual measurements, the three affine transformations that register channel 2-4 with channel 1 are determined. This is done by recording a fluorescent bead distribution, applying the localization algorithm, cutting out four quadrants of each camera frame and determining the affine transformations that best co-localize the identified positions. To this end three starting transformations are applied to channels 2-4 which have to be fair estimates of the actual transformations. For each bead (event in channel 1) the three positions (in channels 2-4) that correspond to it are then identified by finding the events which lie closest to it after back-transformation. Assuming that the assignment is correct for a majority of beads, the correct transformations are then found by minimizing the mean square distance and iterating the whole process if necessary (bad initial guesses and/or dense bead distributions). Note that the transformations may be calculated from the actual data itself but using beads to obtain master transformations turned out to be more reliable and accurate due to the better SNR of the images. The remaining uncertainty σ_{tr} in the xy -positions due to the transformation process was less than 5 nm. The relative movement of the four channels between calibration measurements due to experimental drifts was controlled and turned out to be negligible.

When analyzing the data, quadruples of events in the four channels are identified as above, the center of the event is calculated as the weighted mean of the centers in the four channels. Using the common center, the weighted moments from equation (5.9) are calculated and recorded for each channel. The data is corrected for the detection efficiency of the individual channels and the z -dependent reduced moments c_{lk} and s_{lk} defined by equation (5.15) and the phases φ_{lk} , for $l = 0, 3$ are computed for each event k .

The estimator is based on a reverse-lookup from a calibration curve acquired by scanning fluorescent beads along z (over $1.2 \mu\text{m}$ around the focal plane with steps of 40nm) and interpolating the recorded moments along z (resulting in a calibration curve $c_{lG}(z)$, $s_{lG}(z)$ with steps of 0.4nm). As mentioned above, the absolute phase common to all moments defined in equation (5.15) can differ between gauge curve and experiments. When using only one moment, e.g. $l = 0$, the global phase $\Delta\varphi$ would have to be known to extract z from c_l and s_l and the z -position would be ambiguous due to the periodicity of φ_l . However, when using $l = 0, 3$, plotting all values of φ_0 against φ_3 reveals a characteristic pattern (cf. Fig. 5.4b) that is shifted along the bisecting

line when $\Delta\varphi$ changes. Given a gauge curve $\bar{\varphi}_{0/3}(z)$ and a measurement consisting of N localizations $\{\varphi_{0/3,k}; k = 1 \dots N\}$, the relative global phase $\Delta\bar{\varphi}$ between gauge measurement and experiment is extracted as follows: Smoothed 2d-histograms in $[\varphi_0, \varphi_3]$ -space are computed for the gauge measurement and the sample, resulting in $\bar{\mathbf{C}} = [\bar{C}_{i,j}]_{n \times n}$ and $\mathbf{C} = [C_{i,j}]_{n \times n}$, respectively. The histogram of the gauge measurement can be calculated for different absolute phases $\Delta\tilde{\varphi}_m$. Exploring the following quantity as function of $\Delta\tilde{\varphi}_m$,

$$g(\Delta\tilde{\varphi}_m) := \sum_{i,j} C_{i,j} \bar{C}_{i,j}(\Delta\tilde{\varphi}_m) \quad (5.17)$$

allows to determine the relative global phase $\Delta\bar{\varphi}$ as,

$$\Delta\bar{\varphi} = \arg \max_{\Delta\tilde{\varphi}_m} g(\Delta\tilde{\varphi}_m). \quad (5.18)$$

The phases $\varphi_{0,G}$ and $\varphi_{3,G}$ of the gauge curve are corrected by applying the common phase shift $\Delta\bar{\varphi}$. With this corrected gauge measurement, the z -estimate is then obtained by minimizing the distance of an event k to the z -gauge curve:

$$D_k^2(z) = \sum_{l=0,3} w_l^2 \{ (c_{lG}(z) - c_{lk})^2 + (s_{lG}(z) - s_{lk})^2 \}, \quad (5.19)$$

The weights w_j are chosen according to the experimental uncertainty of the two phase parameters, in the present setup w_0 and w_3 are 1 and 0.35 respectively.

Potential common drifts (of all 4 channels together) in space are corrected by cross-correlating packages of 10000 frames.

If the setup is correctly aligned, the axial position $z = 0$ is defined by the z plane in which $\varphi_0 = \varphi_3$ for all wavelengths but the PSF still scales with the wavelength. Because the mean wavelength of the dye, λ , will usually differ from the mean wavelength of the gauge measurement, λ_G , z -positions have to be corrected by scaling the phase-focus-centered z values with the ratio of the mean wavelengths λ/λ_G .

5.3.2 Color Coding

To visualize the data a color coding of the z information is used. To this end the mean z value for each pixel of the xy -histograms is calculated and a color based on a z -color map is assigned. The color map is created by identifying four z positions with specific colors and by linearly interpolating between them. The z positions of the specific colors are defined by the 0/0.33/0.66/1-quantiles of the cumulative z distribution to maximize the dynamical contrast. The color intensity reflects the event counts in a bin. For visibility purpose some pixels of the 2D-histograms are saturated.

Chapter 6

Characterizing the Nanoscope

In the following, the resolution and stability of the setup is going to be characterized by means of fluorescent beads, which describe a standard model system to determine properties of a microscope.

6.1 Fluorescent Beads

The fluorescent beads (FluoSpheres carboxylate-modified microspheres, 100 nm specified diameter, red fluorescent 580/605, Invitrogen) were diluted in distilled water by 1:5000, afterwards the bead solution was placed on a cover slip treated with Poly-L-lysine (Sigma-Aldrich, Saint Louis, MO, USA) solution, 0.1 % (w/v) in H₂O. The solution was incubated for 10 min. To remove unattached beads the sample was rinsed with water. After adding 10 μ l distilled water as medium, the sample was covered by a second cover slip and sealed with nail polish. A gauge measurement was recorded by scanning a bead over a range of 2 μ m in 40 nm steps at a camera-exposure time of 100 ms. A 532 nm solid state laser (DPSS 532, HB-Laserkomponenten, Schwäbisch Gmünd, Germany) was used as excitation source. In order to characterize the setup, the bead was scanned over the central 1 μ m range in 40 nm steps and 300 images per z-step were recorded. Here the exposure time was 10 ms at an excitation intensity of about 1 kW/cm² yielding about 2700 photons per frame and detected bead. To explore the localization precision in the focal plane as a function of the detected photon number, 300 independent measurements were performed for different emitter brightnesses.

6.2 Resolution potential of 4Pi-SMS

The axial position of the z scanned beads is determined by the estimator introduced in section 5.3. In Fig. 6.1a the determined z position is plotted against the real z position defined by the piezo stage. As can be seen, the axial bead position can be determined over the whole z-range unambiguously. A calculated confocal PSF is sketched for comparison. The insets of Fig. 6.1a show histograms of the axial localizations for two selected positions of the scan. The distributions can be fitted well with Gaussians of standard deviations (sigma) equaling 2.6 nm and 2.8 nm for z = -181 nm and 180 nm, respectively. By fitting a Gaussian to the main peak of the position histogram for each location, the overall axial localization accuracy can be estimated to $\sigma_z \sim 2.3 - 3.5$ nm (5.4-8.2 nm FWHM) as shown in Fig. 6.1b. The lateral resolutions are shown in Fig. 6.1d and are in the range of $\sigma_{xy} \sim 3.5 - 17.5$ nm depending on the axial position. Fig. 6.1c depicts the data in a space spanned by the phases φ_0 and φ_3 introduced in chapter 5, z is encoded by the color. The interpolated gauge measurement is shown as line, while the dots correspond to the 300 measurements per axial position. As discussed in section 5, an additional phase (e. g. φ_3) allows

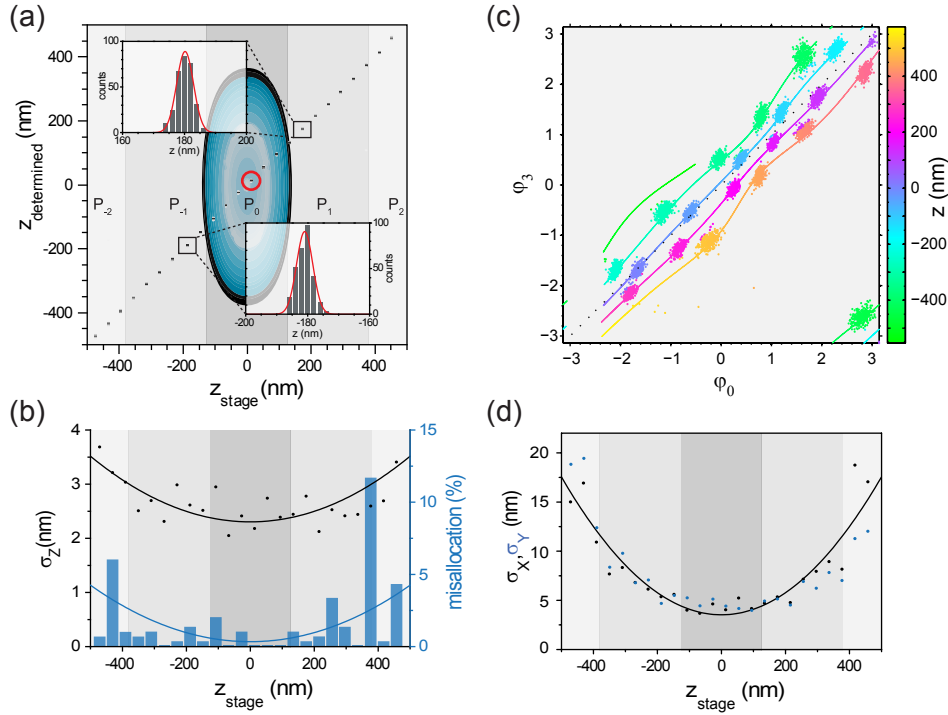


Figure 6.1 (a) The phase pair $[\varphi_0, \varphi_3]$ encodes the axial marker position at least over a range of $1 \mu\text{m}$. A confocal PSF is sketched for comparison. (b) The axial localization accuracy (black dots) for a fluorescent bead containing randomly oriented emitters is about 2.3-3.5 nm over the whole range. The amount of misallocation (blue bars) is well below 4.5%. (c) Data in $[\varphi_0, \varphi_3]$ space. The determined z position is encoded by the color. Note how the different z positions can be distinguished over the whole z range of about $1 \mu\text{m}$. (d) The lateral localization accuracy (black dots x-direction and blue dots y-direction) ranges from 3.5-17.5 nm.

to differentiate between positions further away than $\Delta z_0 \cong \lambda/2$, here 255 nm.

The resolution is already in a regime where the localization precision is of the order of the residual setup instabilities, as will be seen later on. It should be noted that the bead is a bright, nearly isotropic emitter because it contains many randomly oriented fluorophores. The practical localization accuracy of single emitters and ultimately the resolution will be limited by the typically lower photon budget, and in the case of largely static molecules, by localization errors due to emission anisotropies occurring when the emission dipole is tilted with respect to the z -axis and the focal plane. It should be also noted that other limiting factors, like the linker length between the target epitope and the fluorescent marker, can easily abate the achievable resolution for biological imaging. However, since a specific labeling technique, like e. g. antibody labeling as used here, is not mandatory for the presented nanoscope, also smaller makers, e. g. fluorescent proteins, can be employed to exploit the full capability of 4Pi-SMS.

At the border of the axial imaging range, a slightly increased probability of incorrect assignment of the bead position to planes located at a distance $\Delta z_0 \cong \lambda/2$, e.g. 255 nm, above or below the actual plane is observed. This is due to the spreading of the diffraction spot for emitters further

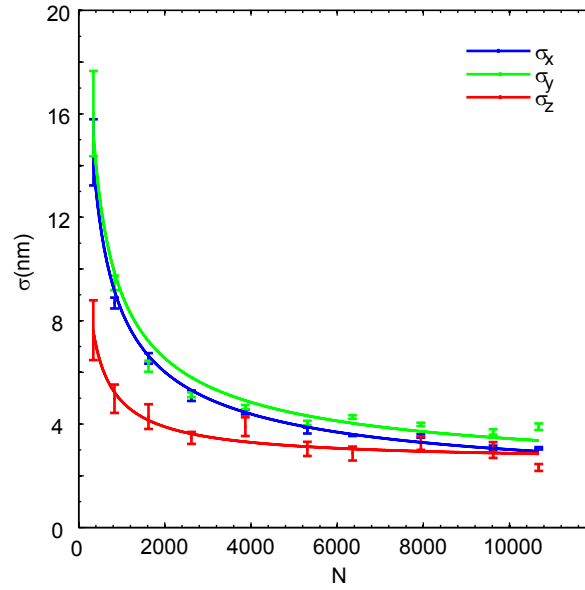


Figure 6.2 Localization accuracy of an emitter in the focal plane as a function of its brightness. The determined standard deviation σ_x , σ_y and σ_z of the lateral and axial coordinates are shown as function of the average detected photon number N . The data is well described by $\sigma = [2\sigma_0^2/N + \sigma_{\text{vib}}^2]^{1/2}$, where σ_0 is the error due to the localization process and σ_{vib} is a standard deviation related to residual instabilities of the setup. The parameters are summarized in table 6.1.

away from the focal plane and the concomitant increase of noise (see also Fig. 6.1c). However, this probability is on average well below 4.5 % over the whole z -range, and typically as low as 0.75 % for the most central axial range of 700 nm.

6.2.1 Photon Number Dependence

To obtain the photon number dependence of the resolution as well as to assess to what extent the localization accuracy is limited by setup instabilities, a fluorescent bead located in the focal plane was imaged at different excitation intensities.

300 independent measurements were performed for each emitter brightness. The average number of photons N detected per measurement was calculated and the standard deviations σ_x , σ_y and σ_z of the lateral and axial coordinates were determined. Fig. 6.2 reveals the localization accuracy in the focal plane as a function of the detected number of photons. The data is well described by,

$$\sigma(N) = \sqrt{\frac{2\sigma_0^2}{N} + \sigma_{\text{vib}}^2} \quad (6.1)$$

where σ_0 is the error due to the localization process and is correlated to the detection PSF and σ_{vib} is a standard deviation related to residual instabilities of the setup. The factor of 2 in the formula accounts for excess noise introduced by the electron amplification within the EMCCD. The determined parameters σ_{vib} and σ_0 for the x , y and z -directions are listed in table 6.1. By discriminating the error introduced by instabilities from the count-rate dependent localization accuracy, a coordi-

Table 6.1 Resolution parameters

	x (nm)	y (nm)	z (nm)
σ_{vib}	1.5	2.0	2.6
σ_0	184	197	93

nate instability of about 2 nm was found.

Estimates for the localization precision of the experiments presented in this work were obtained by scaling the results from these measurements according to the actual marker brightness.

Chapter 7

Biological Applications

7.1 Imaging the fibrinogen receptor distribution on activated human platelets

To explore the resolution of 4Pi-SMS microscopy in biological specimen and its ability to unambiguously image within samples thicker than $\lambda/2$, first the distribution of fibrinogen receptors on human platelets, which form clusters upon platelet activation was imaged (91). The glycoprotein (GP) IIb/IIIa receptor complex was visualized by staining GPIIb using the photochromic Rhodamine S (RhS) and the fluorescent dye Atto532. It was not necessary to confine the light field to a slice thinner than $\Delta z_0 \sim 255$ nm, because with the method introduced in chapter 5 the axial positions can be determined unambiguously also for larger ranges than Δz_0 .

The platelets are smooth, disc-shaped cells of approximately $3 \mu\text{m}$ diameter, having a typical thickness of about $1 \mu\text{m}$. Upon surface activation, they adhere and spread over a stellate shape into a 'fried egg' form (92).

7.1.1 Results

Fig. 7.1a shows an xy-histogram of the molecular positions recorded from a partially thrombin activated platelet labeled with RhS. 30000 images were acquired at a frame rate of 100 Hz with continuous wave excitation at 532 nm, and at an illumination intensity of 7-14 kW/cm². Irradiation with activating UV light was not required, because at pH=7 the RhS molecules switch back to their on-state thermally at a sufficient rate. The cell's stellate shape is clearly visible. The protuberances exhibit a round profile and taper at their ends. This is exemplified in Fig. 7.1b and d which show x'z-position histograms of the fluorophore positions within the indicated rectangles and further confirmed by the respective z-position histograms. In the upper left corner a wide-field image is overlaid (alpha value 0.7).

Fig. 7.1f shows an xy-histogram of a platelet exhibiting the 'fried egg' shape, labeled with Atto532 (120000 images recorded). Since Atto532 is an ordinary fluorophore, GSDIM was chosen as the stochastic imaging modality. Therefore, on-off-switching of Atto532 was performed by randomly shelving >90% of the molecules into a metastable dark state (34) by homogeneously illuminating the sample with 532 nm laser light at an intensity of 7-14 kW/cm². The same light is employed to excite the molecules remaining in the singlet ground state. The cell can be recognized as a whole, with the upper and the lower membrane forming an arch. The membranes converge before they diverge again, and the upper membrane reaches out to form a cupola. Individual clusters of receptors on the plasma membrane of the activated platelet are easily identified in the high resolution image, in contrast to the wide-field image indicated by the overlay in the lower left corner (alpha value 0.7). To further illustrate the shape of the membrane, a yz-position histogram of all

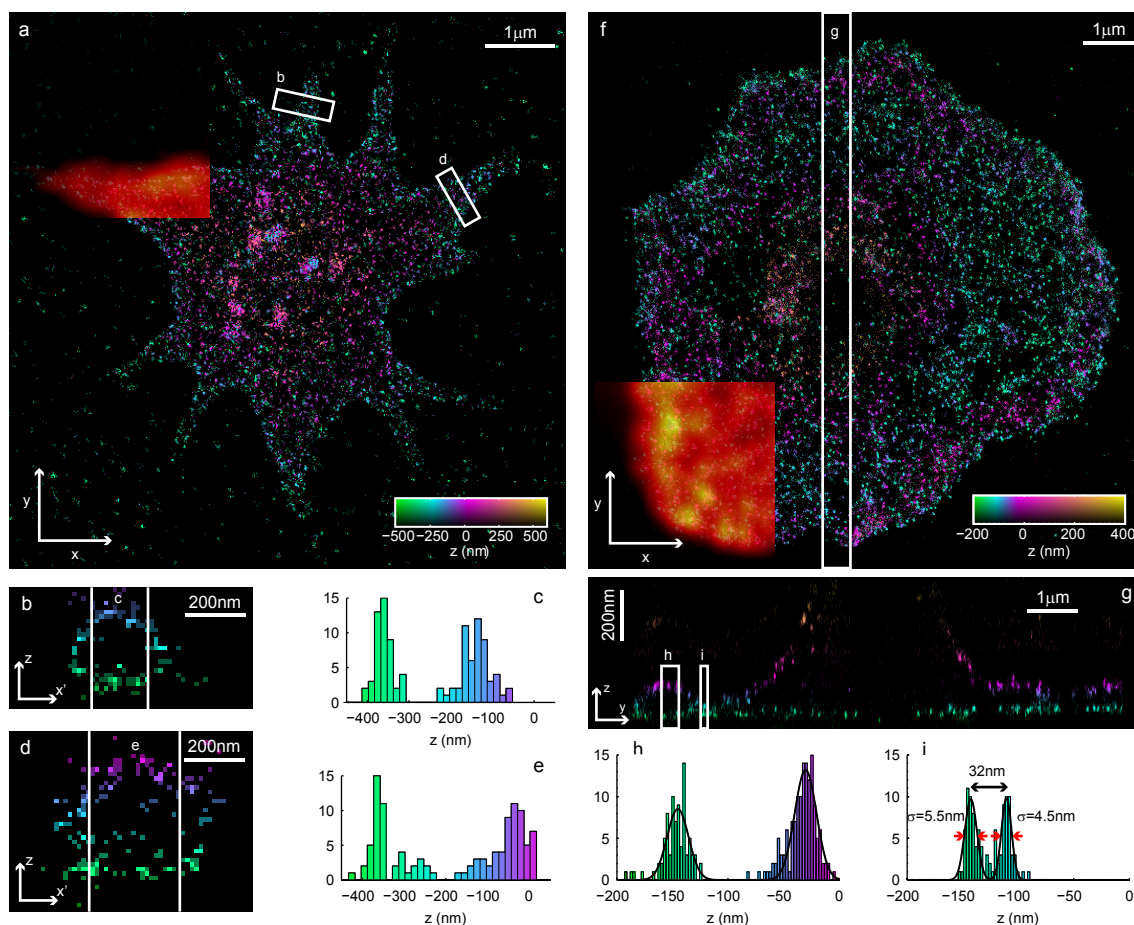


Figure 7.1 Activated human platelet imaging. (a) xy-image of the RhS labeled GpIIb/IIIa receptor protein of a partially thrombin-activated platelet. The color encodes the axial position of each label. The estimated localization accuracy is $\sigma_z \sim 5$ nm and $\sigma_{xy} \sim 10$ nm. (b, d) x'z-image (i.e. 3D position data contracted in y' direction) of the distribution of labels located within the rectangles indicated in (a). (c, e) z-position histograms for the regions marked in (b) and (d). (f) xy-image of the Atto 532 labeled GpIIb/IIIa receptor protein of an activated platelet. The estimated localization accuracy is $\sigma_z \sim 7$ nm and $\sigma_{xy} \sim 14$ nm. (g) yz-image (i.e. 3D position data contracted in x direction) of the distribution of labels located within the rectangle indicated in (g). The z-axis is stretched by a factor of five. (h, i) z-position histograms for the regions marked in (g). Fitting a double-Gaussian delivered an estimate of $\sigma = 4.5 \pm 0.6$ nm and $\sigma = 5.5 \pm 0.4$ nm for the images of the upper and lower membranes respectively. The wider distributions in (h) can be attributed to the membrane curvature and a wider dye distribution. Scale bars: (a, f) 1 μ m, (b, d, g) 200 nm, (g) 1 μ m in x-direction and 200 nm in z-direction.

fluorophore positions within an indicated area is shown in Fig. 7.1g. Over the whole section the two membranes can be clearly resolved. Due to the low probability of less than 10% to assign an

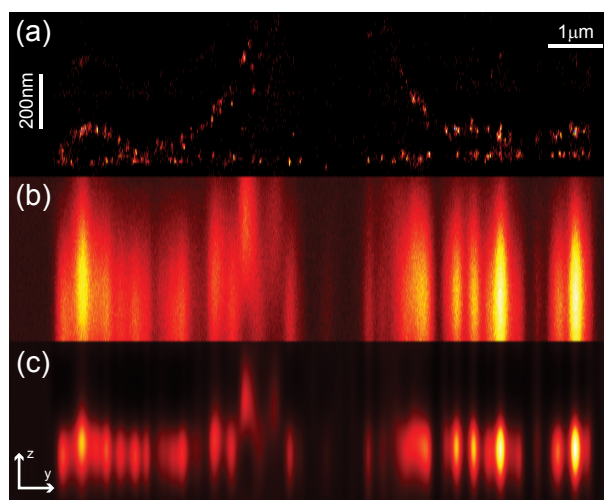


Figure 7.2 (a) 4Pi-SMS image shown in Fig. 7.2g without color coding. (b) Simulated confocal detection for the structure underlying (a). (c) Deconvolved image of (b). The membranes can only be identified separately in the 4Pi-SMS image.

event to the wrong period, a slight ghost image can be vaguely seen above the cell. Of course this has no influence on the localization accuracy of the correctly assigned events ($> 90\%$). Fig. 7.1h and i show histograms of the z -position for the regions marked in Fig. 7.1g. The height of the arch at the indicated position is ~ 115 nm (Fig. 7.1h) and the fluorophore positions can be determined with a σ of ~ 4.5 nm and ~ 5.5 nm where the upper and the lower membrane images are most narrow (Fig. 7.1i), corresponding to FWHMs of 10.6 nm and 13.0 nm which gives a conservative resolution estimate. Due to this high precision, it is possible to identify the marker fluorophores associated with the upper and the lower membranes, even at their closest distance of 32 nm. At the same time, toward the center of the cell where the membranes exhibit distances larger than $\Delta z_0 = 255$ nm, the run of the upper membrane is reproduced with equal confidence. The weak reproduction of the upper membrane for z -positions greater than 200 nm is most likely due to labeling issues for that sample.

To assess the potential of a 4Pi-SMS setup in comparison to a confocal microscope, the obtained SMS image in Fig. 7.2g was convolved with the calculated confocal PSF introduced in section 2.1.4. Additionally, Poisson noise with an expectation value of a tenth of the signal in each pixel and a background of 1 count per pixel was chosen. Fig. 7.2a shows the original SMS image without z color coding. Fig. 7.2b reveals the calculated confocal image, simulating an image obtained by a confocal acquisition. Obviously, a distinction of both membranes is not possible and even the shape of the cell is barely visible. Although the shape becomes more apparent if Fig. 7.2b is deconvolved with the confocal PSF the present separation of the membranes is still not visible (Fig. 7.2c). Note that this approach assumes that the positions determined in the 4Pi-SMS image are the real positions of the markers, thus it neglects the uncertainty in position determination of the high resolution image. Nevertheless, since the precision of the 4Pi-SMS position determination is much higher than the extension of the confocal PSF, this approach can be used to illustrate the capability of 4Pi-SMS.

The impact of employing further moments in contrast to solely analyzing the intensity can

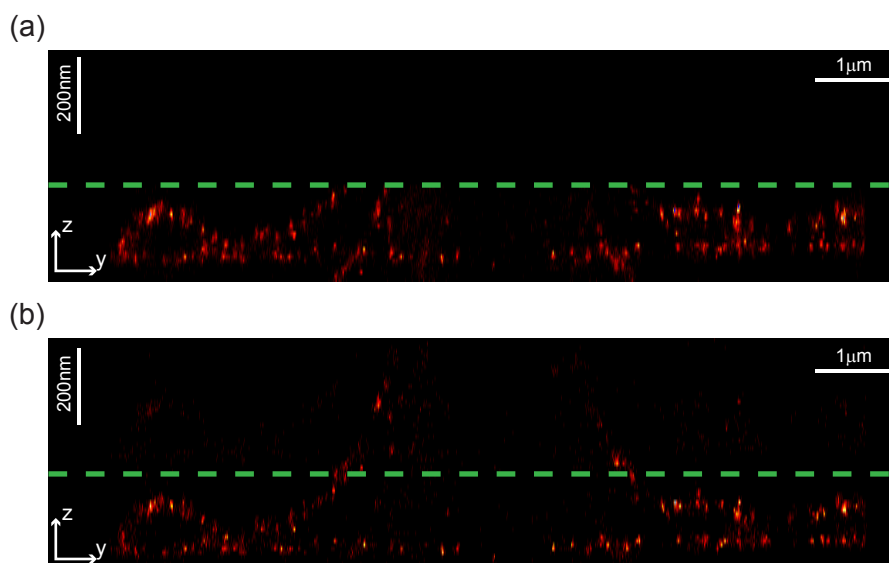


Figure 7.3 Well-defined fluorophore localization by employing moments of higher orders illustrated by means of the data underlying Fig. 7.1g: (a) By considering the relative intensities of the detection channels only, molecular events from outside the area close to the cover slip (255 nm, green line) are falsely back-projected into it. (b) By exploiting the high NA detection through including the 3rd central moment of the image into the analysis this ambiguity can be lifted, while preserving the high localization accuracy.

be seen in Fig. 7.3 which is based on the data shown in Fig. 7.1g. Fig. 7.3a only employs φ_0 to determine the z position, therefore events above an interval $\Delta z_0 \cong 255$ nm, indicated by the green dash line, are falsely back-projected into it. Thus the membrane shape is not recovered correctly. In Fig. 7.3b the data is evaluated by additionally exploiting the information inherent in φ_3 , allowing a correct rendering of the membrane. The advantage of the estimator developed in this work is not only the theoretically unlimited z range which can be imaged, but also the lift of the restriction to image samples near the cover slip and thus requiring e. g. TIRF illumination.

7.1.2 Samples for platelet imaging

Platelets were obtained from blood withdrawn from healthy volunteers to which a 10 % volume of 3.8 % (w/v) sodium citrate in water was added. Platelet-rich plasma (PRP) was obtained from the supernatant after a centrifugation step (120 g, 15 min, 22 °C) and a 15 % volume of an acid-citrate-dextrose solution (ACD, 2.2 % (w/v) sodium citrate, 0.8 % (w/v) citric acid, 2.2 % (w/v) glucose and 2 μM prostaglandin E1 (PGE₁, Sigma-Aldrich) was added. The suspension was centrifuged (1500 g, 7 min, 22 °C) yielding a platelet pellet, which was resuspended in Ringer's-citrate-dextrose (RCD) solution (0.76 % (w/v) citric acid, 0.09 % (w/v) glucose, 0.043 % (w/v) MgCl₂, 0.038 % (w/v) KCl, 0.6 % (w/v) NaCl and 2 μM PGE₁, pH 6.5). The suspension was centrifuged (1520 g, 7 m, 22 °C) and the pellet was resuspended in HEPES-Tyrode buffer (5.6 mM glucose, 10 mM HEPES, 2.7 mM KCl, 1 mM MgCl₂, 137 mM NaCl, 12 mM NaHCO₃, and 0.4 mM NaH₂PO₄, pH 7.4) containing 1 mM CaCl₂ to yield a platelet concentration of $2.0 \times 10^5 \mu\text{l}^{-1}$.

Platelets in HEPES-Tyrode buffer were placed onto cover slips carrying a thrombin coated nanosheet (93) (coating was performed with 10U/ml thrombin overnight at 4 °C) and incubated for 10 min at 37 °C. After incubation the non-adherent platelets were washed off. Then cells were fixed for 90 min with 4 % (w/v) formaldehyde in PBS at 4 °C, quenched in PBS containing 50 mM NH₄Cl at RT for 10 min and washed in PBS for 3 x 5 min. Then the platelets were extracted using 0.5 % (v/v) Triton X-100 in PBS for 10 min at RT and incubated at RT for 45 min with monoclonal mouse anti-human GPIIb antibody (BD Biosciences Co., San Diego, CA, USA) in 3 % (w/v) BSA/PBS containing 0.2 % (v/v) Triton X-100. Subsequently, they were washed in PBS 3 x 10 min, followed by a 45-min incubation with secondary antibody using either custom labeled RhS or Atto532 sheep anti-mouse (ATTO-TEC, Siegen, Germany) in 3 % (w/v) BSA/PBS containing a 0.2 % (v/v) Triton X-100. Finally, they were washed in PBS for 3 x 10 min and shipped in 4 % PFA in PBS to the Max Planck Institute for Biophysical Chemistry.

Upon arrival, PFA was quenched for 10 min at RT by a PBS solution containing 50 mM NH₄Cl. For imaging, samples were mounted in Tris-Buffer (50 mM Tris-HCl, 10 mM NaCl) containing 10 % (w/v) glucose, 0.25 mg/ml glucose oxidase, 0.06 mg/ml catalase and trolox (100 μM) (all Sigma-Aldrich) (94). They were covered with a second cover slip that was sparsely coated with fluorescent beads (FluoSpheres carboxylate-modified microspheres, 100 nm specified diameter, orange fluorescent 540/560, Invitrogen) as described above to facilitate the initial alignment of the microscope and for gauge measurements. 30000 (RhS) and 120000 (Atto532) images were acquired at 100 Hz. Exciting with a 532 nm Laser at an intensity of 7-14 kW/cm², on average 800 (RhS) and 380 (Atto532) photons per event were registered. RhS switches irreversibly from the off to the on-state, therefore each RhS molecule generates at most one detected event. Atto532 switches reversibly between the on and the off-state, therefore each Atto532 molecule might generate multiple detected events.

7.2 Deep Section Imaging of Cultured Mammalian Cells

Platelets are rather thin cells, and since 4Pi-SMS microscopy is not limited to the proximity of the cover slip, images of microtubule-cytoskeleton inside Vero cells stained with RhS will be shown next. The focal plane was roughly adjusted to the middle of the cell and 110000 frames at 100 frames per second were recorded, with continuous wave excitation at 532 nm, and at an illumination intensity of 7-14 kW/cm². Irradiation with activating UV light was not required, because at pH=7 the RhS molecules switch back to their on-state thermally at a sufficient rate.

7.2.1 Cytoskeleton of Microtubules - Results

An xy-histogram of the molecular positions spanning a range of ±500 nm around the focal plane is shown in Fig. 7.4a. For a better representation of the 3D structure the axial positions are color coded. Fig. 7.4b shows a close-up of the region indicated by the larger rectangle in Fig. 7.4a. In this region the filamentous network is distributed over a z-range of about 491 nm, as can be seen from the z-position histograms lying within the two indicated squares (Fig. 7.4c). Note that the z-position histogram of the markers associated with the lower fiber (c1) exhibits two distinct peaks with a σ of 12.2 nm and 9.2 nm respectively, separated by 46.2 nm and the histogram of the markers associated with the upper fiber (c2) exhibits two distinct peaks with a σ of 12.9 nm and 10.6 nm respectively, separated by ~ 43.5 nm. Since this is in good agreement with the diameter of microtubules (~ 25 nm) plus the double distance of the label from the epitope recognized by

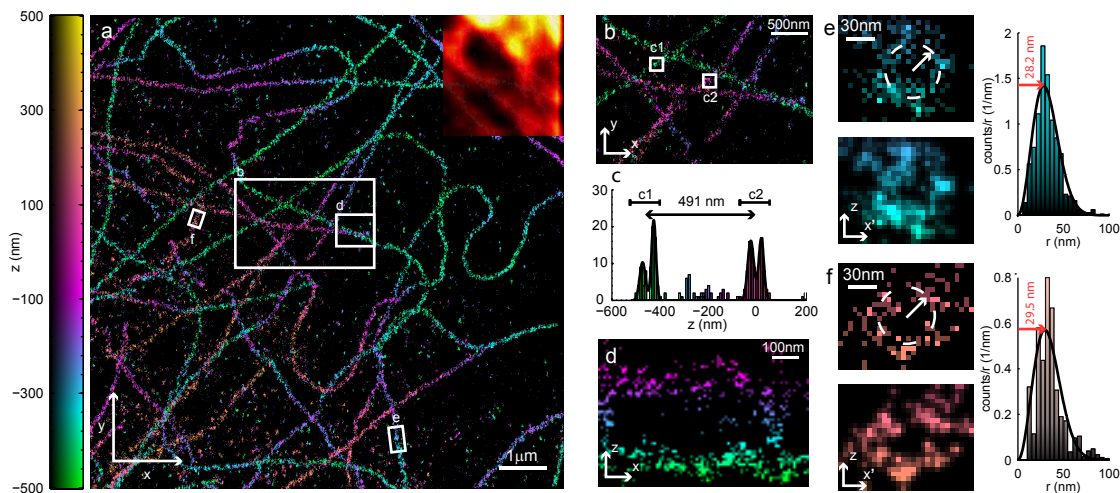


Figure 7.4 4Pi-SMS imaging with extended axial depth. (a) xy-image of the RhS labeled tubulin inside a Vero-cell. The color encodes the axial position of each label extending over about $1 \mu\text{m}$. The localization accuracy is $\sigma_z \sim 6 \text{ nm}$ and $\sigma_{xy} \sim 10 \text{ nm}$. (b) Magnified image of the area indicated in (a). (c) z-position histograms for the two regions marked in (b). The location of the two 491 nm distant fibers can be unambiguously determined. (d) xz-position histogram of the labels indicated in (a). (e, f) $x'z$ -image of the distribution of labels located within the rectangles indicated in (a), the same images smoothed with a Gaussian ($\sigma = 3.2 \text{ nm}$) for better visibility and the respective radial-position histograms. The ring-like structure reveals that only the surface of the tubules was labeled. Scale bars: (a) $1 \mu\text{m}$, (b) 500 nm, (d) 100 nm, (e, f) 30 nm.

the primary antibody ($\sim 10 \text{ nm}$), the 4Pi-SMS setup most likely discerns the upper from the lower part of the microtubule. Fig. 7.4d depicts the xz-histogram of the molecular positions lying within the region indicated by the smaller rectangle in Fig. 7.4a. The two fibers with an axial separation of 297 - 374 nm are clearly discerned and at some positions, the labels associated with the upper and lower part of the microtubule becomes apparent. To demonstrate that the present setup can indeed resolve how the fluorophores reside around the microtubules, $x'z$ position histograms integrated a few tens of nanometers along the tubules were extracted as shown in Fig. 7.4e and f for the regions indicated in Fig. 7.4a (see Fig. D.1 for more examples). In order to accentuate the ringlike shape of the fluorophore distribution, also a slightly smoothed version of the histograms is shown. Note that this smoothing has a similar effect as drawing a Gaussian for each located fluorophore, a representation also frequently used for SMS data. From the respective radial-position histograms the ring diameter can be determined to be in the range of 60 nm. The histograms are centered at the ring center indicated by the dashed white lines. The ring radius is (heuristically) calculated by fitting the function $ax^2 \exp[-(x/b)^2]$ to the histogram (black line) and using the maximum (indicated by the red arrows).

7.2.2 Samples for imaging of the tubulin cytoskeleton

For immunolabeling of tubulin, cultured Vero cells, originating from the African green monkey (kidney epithelia), *Chlorocebus sp.*, were grown on cover slips over night. For immuno labelling, the cells were fixed 5 min with ice cold methanol (abs.). After washing in PBS (137 mM NaCl, 3 mM KCl, 8 mM Na₂HPO₄, 1.5 mM KH₂PO₄, pH 7), the samples were blocked with 5% (w/v) bovine serum albumin in PBS and incubated with mouse monoclonal antibodies against α -Tubulin (Sigma Aldrich). The primary antibodies were detected with secondary antibodies (sheep anti-mouse Jackson ImmunoResearch Laboratories, West Grove, PA, USA) custom-labelled with Rhodamine S. The samples were spincoated with PVA (4% (w/v)) and mounted in PBS (pH 7.0) and covered with a second cover slip that was sparsely coated with fluorescent beads (FluoSpheres carboxylate-modified microspheres, 100 nm specified diameter, orange fluorescent 540/560, Invitrogen) as described above. 110000 images were acquired at 100 Hz, exciting with a 532 nm laser at an intensity of 7-14 kW/cm² and on average 700 photons per event were registered. As Rhodamine S switches irreversibly from the off- to the on-state, each dye molecule generates at most one detected event.

Chapter 8

Multicolor Expansion

The concept of solving the ambiguity problem by exploiting the spherical shape of the emission wavefronts presented in this work is more generally applicable. In fact, it will also eliminate the ambiguities reported in iPALM, i.e. in a system with three detection channels separated by equal phase shifts of $2\pi/3$. However, the full potential of the four channel detection scheme employed here comes into effect in multicolor imaging without additional detection channels, which is less straightforward to realize with a three channel system. Because the ratio of the combined s - versus the p -polarized intensities is independent of the emitter position, multiple fluorophore species can be differentiated by using the same method as in single-lens based two-channel setups (39): The 4Pi-SMS setup is merely tuned to translate any unmistakable hallmark in the fluorescence of a certain type of label into a characteristic value of this ratio which is then used for the classification. For example, two-color imaging is readily achieved by placing an additional long-pass filter in front of the camera (Fig. 4.1), which introduces a dye specific ratio of the s - and p -intensities.

8.1 Exploiting the 4th Channel

Analogous to the method described for multi-color GSDIM microscopy earlier (39), different dye species ν are separated based on a characteristic emission ratio in the detection channels. Since the z -estimator developed in this thesis is based on four instead of three channels (which are sufficient for mere z estimation), multi-color detection can be added to it by a simple modification which ensures that the relative intensities of the s - and p -polarized channels (the ratio of the sums of the two channels of each polarization is z -independent) varies between molecular species. Here, a dichroic mirror is added at an angle where the transmission characteristics strongly depend on the polarization direction. The edge is chosen at a position such that s and p polarized light is transmitted with significantly different relative efficiencies for the dye species involved in the measurement. Note that z -estimation as described above is not affected by this measure as it is designed to explicitly take this into account. Now let $p_s(\nu)$ and $p_p(\nu) = 1 - p_s(\nu)$ be the probability that a photon emitted by a dye of species ν is detected in the s or p -polarized channels, respectively. The ratio of p_s and p_p is then independent of the dye's orientation due to the $\lambda/4$ plates and given by the ratio of the total transmission efficiency for the two polarization directions, which is specific for the dye's emission spectrum.

A maximum-likelihood estimator for the species ν can be developed if the probabilities $p[n_s, n_p; \nu]$ of species ν producing an event (n_s, n_p) are given, where the n_κ are the $M_{0\kappa}$ calculated from the detected intensity distributions and normalized and discretized such that they estimate the actual

number of s and p polarized photons registered by the detector. The $p[n_s, n_p; \nu]$ are normalized,

$$\sum_{n_s, n_p} p[n_s, n_p; \nu] = 1 \quad (8.1)$$

and obtained from single color labeled gauge measurements. Assuming that all species have equal a -priori probability to be present at a given position, the species of an event in a mixed sample is estimated by

$$\nu_E(n_s, n_p) = \arg \max_{\nu} p[n_s, n_p; \nu] \quad (8.2)$$

where the n_{κ} are now the values calculated from the detected event. Obviously the estimation is less reliable in the overlap region and one can calculate a confidence level for each value pair (n_s, n_p) given by

$$c(n_s, n_p) = p[n_s, n_p; \nu_E(n_s, n_p)] / \sum_{\nu} p[n_s, n_p; \nu] \quad (8.3)$$

which essentially gives the probability of picking the correct type under the assumption that both have equal probability of occurring. Cross-talk can be reduced by excluding events that are likely to produce false assignments (events for which the confidence level is low). To this end a confidence threshold C is introduced. If, indeed, all species have the same a -priori probability of occurring, the confidence level gives the probability of a correct estimate and obviously discarding events with $c(n_s, n_p) < C$ will thus reduce the cross-talk. The cross-talk matrix and thus the cross-talk in real measurements is readily estimated from the gauge measurements:

$$c_{\nu\mu} = \sum_{n_s, n_p} \theta[c(n_s, n_p) - C] \delta_{\nu\nu_E(n_s, n_p)} p[n_s, n_p; \mu] \quad (8.4)$$

Inhomogeneous broadening usually widens the distributions $p[n_s, n_p; \nu]$ beyond the theoretically expected values when assuming a fixed expected ratio of s and p polarized light. Similar to the z -determination, one can attempt to assess these effects theoretically but it has proven much more reliable to use gauge measurements.

8.2 Biological Application

To demonstrate the potential of multicolor imaging with a 4Pi-SMS setup, cultured PtK2 cells were immunostained for peroxisomes with Atto532 and for tubulin with Atto565 and imaged. Above introduced methods allow to identify the biological structures by their specific labeling and simultaneously recover the 3D structure with the high resolution given by 4Pi-SMS.

8.2.1 Two Color Imaging of Cell Network and Peroxisomes

Fig. 8.1a shows the emission spectra of Atto532 and Atto565 as well as the transmission characteristics of the used long-pass filter (555dcxr, Chroma) under 45° illumination. The edge of the filter for the s -polarized light is shifted by about 30 nm from that for the p -polarized light, such that placing it in the detection path changes the relative detection efficiency of the s - versus p -polarized channels for fluorescence emitted by Atto532 and Atto565 to 0.50 and 0.81 respectively. The 2D-histogram in s - p space created from the color gauge measurement with single-labeled samples (Fig. 8.1b) shows that this allows one to distinguish between events from individual Atto532 and

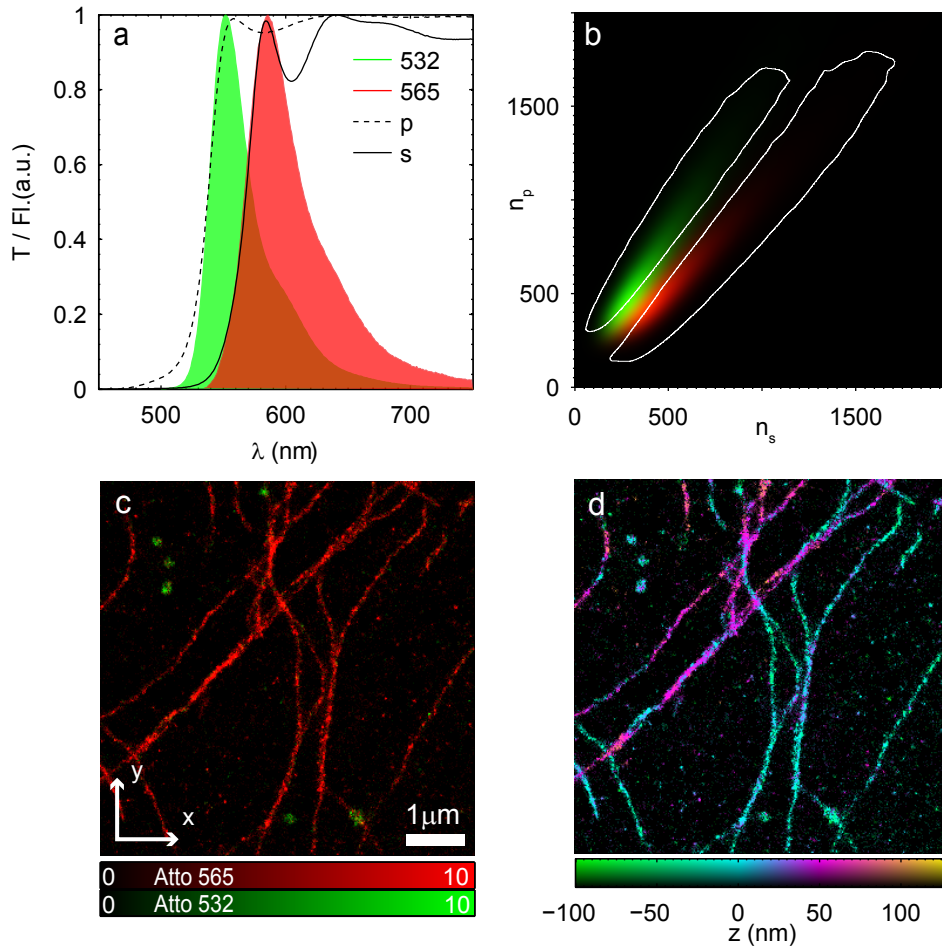


Figure 8.1 Two color imaging. (a) Fluorescence emission spectra of Atto 532 and Atto 565 as well as the transmission spectrum for *s*- and *p*-polarized light of the long pass filter. (b) *s*-*p* histogram of events in the gauge measurement performed on samples immunostained for peroxysomes (Atto 532, green) and microtubules (Atto 565, red). As expected, events from Atto 532 have a larger ratio of photons in the *p*- vs. the *s*-channel due to the higher transmission of the dichroic. The two fluorophores can thus be distinguished in *s*-*p* space. The white contour encloses the areas with a classification confidence better than 80%. Only events inside these regions were used in (c) and (d) reducing the cross-talk to < 6%. (c) *xy*-image of a PtK2-cell immunostained for both peroxysomes (Atto 532) and microtubules (Atto 565), color coded for the label. (d) *xy*-image of the same cell as shown in (c) but this time color coded for the *z*-position. Scale bar 1 μm and the localization accuracy can be estimated to be $\sigma_z \sim 6 \text{ nm}$ and $\sigma_{xy} \sim 12 \text{ nm}$ for both dyes.

Atto565 molecules based on the intensity ratio in the two channels. This is exemplified in Fig. 8.1c where an *xy*-histogram of the molecular positions derived from a PtK2 cell immunostained for peroxysomes (Atto532, green) and microtubules (Atto565, red) is shown. The single molecule nature of the approach allows one to exclude events that do not allow clear classification, thus trading dy-

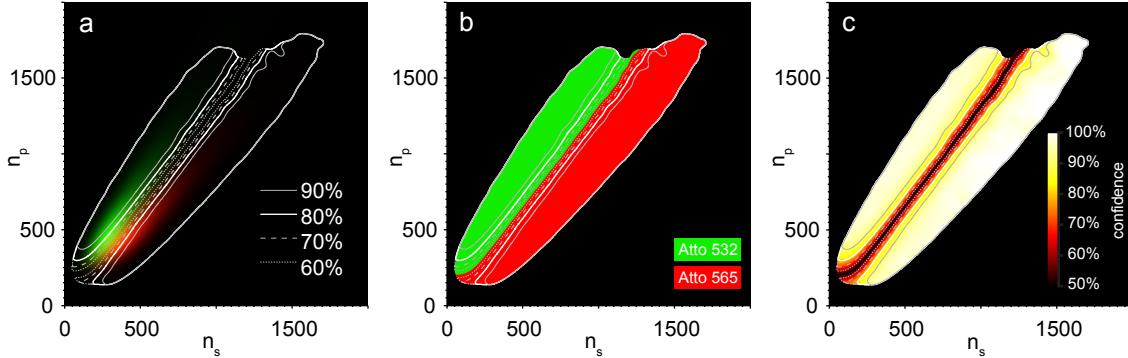


Figure 8.2 Dye classification in s-p-space. Data is from the gauge measurements used for Figure 4 in the manuscript. (a) Smoothed and normalized histograms containing the events from the Atto532-labelled sample (green) and those from the Atto 565-labelled sample (red). These distributions estimate the probabilities $p[n_s, n_p; \nu]$ of species $\nu = \text{Atto532}, \text{Atto565}$ producing an event with n_p photons in the p-polarized channels and n_s photons in the s-polarized channels. (b) Classification map used in Figure 4c of the manuscript. The green (red) region marks (n_s, n_p) values for which the estimator classifies an event as stemming from an Atto532 (Atto 565) molecule. (c) Confidence level, i.e. the probability of correctly assigning an event if both species have the same probability of occurring as a function of (n_s, n_p) . Regions where the histogram dropped below a value of 0.125 (black area in b) are set to 50%. The confidence level is also indicated by contours at 60, 70, 80 and 90 percent in all panels.

dynamic range for lower cross-talk (39). Here only events for which the gauge measurement suggests a classification confidence higher than 80% are included, which results in a residual cross-talk of 6% for both Atto532 and Atto565 respectively. Because the z-position is extracted from intensity ratios of the channel pairs of channels with equal polarization (which are not influenced by the polarization properties of the filter), z-localization can be performed as before (Fig. 8.1d). It should be noted that by using the long pass filter, the total signal of Atto532 is attenuated by 29% and the signal of Atto565 by 13%, which results in a small relative reduction of resolution of 16% and 7% respectively.

Fig. 8.2a depicts $p[n_s, n_p; \nu]$ defined in eq. (8.1) and extracted from the gauge measurement used for Fig. 8.1. To minimize the effect of shot-noise on the estimator the histograms (consisting of 800x800 bins) were smoothed with a Gaussian (FWHM 24 bins). The resulting estimator and confidence level is depicted in 8.2b and c, respectively. Regions where the smoothed and added histograms from the gauge measurement dropped below a value of 0.125 were also excluded. The cross-talk estimation from this gauge measurement is obtained by simply classifying the events contained in the gauge measurement with the estimator and quantifying the false assignments. In Fig. 8.1 a confidence threshold of $C = 80\%$ was used resulting in <6% false assignments for both Atto565 and Atto532, while about 40% of the events are discarded due to the threshold.

In order to check the reliability of this method and of the cross-talk estimates, a cross-validation of additional gauge measurements was performed on two Atto532 and three Atto565 samples. 6 estimators were extracted by pairing every Atto532 measurement with every Atto565 measurement and for each of them the cross-talk was checked which is produced when classifying the gauge measurements at an 80% confidence threshold. The cross-talk values found were $5\% \pm 1\%$ for

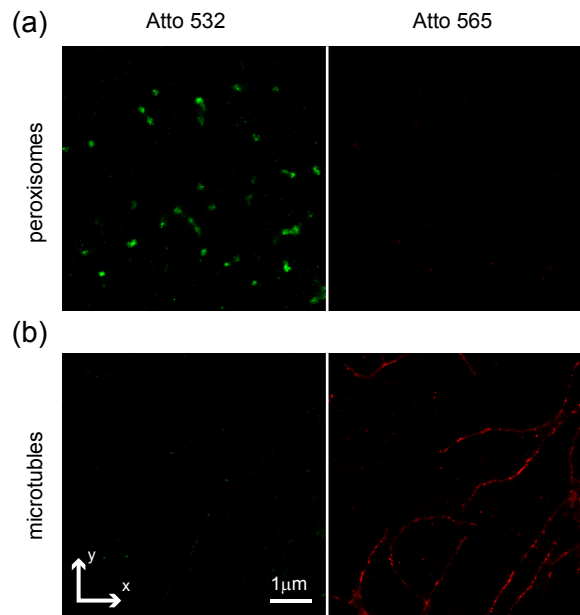


Figure 8.3 Superresolution images generated from the color gauge measurements. (a) Gauge measurement for peroxisomes labeled with Atto 532. The derived classification map was applied to check for systematic cross-talk (e.g. correlated with position in the sample). The left panel shows those events classified as Atto532 and the right panel those as Atto565 (<6%). (b) Gauge measurement for tubulin labeled with Atto 565. Again classification was performed and the right panel contains those events correctly identified as Atto565 while the left panel contains the cross-talk (<6%).

Atto532 (number of estimates $n = 12$) and $8\% \pm 1\%$ for Atto565 ($n = 18$). The small variation confirms the validity of the approach employed here and the difference to the values found for the gauge measurement shown in Fig. 8.1 is rooted in the fact that the setup had been re-aligned, slightly changing the detection efficiencies of the dyes.

8.2.2 Samples for Two Color Imaging

For immunolabeling of tubulin and PMP70, cultured PtK2 cells, originating from the marsupial (kidney epithelia), *Potorous tridactylus*, were grown on cover slips over night. For immunolabelling, the cells were fixed 5 min with ice cold methanol (abs.). After washing in PBS, the samples were blocked with 5% (w/v) bovine serum albumin in PBS and incubated with mouse monoclonal antibodies against α -Tubulin (Sigma Aldrich) and polyclonal rabbit antibodies against PMP70 (Abcam, Cambridge, MA, USA). The primary antibodies were detected with secondary antibodies (sheep anti-mouse, goat anti-rabbit, Jackson ImmunoResearch Laboratories, West Grove, PA, USA) custom-labelled with Atto565 and Atto532 (both ATTO-TEC, Siegen, Germany). To create an oxygen free environment for imaging, the samples were mounted in Tris-Buffer containing glucose oxidase and Catalase (Sigma Aldrich), as already described in chapter 7. Finally all samples were covered with a second cover slip that was sparsely coated with fluorescent beads (FluoSpheres carboxylate-modified microspheres, 100 nm specified diameter, orange

fluorescent 540/560 and red fluorescent 580/605, Invitrogen) as described in the former chapter. 30000 images were acquired at 100 Hz by exciting with a 532 nm laser at an intensity of 7-14 kW/cm² and on average 520 (Atto532) and 500 (Atto565) photons per event were registered. As Atto532 and Atto565 switch reversibly between the on and the off-state, each dye molecule might generate multiple detected events.

Chapter 9

Conclusion

In this work the SMS concept was combined with the 4Pi technique to achieve high sub-diffraction resolution in all three spatial dimensions. Utilizing the polarization of the electrical field to create the required signals, the use of a typical 4Pi cavity with standard optical components is possible. By exploiting the spherical wavefront shape of the fluorescence emission, the 4Pi-based SMS setup is able to localize different types of individual fluorophores unambiguously inside a 1 μm thick section within a thick sample with unsurpassed accuracy. Importantly, since the method is not restricted to any specific dye or fluorescent protein, it can be combined with virtually all stochastic superresolution modalities and its application is not technically limited to fixed samples. The biological applicability was proven for different biological systems and with different types of markers. If the imaging acquisition is fast enough, its application to dynamic studies in living cells should be readily feasible. In fact, a 4Pi setup utilizing the same configuration of the same water immersion lenses as used in the present study was capable of imaging living cells over many hours (95).

The method of localizing emitters has been implemented under the assumption that the molecules can freely rotate on timescales of several milliseconds, which may not be the case in some types of samples due to low viscosity of the embedding medium or steric reasons. For fixed or slowly rotating emission dipoles, asymmetric fluorescence emission could compromise the accuracy of the localizations. Importantly, this restriction applies to any stochastic method implemented so far and there has not been any evidence of this being the case in the data presented here. Moreover, for future studies in aqueous environments the speed at which molecules tumble around the optic axis will most likely increase even further. Nevertheless, studies on the impact of tilted dipoles were already reported (90) and they will certainly be extended. In any case, the 4Pi-SMS setup introduced in this thesis can be easily adapted to new findings and will therefore always provide a 3D localization superior to that of a single lens based system. In the future, the problem caused by the anisotropic emission of a dipole could be completely avoided by using isotropic emitters, like for example quantum dots.

Like all SMS concepts, 4Pi-SMS will benefit from faster cameras with an enlarged field of view and from fast switching markers which emit many thousand of photons in short bursts. This will reduce the data acquisition time and improve the resolution. Finally, such high photon yields will allow position determination with a precision below 1 nm, where resolution is not limited by the imaging process anymore, but rather by the marker size, linker length and marker motion. An influence of the linker lengths on the image was already observed in this work for the Atto532 labeled tubulin which revealed a ringlike labeling around the tubules.

The analysis used for the z determination does not completely rule out the possibility to incorrectly assign a marker to a plane Δz_0 ($\sim \lambda/2$) above or below the actual plane. The probability of such an assignment error depends on the number of detected photons, but for the fluorophores

used in this study it was almost negligible. The development of brighter labels will lessen these small artifacts even further. Recently developed localization algorithms based on maximum likelihood estimator promise to improve the precision of lateral position determination (75, 76). Since the z determination is based on the calculation of cylindric symmetric moments centered at the localized xy position, it would be worth to investigate if more precise xy values of such estimators also enhance the precision of z analysis. An other approach to reduce the impact of misallocations of dim markers is to investigate whether a mathematical algorithm similar to deconvolution can be developed, for the nonlinear process of assigning each marker to a certain period, which is conducted during the z determination.

Brighter labels will also increase the axial extent of the volume which can be observed simultaneously. Note that in case of an increasing distance to the focal plane, it has to be considered that the Gaussian approximation of the PSF used in the localization process becomes less accurate. However, this issue can be addressed by either employing improved fitting functions or adapted maximum likelihood estimator as mentioned above, which take the ring-like structure into account generated by markers far out of focus. Extending the axial field of view should also be possible by incorporating optical elements for focal extension (96) into the detection path and possibly raising the number of central moments employed in case the ‘depth of field’ becomes so large that the combination of two central moments will no longer allow extraction of a unique z-position. However, because in the current configuration markers outside the useable axial range are recognized, the simplest way to acquire image stacks of much larger depth is to scan the object along z recording micron thick slices around different focal planes. In this case, standard two photon activation or two photon activation in 4Pi mode are promising options to reduce the amount of discarded events and thus to allow an increased imaging density of accepted events. This might result in a faster data acquisition and less bleaching, provided that the two photon activation does not open further bleaching channels. However, note that an additional constraint of the light field, such as TIRF or two photon activation, is not required in the case of 4Pi-SMS, the full z information can be extracted from the PSF by the methods introduced in this thesis.

In this work resolutions better than 10 nm were achieved for conventional dyes, which is already in the order of the residual setup instabilities of about 2 nm. Therefore, future designs should attempt to improve the setup stability even further to fully exploit the resolution potential of 4Pi-SMS.

In the implementation of 4Pi-SMS used in this work, the oscillations of the 0th and 3rd central moments were employed for axial position determination, since out of several combinations, it gave the best balance between accuracy and reliability. As it was not rigorously proven that the estimator used is the global optimum, it may be possible to slightly improve the accuracy of the method by selecting other combinations of central moments, other sets of rotationally symmetric weight functions or even a new type of estimator. Experimentally conceivable are for instance a separation of the inner and outer part of the wavefronts before focusing to avoid mixing of the different modulation frequencies which is intrinsic to the focusing process. Thus the full frequency contrast between outer and inner parts of the wavefronts would be available, however at the cost of broader detection PSFs.

It was opted to use a single camera for all four detection channels. While this reduces the field of view, it has several major advantages beyond the obvious economic factor: Using one instead of three (iPALM) or even four cameras is cheaper and makes synchronisation and calibration for differences in gain or quantum efficiency of several cameras obsolete.

It is important to note again that using four channels is not mandatory to implement the scheme

of unambiguous z-localization developed here. Spherical fluorescence wave-fronts are of course also prevalent in any three-channel setup, but so far they were not exploited. Given that the appropriate calibration data is recorded, the method presented in this thesis is therefore directly applicable to the iPALM scheme, allowing these microscopes to unambiguously image over a larger z-range and within axially extended samples. The z-resolution of 3- and 4-channel setups merely depends on the steepness of the oscillating intensities at a given axial position and the photon budget and will thus be almost similar for both schemes. However, the use of four channels allows the use of standard optical elements and, more importantly, inherently enables the discrimination between several molecular species based on the same principle as in a two-channel single lens setup. For this reason, the two colour image shown in this work should be seen as representative for a much wider spectrum of potential 4Pi-SMS applications in which three or even more fluorophore species are separated by color, or after modifications to the setup, by any other feature (39, 38) such as anisotropy, rotational mobility (97) or lifetime, always providing the highest 3D resolution that is technically achievable in a stochastic superresolution scheme.

To conclude, this thesis has established a nanoscope with a resolution well below 10 nm in all three spatial dimensions in biological samples. The resolution is not only superior to single lens based methods, it is also approximately homogeneous along the z axis in comparison to single lens based methods. Future bright markers will enable 3D-resolutions below 1 nm. By exploiting the spherical wavefront of an emitter, the sample thickness is not limited to slices thinner than $\Delta z_0 \sim \lambda/2$, theoretically an unlimited z range is possible. An easy multicolor expansion has been demonstrated from which most biological applications will benefit.

Thus, one of the most important features of light microscopy, which is noninvasive imaging of thick samples is now feasible with highest possible 3D-resolution by simultaneously enabling marker discrimination by specific properties.

Appendix A

List of Acronyms

STED	stimulated emission depletion	2
GSD	ground-state depletion	3
RESOLFT	reversible saturable optical fluorescence transitions	3
PALM	photoactivated localization microscopy	3
fPALM	fluorescence photoactivation localization microscopy	3
STORM	stochastic optical reconstruction microscopy	3
dSTORM	direct STORM	3
GSDIM	ground state depletion microscopy followed by individual molecule return	3
SMS	single marker switching	3
STM	scanning tunneling microscopy	2
AFM	atomic force microscope	2
PALMIRA	PALM with independently running acquisition	3
EMCCD	electron multiplying charge coupled device	24
FWHM	full width at half maximum	4
OTF	optical transfer function	8
PSF	point spread function	3
SNR	signal-to-noise ratio	2
TIRF	total internal reflection fluorescence	23
SSIM	saturated structured illumination microscopy	3
SPEM	saturated patterned excitation microscopy	3
PAINT	points accumulation for imaging in nanoscale topography	3
TL-PALM	time-lapse PALM	3
NA	numerical aperture	1
IC	internal conversion	10
ISC	inter system crossing	10
PMT	photo multiplier tube	14
APD	avalanche photo diode	14
2P	two photon	16

GPUs	graphics processing units	25
MLEs	maximum likelihood estimators	24
BS	beamsplitter	34
SLM	spatial light modulator	35
PMMA	poly methyl methacrylate	36
fov	field of view	36
DH-PSF	double helix point spread function	35
BP FPALM	biplane fluorescence photoactivation localization microscopy	34
PSD	position sensitive diode	45

Appendix B

Statistics - Moments

Let $p(x)$ be the probability density of the random variable X , thus $p(x)dx$ is the probability that X obtains the values between $[x, x + dx]$. As the whole probability is one, $p(x)$ is normalised.

$$\int_{-\infty}^{\infty} dx p(x) = 1 \quad (\text{B.1})$$

If $F(X)$ is a function of the random variable X , its mean value is defined by,

$$\langle F(X) \rangle := \int dx p(x) F(x) \quad (\text{B.2})$$

The n -th moment of the probability distribution $p(x)$ is defined by,

$$M_l := \langle X^l \rangle \quad (\text{B.3})$$

The *characteristic function* is given by,

$$\chi(k) := \int dx e^{-ikx} p(x) \equiv \langle e^{-ikX} \rangle \quad (\text{B.4})$$

Hence $\chi(k)$ is the Fourier transform of $p(x)$. This implies,

$$p(x) = \int \frac{dk}{2\pi} e^{ikx} \chi(k) \quad (\text{B.5})$$

Under the assumption that all moments exist, the characteristic function can be written as,

$$\chi(k) \equiv \langle e^{-ikX} \rangle = \sum_l \frac{(-ik)^l}{l!} \langle X^l \rangle \quad (\text{B.6})$$

inserting eq. (B.6) in eq. (B.5) gives,

$$p(x) = \int \frac{dk}{2\pi} e^{ikx} \sum_l \frac{(-ik)^l}{l!} M_l \quad (\text{B.7})$$

Thus a probability function is defined by all its moments.

Appendix C

The Stabilization Module

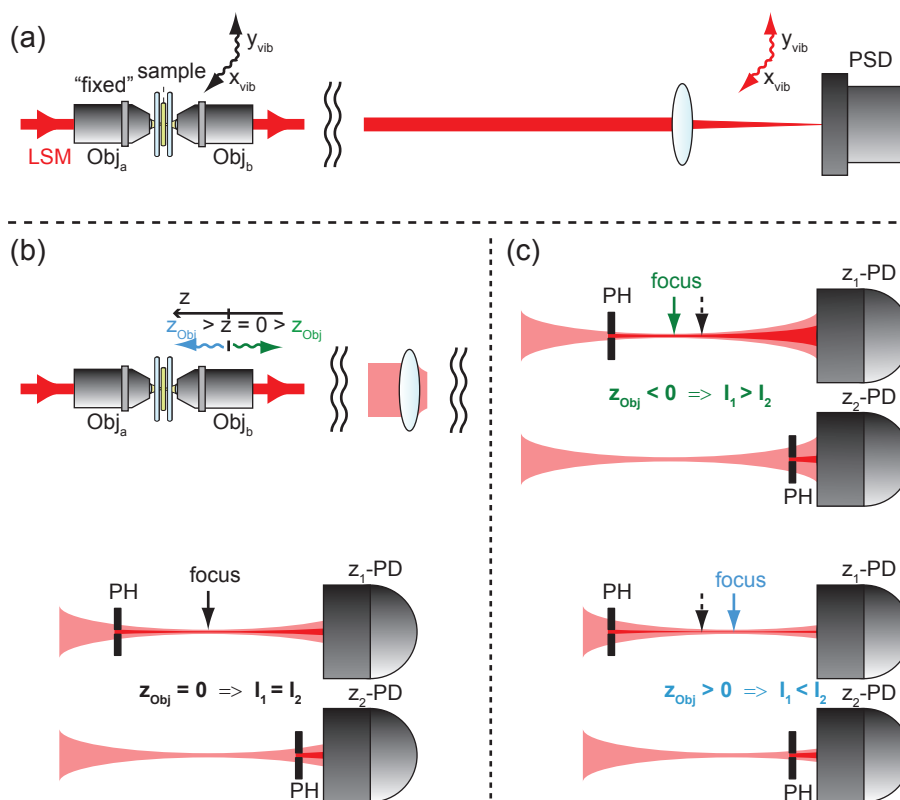


Figure C.1 (a) The relative xy -motion between objectives a and b are detected by a position sensitive diode (PSD). (b) The relative z -motion is detected by a system of two pinholes (PH) and two photo diodes (z -PD). The collimated beam after objective b is divided by a beamsplitter (Fig. 4.1b) and focused in front of both photo diodes. In one arm the pinhole is placed in front of the focus in the other arm the pinhole is placed behind it. The system is adjusted such that, if the foci of objective a and b coincide ($z=0$), the intensities passing both pinholes (indicated by the dark red beams) and detected by the z -PDs are equal. (c) If the relative z position of both objectives changes the focal planes in front of the z -PDs move and the intensities passing the pinholes become different in both arms. The signals generated are analyzed by a PID-controller implemented in LABVIEW. Objective b is mounted on a xyz-piezo stage which is adjusted by the PID-controller to correct for the deviations.

Appendix D

Tubulin rings

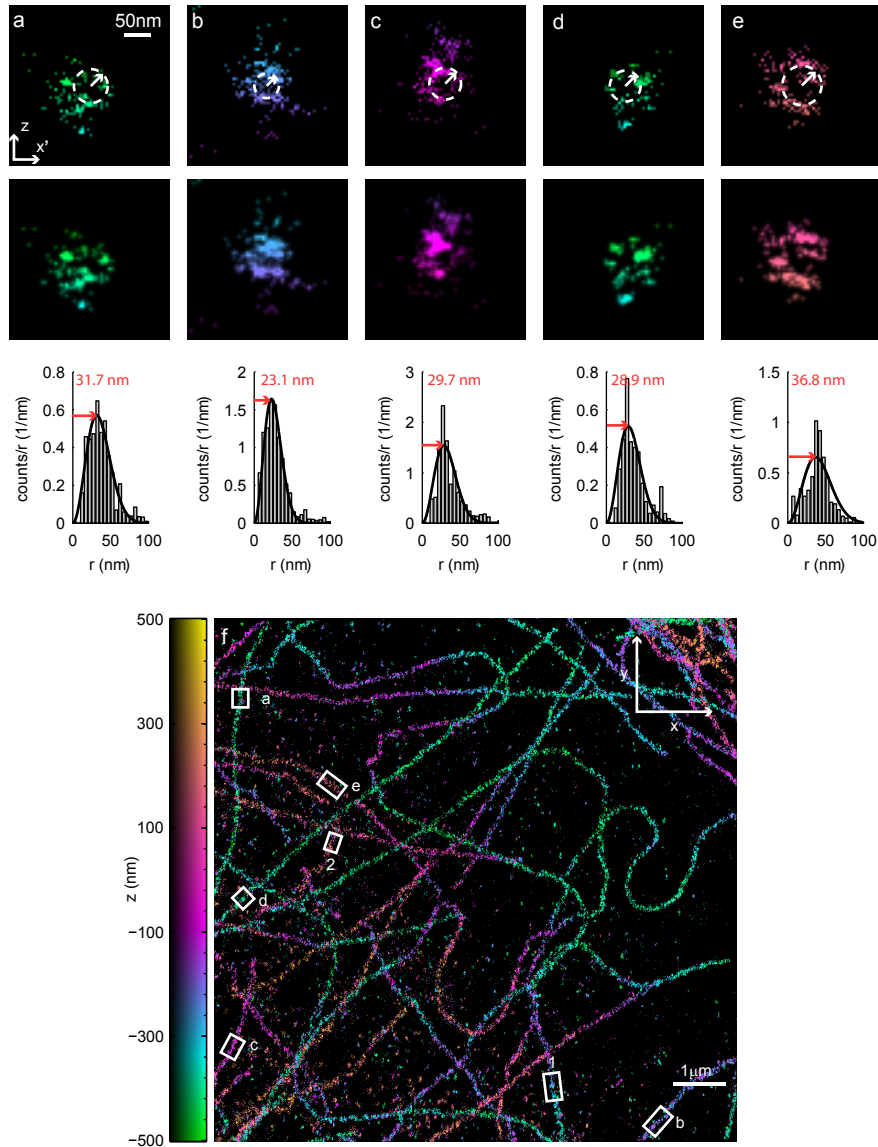


Figure D.1 Additional rings of labels around tubulin. (a-e) $x'z$ -image of the distribution of labels located within the rectangles indicated in (f). The upper row shows the $x'z$ -histograms, the second row exhibits the same images smoothed with a Gaussian ($\sigma = 3.2\text{nm}$) for better visibility. The bottom row shows the respective radial-position histograms centered at the ring center shown in the upper row. The ring radius (heuristically) calculated by fitting the function $ax^2 \exp[-(x/b)^2]$ to the histogram (black line) and using the maximum (indicated by the red arrows). The ring-like structure is due to the fact that only the surface of the tubules was labeled. (f) Like Fig. 7.4, extended by boxes indicating the regions of (a-e). The rings shown in Fig. 7.4 are indicated by the boxes 1 and 2. The mean fit radius of all rings is $29.7 \pm 4.1\text{ nm}$.

Bibliography

- [1] E. Verdet. *Lecons d'optique physique*, 1869.
- [2] E. Abbe. Beiträge zur Theorie des Mikroskops und der mikroskopischen Wahrnehmung. *Arch. Mikr. Anat.*, 9:413–468, 1873.
- [3] Lord Rayleigh. On the theory of optical images, with special reference to the microscope. *Philos. Mag.*, XLII:167–195, 1896.
- [4] P. Török, P. Varga, Z. Laczik, and G. R. Booker. Electromagnetic diffraction of light focused through a planar interface between materials of mismatched refraction indices: an integral representation. *J. Opt. Soc. Am. A*, 12(2):325–332, 1995.
- [5] G. Binnig and H. Rohrer. Scanning tunneling microscopy. *Helv. Phys. Acta*, 55:726–735, 1982.
- [6] G. Binnig, C. F. Quate, and Ch. Gerber. Atomic force microscope. *Phys. Rev. Lett.*, 56:930–933, 1986.
- [7] Lukas Novotny and Bert Hecht. *Principles of Nano-Optics*. Cambridge Univ. Press, Cambridge, 2006.
- [8] J. B. Pendry. Negative refraction makes a perfect lens. *Physical Review Letters*, 85(18):3966, October 2000.
- [9] Zhaowei Liu, Hyesog Lee, Yi Xiong, Cheng Sun, and Xiang Zhang. Far-Field optical hyperlens magnifying Sub-Diffraction-Limited objects. *Science*, 315(5819):1686, March 2007.
- [10] Igor I. Smolyaninov, Yu-Ju Hung, and Christopher C. Davis. Magnifying superlens in the visible frequency range. *Science*, 315(5819):1699–1701, March 2007.
- [11] G. Toraldo di Francia. Supergain antennas and optical resolving power. *Nuovo Cimento Suppl.*, 9:426–435, 1952.
- [12] A. N. Boto, P. Kok, D. S. Abrams, S. L. Braunstein, C. P. Williams, and J. P. Dowling. Quantum interferometric optical lithography: Exploiting entanglement to beat the diffraction limit. *Phys. Rev. Lett.*, 85(13):2733–2736, 2000.
- [13] S.W. Hell. Double confocal microscope. *European Patent*, 1:0491289, 1990.
- [14] S. W. Hell and E. H. K. Stelzer. Fundamental improvement of resolution with a 4Pi-confocal fluorescence microscope using two-photon excitation. *Opt. Commun.*, 93:277–282, 1992.

- [15] Alexander Egner, Stefan Jakobs, and Stefan W. Hell. Fast 100-nm resolution three-dimensional microscope reveals structural plasticity of mitochondria in live yeast. *Proceedings of the National Academy of Sciences of the United States of America*, 99(6):3370–3375, March 2002. PMID: 11904401 PMCID: 122530.
- [16] M G Gustafsson, D A Agard, and J W Sedat. I5M: 3D widefield light microscopy with better than 100 nm axial resolution. *Journal of Microscopy*, 195(Pt 1):10–16, July 1999. PMID: 10444297.
- [17] Stefan W. Hell and Jan Wichmann. Breaking the diffraction resolution limit by stimulated emission: stimulated-emission-depletion fluorescence microscopy. *Optics Letters*, 19(11):780–782, June 1994.
- [18] T. A. Klar, S. Jakobs, M. Dyba, A. Egner, and S. W. Hell. Fluorescence microscopy with diffraction resolution limit broken by stimulated emission. *Proc. Natl. Acad. Sci. USA*, 97:8206–8210, 2000.
- [19] T. A. Klar, E. Engel, and S. W. Hell. Breaking abbe’s diffraction resolution limit in fluorescence microscopy with stimulated emission depletion beams of various shapes. *Phys. Rev. E*, 64:066613, 1–9, 2001.
- [20] V. Westphal, L. Kastrup, and S. W. Hell. Lateral resolution of 28nm ($\lambda/25$) in far-field fluorescence microscopy. *Appl. Phys. B*, 77(4):377–380, 2003.
- [21] Benjamin Harke, Jan Keller, Chaitanya K. Ullal, Volker Westphal, Andreas Schönle, and Stefan W. Hell. Resolution scaling in STED microscopy. *Optics Express*, 16(6):4154–4162, March 2008.
- [22] S. W. Hell and M. Kroug. Ground-state depletion fluorescence microscopy, a concept for breaking the diffraction resolution limit. *Appl. Phys. B*, 60:495–497, 1995.
- [23] S. W. Hell. Toward fluorescence nanoscopy. *Nature Biotechnol.*, 21(11):1347–1355, 2003.
- [24] S. W. Hell. Strategy for far-field optical imaging and writing without diffraction limit. *Phys. Lett. A*, 326(1-2):140–145, 2004.
- [25] S. W. Hell, M. Dyba, and S. Jakobs. Concepts for nanoscale resolution in fluorescence microscopy. *Curr. Opin. Neurobio.*, 14(5):599–609, 2004.
- [26] Michael Hofmann, Christian Eggeling, Stefan Jakobs, and Stefan W. Hell. Breaking the diffraction barrier in fluorescence microscopy at low light intensities by using reversibly photoswitchable proteins. *Proceedings of the National Academy of Sciences of the United States of America*, 102(49):17565–17569, December 2005.
- [27] Rainer Heintzmann, Thomas M. Jovin, and Christoph Cremer. Saturated patterned excitation microscopy - a concept for optical resolution improvement. *J. Opt. Soc. Am. A: Optics and Image Science, and Vision*, 19(8):1599–1609, 2002. TY - JOUR.
- [28] M. G. L. Gustafsson. Nonlinear structured-illumination microscopy: Wide-field fluorescence imaging with theoretically unlimited resolution. *Proceedings of the National Academy of Sciences of the United States of America*, 102(37):13081–13086, 2005.

- [29] Lothar Schermelleh, Peter M. Carlton, Sebastian Haase, Lin Shao, Lukman Winoto, Peter Kner, Brian Burke, M. Cristina Cardoso, David A. Agard, Mats G. L. Gustafsson, Heinrich Leonhardt, and John W. Sedat. Subdiffraction multicolor imaging of the nuclear periphery with 3D structured illumination microscopy. *Science*, 320(5881):1332–1336, June 2008.
- [30] Eric Betzig, George H. Patterson, Rachid Sougrat, O. Wolf Lindwasser, Scott Olenych, Juan S. Bonifacino, Michael W. Davidson, Jennifer Lippincott-Schwartz, and Harald F. Hess. Imaging intracellular fluorescent proteins at nanometer resolution. *Science*, 313(5793):1642–1645, September 2006.
- [31] Michael J Rust, Mark Bates, and Xiaowei Zhuang. Sub-diffraction-limit imaging by stochastic optical reconstruction microscopy (STORM). *Nat Meth*, 3(10):793–796, October 2006.
- [32] Samuel T. Hess, Thanu P.K. Girirajan, and Michael D. Mason. Ultra-High resolution imaging by fluorescence photoactivation localization microscopy. *Biophysical Journal*, 91(11):4258–4272, December 2006.
- [33] Alexander Egner, Christian Eggeling, Andreas Schönle, Stefan W. Hell, Claudia Geisler, Claas von Middendorff, Hannes Bock, Dirk Wenzel, Rebecca Medda, Martin Andresen, Andre C. Stiel, and Stefan Jakobs. Fluorescence nanoscopy in whole cells by asynchronous localization of photoswitching emitters. *Biophysical Journal*, 93(9):3285–3290, November 2007.
- [34] Jonas Fölling, Mariano Bossi, Hannes Bock, Rebecca Medda, Christian A Wurm, Birka Hein, Stefan Jakobs, Christian Eggeling, and Stefan W Hell. Fluorescence nanoscopy by ground-state depletion and single-molecule return. *Nat Meth*, 5(11):943–945, November 2008.
- [35] Alexey Sharonov and Robin M. Hochstrasser. Wide-field subdiffraction imaging by accumulated binding of diffusing probes. *Proceedings of the National Academy of Sciences*, 103(50):18911–18916, December 2006.
- [36] M. Heilemann, S. Van De Linde, M. Schuttpelz, R. Kasper, B. Seefeldt, A. Mukherjee, and van de Linde. Subdiffraction-resolution fluorescence imaging with conventional fluorescent probes. *Angewandte Chemie (International ed. in English)*, 47(33):6172–6176, 2008.
- [37] Julie S Biteen, Michael A Thompson, Nicole K Tselentis, Grant R Bowman, Lucy Shapiro, and W E Moerner. Super-resolution imaging in live caulobacter crescentus cells using photoswitchable EYFP. *Nat Meth*, 5(11):947–949, November 2008.
- [38] Andreas Schönle and Stefan W Hell. Fluorescence nanoscopy goes multicolor. *Nat Biotech*, 25(11):1234–1235, November 2007.
- [39] Mariano Bossi, Jonas Fölling, Vladimir N. Belov, Vadim P. Boyarskiy, Rebecca Medda, Alexander Egner, Christian Eggeling, Andreas Schönle, and Stefan W. Hell. Multicolor Far-Field fluorescence nanoscopy through isolated detection of distinct molecular species. *Nano Letters*, 8(8):2463–2468, 2008.
- [40] Stefan W. Hell. Far-Field optical nanoscopy. *Science*, 316(5828):1153–1158, May 2007.

- [41] Stefan W Hell. Microscopy and its focal switch. *Nat Meth*, 6(1):24–32, January 2009.
- [42] S. W. Hell, S. Jakobs, and L. Kastrup. Imaging and writing at the nanoscale with focused visible light through saturable optical transitions. *Appl. Phys. A*, 77:859–860, 2003.
- [43] Jonas Fölling, Vladimir Belov, D. Riedel, Andreas Schönle, Alexander Egner, Christian Eggeling, Mariano Bossi, and Stefan W. Hell. Fluorescence nanoscopy with optical sectioning by Two-Photon induced molecular switching using Continuous-Wave lasers. *ChemPhysChem*, 9(2):321–326, 2008.
- [44] Bo Huang, Wenqin Wang, Mark Bates, and Xiaowei Zhuang. Three-Dimensional Super-Resolution imaging by stochastic optical reconstruction microscopy. *Science*, 319(5864):810–813, February 2008.
- [45] Manuel F Juetten, Travis J Gould, Mark D Lessard, Michael J Mlodzianoski, Bhupendra S Nagpure, Brian T Bennett, Samuel T Hess, and Joerg Bewersdorf. Three-dimensional sub-100 nm resolution fluorescence microscopy of thick samples. *Nat Meth*, 5(6):527–529, June 2008.
- [46] Marcus Dyba and Stefan W. Hell. Focal spots of size $\lambda/23$ open up Far-Field fluorescence microscopy at 33 nm axial resolution. *Physical Review Letters*, 88(16):163901, April 2002.
- [47] M. Dyba, S. Jakobs, and S. W. Hell. Immunofluorescence stimulated emission depletion microscopy. *Nature Biotechnol.*, 21(11):1303 – 1304, 2003.
- [48] Roman Schmidt, Christian A Wurm, Stefan Jakobs, Johann Engelhardt, Alexander Egner, and Stefan W Hell. Spherical nanosized focal spot unravels the interior of cells. *Nat Meth*, 5(6):539–544, June 2008.
- [49] Claas v. Middendorff, Alexander Egner, Claudia Geisler, Stefan W. Hell, and Andreas Schönle. Isotropic 3D nanoscopy based on single emitter switching. *Optics Express*, 16(25):20774–20788, December 2008.
- [50] Stefan Hell and Ernst H. K. Stelzer. Properties of a 4Pi confocal fluorescence microscope. *Journal of the Optical Society of America A*, 9(12):2159–2166, December 1992.
- [51] Alexander Egner and Stefan W. Hell. Fluorescence microscopy with super-resolved optical sections. *Trends in Cell Biology*, 15(4):207–215, April 2005.
- [52] Stefan W. Hell, Roman Schmidt, and Alexander Egner. Diffraction-unlimited three-dimensional optical nanoscopy with opposing lenses. *Nat Photon*, 3(7):381–387, July 2009.
- [53] Gleb Shtengel, Michael W. Davidson, Richard D. Fetter, Harald F. Hess, James A. Galbraith, Catherine G. Galbraith, Jennifer Lippincott-Schwartz, Jennifer M. Gillette, Suliana Manley, Rachid Sougrat, Clare M. Waterman, and Pakorn Kanchanawong. Interferometric fluorescent super-resolution microscopy resolves 3D cellular ultrastructure. *Proceedings of the National Academy of Sciences*, 106(9):3125–3130, March 2009.
- [54] Max Born and Emil Wolf. *Principles of Optics*. Cambridge University Press, Cambridge, New York, Melbourne, Madrid, Cape Town, 7th edition, 2002.

- [55] B.E.A. Saleh and M.C. Teich. *Fundamentals of Photonics*. Wiley-Interscience, second edition, 2007.
- [56] Alexander Egner. *Multifokale hochauflösende 3D-Fluoreszenzmikroskopie*. PhD thesis, Heidelberg, 2002.
- [57] Jonas Fölling. *High-Resolution Microscopy with Photoswitchable Organic Markers*. PhD thesis, Göttingen, 2008.
- [58] B. Valeur. *Molecular fluorescence*. Wiley-VCH Verlag, Weinheim, 1st edition, 2002.
- [59] Stefan Bretschneider, Christian Eggeling, and Stefan W Hell. Breaking the diffraction barrier in fluorescence microscopy by optical shelving. *Physical Review Letters*, 98(21):218103, May 2007. PMID: 17677813.
- [60] C. Eggeling, J. Widengren, R. Rigler, and C. A. M. Seidel. Photobleaching of fluorescent dyes under conditions used for single-molecule detection: Evidence of two-step photolysis. *Anal. Chem.*, 70:2651–2659, 1998.
- [61] T. Wilson and C. J. R. Sheppard. *Theory and practice of scanning optical microscopy*. Academic Press, New York, 1984.
- [62] C.E. Shannon. Communication in the presence of noise. *Proceedings of the IRE*, 37(1):10–21, 1949.
- [63] M. Minsky. Microscopy apparatus, 1961.
- [64] A. Egner and S. W. Hell. Equivalence of the Huygens-Fresnel and Debye approach for the calculation of high aperture point-spread-functions in the presence of refractive index mismatch. *J. Microsc.*, 193:244–249, 1999.
- [65] S. W. Hell, M. Schrader, and H. T. M. van der Voort. Far-field fluorescence microscopy with three-dimensional resolution in the 100 nm range. *J. Microsc.*, 185(1):1–5, 1997.
- [66] M. G. L. Gustafsson, D. A. Agard, and J. W. Sedat. Sevenfold improvement of axial resolution in 3d widefield microscopy using two objective lenses. *Proc. SPIE*, 2412:147–156, 1995.
- [67] L. Shao. I5S: wide-field light microscopy with 100-nm-scale resolution in three dimensions. *Biophys. J.*, 94:4971–4983, 2008.
- [68] M C Lang, T Staudt, J Engelhardt, and S W Hell. 4Pi microscopy with negligible sidelobes. *New Journal of Physics*, 10(4):043041, 2008.
- [69] W. Heisenberg. The physical principles of the quantum theory, 1930.
- [70] S. Weiss. Fluorescence spectroscopy of single biomolecules. *Science*, 283:1676–1683, 1999.
- [71] N. Bobroff. Position measurement with a resolution and noise-limited instrument. *Rev. Sci. Instrum.*, 57:1152–1157, 1986.

- [72] E. Betzig. Proposed method for molecular optical imaging. *Optics Letters*, 20(3):237–239, February 1995.
- [73] J. Fölling, V. Belov, D. Riedel, A. Schönle, A. Egner, C. Eggeling, M. Bossi, and S. W. Hell. Fluorescence nanoscopy with optical sectioning by two-photon induced molecular switching using continuous-wave lasers. *ChemPhysChem*, 9:321–326, 2008.
- [74] Russell E Thompson, Daniel R Larson, and Watt W Webb. Precise nanometer localization analysis for individual fluorescent probes. *Biophysical Journal*, 82(5):2775–2783, May 2002. PMID: 11964263 PMCID: 1302065.
- [75] Ted A Laurence and Brett A Chromy. Efficient maximum likelihood estimator fitting of histograms. *Nat Meth*, 7(5):338–339, May 2010.
- [76] Carlas S Smith, Nikolai Joseph, Bernd Rieger, and Keith A Lidke. Fast, single-molecule localization that achieves theoretically minimum uncertainty. *Nat Meth*, 7(5):373–375, May 2010.
- [77] Kim I Mortensen, L Stirling Churchman, James A Spudich, and Henrik Flyvbjerg. Optimized localization analysis for single-molecule tracking and super-resolution microscopy. *Nat Meth*, 7(5):377–381, May 2010.
- [78] Ricardo Henriques, Mickael Lelek, Eugenio F Fornasiero, Flavia Valtorta, Christophe Zimmer, and Musa M Mhlanga. QuickPALM: 3D real-time photoactivation nanoscopy image processing in ImageJ. *Nat Meth*, 7(5):339–340, May 2010.
- [79] Christian Blatter. *Wavelets: a primer*. A K Peters, Ltd., October 2002.
- [80] Claas von von Middendorff. *Experimental Stochastics in High-Resolution Fluorescence Microscopy*. PhD thesis, Heidelberg, 2008.
- [81] M. S. Robbins and B. J. Hadwen. The noise performance of electron multiplying charge-coupled devices. *IEEE Transactions on Electron Devices*, 50(5):1227–1232, 2003.
- [82] David Baddeley, Mark B. Cannell, and Christian Soeller. Visualization of localization microscopy data. *Microscopy and Microanalysis*, 16(01):64–72, 2010.
- [83] Volker Westphal, Silvio O. Rizzoli, Marcel A. Lauterbach, Dirk Kamin, Reinhard Jahn, and Stefan W. Hell. Video-Rate Far-Field optical nanoscopy dissects synaptic vesicle movement. *Science*, 320(5873):246–249, April 2008.
- [84] H. P. Kao and A.S. Verkman. Tracking of single fluorescent particles in three dimensions: Use of cylindrical optics to encode particle position. *Biophys. J.*, 67:1291–1300, 1994.
- [85] F. Aguet, D. Van De Ville, and M. Unser. A maximum-likelihood formalism for sub-resolution axial localization of fluorescent nanoparticles. *Optics Express*, 13:10503–10522, 2005.
- [86] Sri Rama Prasanna Pavani, Michael A. Thompson, Julie S. Biteen, Samuel J. Lord, Na Liu, Robert J. Twieg, Rafael Piestun, and W. E. Moerner. Three-dimensional, single-molecule fluorescence imaging beyond the diffraction limit by using a double-helix point spread function. *Proceedings of the National Academy of Sciences*, 106(9):2995–2999, March 2009.

- [87] Sri Rama Prasanna Pavani and Rafael Piestun. High-efficiency rotating point spread functions. *Optics Express*, 16(5):3484–3489, March 2008.
- [88] Michael A. Thompson, Matthew D. Lew, Majid Badieirostami, and W. E. Moerner. Localizing and tracking single nanoscale emitters in three dimensions with high spatiotemporal resolution using a Double-Helix point spread function. *Nano Letters*, 10(1):211–218, January 2010.
- [89] Majid Badieirostami, Matthew D. Lew, Michael A. Thompson, and W. E. Moerner. Three-dimensional localization precision of the double-helix point spread function versus astigmatism and biplane. *Applied Physics Letters*, 97(16):161103, 2010.
- [90] Johann Engelhardt, Jan Keller, Patrick Hoyer, Matthias Reuss, Thorsten Staudt, and Stefan W. Hell. Molecular orientation affects localization accuracy in superresolution Far-Field fluorescence microscopy. *Nano Letters*, 0(0):0, 2010.
- [91] W M Isenberg, R P McEver, D R Phillips, M A Shuman, and D F Bainton. The platelet fibrinogen receptor: an immunogold-surface replica study of agonist-induced ligand binding and receptor clustering. *The Journal of Cell Biology*, 104(6):1655–1663, June 1987. PMID: 3584243.
- [92] CM 2d Smith, SM Burris, GH Rao, and JG White. Detergent-resistant cytoskeleton of the surface-activated platelet differs from the suspension-activated platelet cytoskeleton. *Blood*, 80(11):2774–2780, December 1992.
- [93] Y. Okamura, K. Kabata, M. Kinoshita, D. Saitoh, and S. Takeoka. Free-Standing biodegradable poly(lactic acid) nanosheet for sealing operations in surgery. *Advanced materials*, 21(43):4388, 2009.
- [94] Stefan Jakobs, Astrid C. Schauss, and Stefan W. Hell. Photoconversion of matrix targeted GFP enables analysis of continuity and intermixing of the mitochondrial lumen. *FEBS Letters*, 554(1-2):194–200, November 2003.
- [95] Alexander Egner, Sophie Verrier, Alexander Goroshkov, Hans-Dieter Söling, and Stefan W. Hell. 4Pi-microscopy of the golgi apparatus in live mammalian cells. *Journal of Structural Biology*, 147(1):70–76, July 2004.
- [96] Jr. Dowski and W. Thomas Cathey. Extended depth of field through wave-front coding. *Applied Optics*, 34(11):1859–1866, April 1995.
- [97] Ilaria Testa, Andreas Schönle, Claas v. Middendorff, Claudia Geisler, Rebecca Medda, Christian A. Wurm, Andre C. Stiel, Stefan Jakobs, Mariano Bossi, Christian Eggeling, Stefan W. Hell, and Alexander Egner. Nanoscale separation of molecular species based on their rotational mobility. *Optics Express*, 16(25):21093–21104, December 2008.

List of publications

Parts of this thesis will be published as follows

1. Aquino, D., Schönle, A., Geisler, C., v. Middendorff, C., Wurm, C. A., Okamura, Y., Lang, T. , Hell, S.W., Egner, A. Multicolor nanoscopy of 3D volumes by 4Pi detection of stochastically switched fluorophores. *Nature Methods* in revision.

Danksagung

An dieser Stelle möchte ich mich bei all denen bedanken, die zum Erfolg dieser Arbeit beigetragen haben.

Mein besonderer Dank gilt Prof. Dr. Dr. h.c. Stefan W. Hell für die großartige Gelegenheit meine Dissertation in seiner Arbeitsgruppe durchzuführen. Die fachlichen Diskussionen und das stetige Interesse an dem Projekt waren immer eine Motivation. Auch das hervorragend ausgestattete Labor und das exzellente Arbeitsumfeld hat entscheidend zum Erfolg dieser Arbeit beigetragen.

Prof. Dr. Rainer H. A. Fink möchte ich für die freundliche Übernahme des Zweitgutachtens danken.

Alexander Egner danke ich für die ausgezeichnete Betreuung, die Unterstützung in jeglicher Hinsicht und dafür, dass er immer für Fragen und Diskussionen zur Verfügung stand. Mit seinen Ideen hat er mich immer motiviert und diese Arbeit erst ermöglicht.

Weiterhin danke ich:

Andreas Schönle, Claas v. Middendorff, Jan Keller und Marcel Leutenegger für zahlreiche Diskussionen, nicht nur fachlicher Natur, und die Unterstützung bei Softwareproblemen jeglicher Art.

Claudia Geisler und Ilaria Testa für die Beantwortung vieler Fragen, vor allem am Anfang des Projekts.

Rainer Pick für die großartige Unterstützung beim technischen Design des Systems.

Christian Wurm, Tanja Gilat und Ellen Rothermel für die Bereitstellung der Proben und freundliche Hilfe in Fragen rund um das Biolabor.

Jaydev Jethwa, Harald Meyer und Marco Roose für technische Unterstützung und hilfreichen Rat.

Jaydev Jethwa, Jan Keller, Andreas Schönle, Steffen Sahl, Claudia Geisler, Ilaria Testa, Chaitanya Ullal, Brian Rankin und Roman Schmidt für das Korrekturlesen von Teilen dieser Arbeit.

Josephine Stadler, Sarah Aschemann und Alena Stephan für die kompetente Unterstützung in organisatorischen Fragen.

Dr. Vladimir Belov und der Chemiegruppe für die Bereitstellung der verwendeten Farbstoffe.

Den Mitarbeitern der Feinmechanik und Optikwerkstatt für die Anfertigung der hochwertigen Bauteile, insbesondere Thomas Meyer, Michael Zigan, Mario Lengauer und Wolfgang Kluge.

Bei meinen Büro- und Laborkollegen, sowie allen Gruppenmitgliedern möchte ich mich für eine tolle Zeit und eine immer freundliche Atmosphäre in den vergangenen Jahren bedanken.

Nicht zuletzt gilt besonderer Dank meinen Eltern, die mir meine Ausbildung ermöglicht haben, sowie meiner ganzen Familie und meiner Freundin Petra Winkler für Unterstützung in allen Belangen.